^{17}O NMR ON CRYSTALLINE HYDRATES: IMPACT OF HYDROGEN BONDING

Sherif Nour

A thesis submitted to the

Faculty of Graduate and Postdoctoral Studies

in partial fulfillment of the requirements for the

Master of Science degree

Department of Chemistry

Faculty of Science

University of Ottawa

ACKNOWLEDGMENTS

I, first and foremost, thank God for blessing me with a great family who supported me through tough times. I ask him to continue blessing me and all those who surround me with success, health, and happiness. To my beloved wife-to-be, I love you and deeply appreciate you. You have always been the real support in my life for the past five years, and I am looking forward to all the years to come living with you.

To the Bryce group, I want to thank you all for a wonderful year of working together; I wish all of you success in your goals. I will never forget the MOOT conference where I got the opportunity to get know you more and truly enjoyed your company. To Dr. David Bryce, I appreciate your great support. I did not only gain scientific knowledge under your supervision, but also built strong work ethics. I wish you the best in the years to come.

I thank Dr. Cory Widdifield and Dr. Kevin Burgess for starting this project and providing assistance when it was needed. I also thank Dr. Gang Wu for providing me with an enriched sample, which was the first hydrate I studied in my work.

TABLE OF CONTENTS

LIST OF TABLES

Table **Page**

LIST OF FIGURES

Figure **Page**

LIST OF ABBREVIATIONS

AT	Acquisition Time
B3LYP	Becke, three parameter, Lee-Yang-Parr
CASTEP	Cambridge Serial Total Energy Package
CP	Cross Polarization
CS	Chemical Shift
CSA	Chemical Shift Anisotropy
DFT	Density Functional Theory
EFG	Electric Field Gradient
FID	Free Induction Decay
GIPAW	Gauge-Including Projector-Augmented Wave
GGA	Generalized Gradient Approximation
HB	Hydrogen Bonding
HF	Hartree Fock
HPPD	High Power Proton Decoupling
IR	Infrared Radiation
MAS	Magic Angle Spinning
MRI	Magnetic Resonance Imaging
MQMAS	Multiple Quantum Magic Angle Spinning
NMR	Nuclear Magnetic Resonance
ppm	Parts per million
PAS	Principal Axis System
PBE	Perdew, Burke, and Ernezerhof
PXRD	Powder X-Ray Diffraction

QI	Quadrupolar Interaction
RF	Radio Frequency
TD	Data Points (time domain)
SSNMR	Solid-State Nuclear Magnetic Resonance
STMAS	Satellite Transition Magic Angle Spinning
SW	Spectral Width

ABSTRACT

The water molecules in inorganic hydrate salts adopt different geometries and are involved in different hydrogen bond interactions. In this work, magic-angle spinning (MAS) and static ^{17}O solid-state NMR experiments are performed to characterize the ^{17}O electric field gradient (EFG) and chemical shift (CS) tensors of the water molecules in a series of inorganic salt hydrates which include: oxalic acid hydrate, barium chlorate hydrate, sodium perchlorate hydrate, lithium sulphate hydrate, and potassium oxalate hydrate, which were all enriched with ^{17}O water. Data were acquired at magnetic field strengths of 9.4, 11.75, and 21.1 T. Gauge-including projector-augmented-wave density functional theory (GIPAW DFT) calculations are performed on barium chlorate hydrate and oxalic acid hydrate where structural changes including the O_w-H•••O distance, H-O-H angle, and O-H distance are employed to understand their impact on the NMR parameters. Furthermore, simplified molecular models consisting of a metal cation and a water molecule were built to establish the effect the M-O_w distance has on the parameters. The computational studies are then used to understand the experimental results. The ^{17}O quadrupolar coupling constant ranged from 6.75 MHz in $K_2C_2O_4$•H_2O to 7.39 MHz in $NaClO_4$•H_2O while the asymmetry parameter ranged from 0.75 in $NaClO_4$•H_2O to 1.0 in $K_2C_2O_4$•H_2O and the isotropic chemical shift ranged from -15.0 ppm in $NaClO_4$•H_2O to 19.6 ppm in $BaClO_3$•H_2O. The computational results revealed the trends for each parameter, where there is an increasing trend for quadrupolar coupling constant and span as a function of increasing hydrogen bond distance, decreasing trend for the three chemical shift tensors as a function of increasing M-O_w distance and unclear trends for asymmetry parameter and skew due to competing electronic factors.

Overall, this study provides benchmark ^{17}O NMR data for water molecules in crystalline hydrates, including the first measurement of ^{17}O chemical shift anisotropy for such materials.

CHAPTER ONE:
INTRODUCTION AND OBJECTIVES

Nuclear magnetic resonance (NMR) is a powerful and versatile technique used in various disciplines in the biological, chemical, and physical sciences. NMR is not just limited to determining structures of compounds using chemical shifts and coupling constants; in fact, applications in NMR have been found useful in fields in which its inventors never expected such as the pharmaceutical, agricultural, oil and gas, and quantitation industries, to name a few. Other aspects of NMR, such as spin relaxation, allow for the study of the binding of guest molecules in receptors, and two-dimensional NMR spectra can provide detailed information on the structures of proteins.[1,2] NMR is also a useful diagnostic device, more commonly known as magnetic resonance imaging (MRI), which can detect abnormalities and disease in a human's body by collecting images. The applications of solution NMR have been well-studied; however, solid-state NMR (SSNMR) is able to exploit the orientation of individual crystallites in powdered samples, which gives additional information in regards to both intermolecular and intramolecular interactions. SSNMR is able to provide this information, whereas solution NMR cannot, because in solution NMR molecules are tumbling rapidly and interactions including magnetic shielding are averaged out, while in solid-state NMR this is not the case.

Bryce et al. have shown that the number of publications in the field of solid-state NMR increased drastically over a ten year period between 1990 and 2000.[3] Research regarding solid-state NMR continues to be on the rise as this technique can be used for studying materials, drugs, and proteins to name a few. In addition to aiding in the determination of molecular structure or molecular orientation, NMR can also be used to

study activation energies, where spin relaxation can be measured as a function of temperature and the activation energy can be calculated. In the oil and gas industry, proton NMR is used to aid in the search for oil and gas wells, where spin relaxation as a function of sample depth can provide necessary information on the composition of the wells.[4] Plant biologists use NMR in determining the structure of nitrogen-containing compounds, using ^{14}N to search of signals associated with deprivation of nutrients in plants.[5] While these are only a few examples, many fields continue to find new and exciting ways in which NMR can provide true benefit.

In this thesis, ^{17}O solid-state NMR is used to characterize the electric field gradient (EFG) and the chemical shift (CS) tensors in a series of inorganic hydrates, which include: oxalic acid hydrate, barium perchlorate hydrate, lithium sulphate hydrate, sodium chlorate hydrate, and potassium oxalate hydrate. One of the main goals of the study is to understand the relationship between the observable ^{17}O NMR parameters and the geometry of the hydrogen bonds involving the water molecules in these hydrates. The complete ^{17}O CS tensor for water itself has never been reported experimentally. Density functional theory gauge-including projector-augmented-wave (GIPAW) calculations are used to determine the impact of the structural changes, such as the hydrogen bond distance, O-H distance and water angle (H-O-H) on the NMR parameters, and order them from highest to lowest impact. The objective of the calculations is to complement the experimental results in determining impact of various geometrical parameters of the hydrogen bond on the observed NMR parameters. This study allows us to understand the most significant structural contributions to the different parameters obtained from the experiments.

First, this thesis provides a brief introduction to NMR in light of its theory and mechanisms in Chapter 2; this will include a greater focus on solid-state NMR, challenges to overcome with NMR, different interactions in NMR, and the necessary equipment. The introduction also discusses some of the relevant powder X-ray diffraction (PXRD) and computational chemistry theory. I note briefly here that PXRD was used in order to confirm the structure and the purity of the ^{17}O enriched samples (details regarding the preparation of these samples are included in Chapter 4). Next, Chapter 3 will cover the theory behind hydrogen bonding, the structure of both water and ice, literature ^{1}H NMR studies on ice at different temperatures, and literature ^{1}H NMR studies on crystalline hydrates in determining the chemical shift changes due to different structural features. This section also covers previous studies done on ice and water using ^{17}O NMR, and further studies done using that same technique on organic polymers and materials in order to put into perspective the different ranges for the NMR parameters such as quadrupolar coupling constant and asymmetry parameter, which will be discussed in the chapters to come.

Subsequently, Chapter 4 provides all the experimental results for all samples and all the parameters obtained from spectral analysis, some of which showed more than one crystallographically unique oxygen site. It also includes all the computational results which illustrate the factors contributing to the impact the geometry of hydrates has on the NMR parameters. This section describes in detail how the NMR parameters are characteristic of the hydrogen bond. Finally, Chapter 5 provides a summary including insight as to how the parameters obtained reflect what the computational studies have shown, and provides a final comparison of the Cambridge serial total energy package (CASTEP) calculations to the experimental results.[6]

Overall, the purpose of this thesis is to give the reader new insight into the topic of hydrogen bonding, which although has been around for a long time, has never been thoroughly studied from this angle, which is ^{17}O NMR. The study is based on obtaining experimental results which includes ^{17}O NMR parameters for five different hydrates while considering the impact of structure changes on the parameters using computational methods to determine which factors most contribute to the experimental results.

CHAPTER TWO:
INTRODUCTION TO NMR AND METHODS

In this chapter, some basic theory relating to solid-state NMR (SSNMR) and solution NMR will be presented. Solution NMR has been used for many different applications including protein chemistry, kinetics, oil and gas, and organic chemistry to name a few.[1,2,4,5,7] The chemical shifts obtained by NMR can provide much information and can be used directly to determine not just the structures of molecules, but also how these molecules interact with one another. The application of SSNMR is even more profound as it provides further information arising from the distribution of orientations of crystallites in powders. After discussing some basic theory, this chapter will also give detail regarding the spectrometer itself, and how it allows one to obtain NMR signals. Thirdly, the four important interactions in NMR will be discussed, which are: magnetic shielding, dipolar coupling, indirect spin-spin coupling, and quadrupolar coupling. Quadrupolar nuclei have a spin larger than one half and possess a nuclear charge distribution that is not symmetric. Quadrupolar nuclei will be discussed in some detail since this work is based on ^{17}O, which has a nuclear spin of 5/2. Also, the SSNMR on different types of solids such as powders and crystals will be discussed in further detail. This also leads to the need to understand the different techniques used to overcome issues in SSNMR such as line broadening, which includes cross polarization, magic-angle spinning, and proton decoupling. The quadrupolar interactions in SSNMR give rise to first- and second-order interactions which will also be discussed. The equipment used for SSNMR is somewhat different than for solution NMR and will need to be studied in order to understand the difference. Powder X-ray diffraction is an important method in studying structures of solids and will also be discussed in this chapter.

Computational methods aiding researchers in predicting values such as NMR parameters will also be studied.

2.1 Theory of NMR

In this section, the properties of spin will be discussed along with the Zeeman splitting which gives rise to NMR. This Zeeman splitting allows one to determine the Larmor frequency at which the spins precess when an applied magnetic field is present. It is also necessary to discuss the 90° pulse and the free induction decay (FID) which gives rise to the signal observed through complex mathematical formulas.

2.1.1 Spin

Many nuclides have a property called spin angular momentum, which can be expressed with the equation shown below (**Equation 2.1**). The spin of a nucleus itself is a type of angular momentum. This angular momentum can be expressed both in classical and quantum mechanics where in the former, the angular momentum can be described as being associated with a rotating object.

$$p = h\sqrt{I(I+1)} \qquad \textbf{Equation 2.1}$$

The terms p and h are the angular momentum and the Planck's constant, respectively. The spin quantum number, I, is a fundamental property for each nuclide and takes a value of $0, \frac{1}{2}, 1, \frac{3}{2}, 2, \frac{5}{2}, 3, \frac{7}{2,}$ etc where if $I > \frac{1}{2}$, the nucleus is said to be quadrupolar, which is discussed later in this chapter. There are $(2I+1)$ allowed values of a second quantum number, m. The charged nuclei possess a magnetic moment which is directly proportional to its angular momentum and can be represented by **Equation 2.2.**

$$\mu = \gamma\hbar\sqrt{I(I+1)} \qquad \textbf{Equation 2.2}$$

Here, γ is the gyromagnetic ratio. The quantized energy is therefore the product of the magnetic moment and the applied magnetic field as shown in **Equation 2.3**.

$$E = -\mu B_0 \qquad \textbf{Equation 2.3}$$

2.1.2 Larmor frequency

As mentioned, each nuclear spin has a nuclear magnetic moment which generates a magnetic field and when there is an applied magnetic field, there will be an interaction of the two. At equilibrium, spins will have random directions and the sum of all of these spins' magnetic moments is referred to as bulk magnetization. Once an applied magnetic field is present, the bulk magnetization will tend to be aligned with that magnetic field, which in a rotating frame, is referred to as the z-axis. In a magnetic field, the spin magnetization will precess around the z-axis at a rate known as the Larmor frequency. This is the inverse of the time it takes for a spin to precess around the z-axis one full round. As shown in **Equation 2.4**, the Larmor frequency (ν) is directly proportional to the gyromagnetic ratio (γ) and the applied magnetic field (B_0).

$$\nu = \frac{-\gamma}{2\pi}B_0 \qquad \textbf{Equation 2.4}$$

2.1.3 Zeeman splitting

As shown in **Figure 2.1**: Zeeman Splitting, there is a splitting in energy which arises due to spins aligning themselves according to their energy states where they are either α (lower energy) or β (higher energy). The difference in energy is quantized and is proportional to the Larmor frequency mentioned above. The spins basically split into these two populations in the presence of an applied magnetic field. The number of splittings

observed will be based on *I* where if *I* is $\frac{3}{2}$, for example, then there will be three splittings due to the transitions $-\frac{3}{2}\rightarrow-\frac{1}{2}$, $-\frac{1}{2}\rightarrow\frac{1}{2}$, and $\frac{1}{2}\rightarrow\frac{3}{2}$.

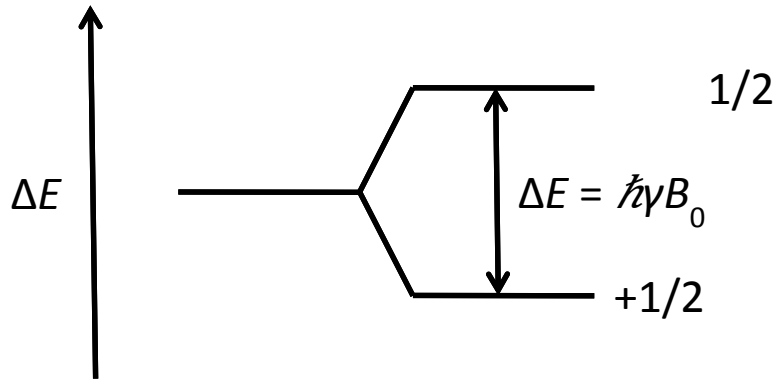

Figure 2.1: Zeeman Splitting

2.1.4 90° radiofrequency pulse

In an NMR experiment, the spin magnetization is measured perpendicular to the magnetic field, not along it. In the applied magnetic field, a 90° radiofrequency pulse may be applied along the x-axis to the initial net magnetization. The spins will then undergo precession around the axis and relax back to the z-axis (along the external magnetic field). During a single 90° pulse experiment, the radio frequency (RF) is chosen with a frequency close to the Larmor frequency for the nuclear isotope of interest. The pulse will then be switched off and the precession of the nuclear spins will lead to a FID. The same is true for multiple-pulse experiments such as spin echoes, where a time interval denoted τ (which is the time between two RF pulses) is inserted between two pulses, where the second pulse is twice as long as the first. [8]

2.1.5 Free induction decay

After the 90° pulse, the spins will begin to lose the phase coherence in the x-y plane, where the time constant for this process is referred to as T_2, the transverse relaxation. The spectrometer will acquire the FID which is the signal recorded in the x-y plane after the 90° pulse as a function of time. Another important time constant is the longitudinal relaxation time which is the time it takes for the spin to return to the z-axis to re-establish equilibrium. The FID consists of two mathematical equations; M_x and M_y which are the magnetizations along both axis as shown in **Equation 2.5** and **Equation 2.6**.

$$M_x = M_0 \sin\beta \cos \Omega t \qquad \textbf{Equation 2.5}$$

$$M_y = M_0 \sin\beta \sin \Omega t \qquad \textbf{Equation 2.6}$$

M_0 is the amplitude of magnetization at $t = 0$ where t is time, β is the pulse rotation angle, and Ω is the offset frequency. Two relaxation processes occur during this re-establishment of the equilibrium magnetization. The first is called transverse relaxation, which is characterized by an exponential decay, with time constant T_2. The second is T_1 which is known as the spin-lattice relaxation time constant and redistributes the population of spin states (α and β) to reach thermal equilibrium.

2.2 Interactions in NMR

There are four major interactions contributing to NMR spectra, which are: magnetic shielding, direct dipole-dipole coupling, indirect coupling (*J*-coupling), and quadrupolar coupling. These are discussed in turn below.

2.2.1 Magnetic shielding

According to Ramsey, the magnetic shielding is due to the sum of two opposing currents, which are called the diamagnetic and the paramagnetic shielding where the magnetic field arising from the diamagnetic current goes in the opposite direction of the applied magnetic field while the paramagnetic current goes in the same direction as the applied magnetic field, as shown in **Equation 2.6**.[3]

$$\sigma = \sigma_p + \sigma_d \qquad \textbf{Equation 2.6}$$

Magnetic shielding may be described by a second-rank tensor containing up to nine independent tensor components as shown in **Equation 2.7**.

$$\sigma = \begin{bmatrix} \sigma_{xx} & \sigma_{xy} & \sigma_{xz} \\ \sigma_{yx} & \sigma_{yy} & \sigma_{yz} \\ \sigma_{zx} & \sigma_{zy} & \sigma_{zz} \end{bmatrix} \qquad \textbf{Equation 2.7}$$

In its principal axis system, there are three principal components (σ_{11}, σ_{22}, and σ_{33}) and principal axes. These are the directions of the external magnetic fields where the induced field is parallel to that external field. It is the magnetic shielding (σ) that determines the chemical shift (δ) of an NMR signal as shown in **Equation 2.8**.

$$\delta = 10^6 \frac{\sigma_{ref} - \sigma}{1 - \sigma_{ref}} \qquad \textbf{Equation 2.8}$$

The chemical shift is said to be isotropic when the three principal components of the chemical shift tensor (δ_{11}, δ_{22}, δ_{33}) are the same. When two or more are not the same, the chemical shift is said to be anisotropic. To first order, the chemical shift depends on the value of σ_{ZZ}. The isotropic chemical shift tensor shown in **Equation 2.9** is the average of all three chemical shift tensors. Shown in **Equation 2.10** is the span, which is the breadth of a

spectrum. Also the skew is shown in **Equation 2.11** which measures the asymmetry of the tensor and may be either positive or negative, as shown in **Figure 2.2**.

$$\delta_{iso} = \frac{1}{3}(\delta_{11} + \delta_{22} + \delta_{33}) \qquad \textbf{Equation 2.9}$$

$$\Omega = \delta_{11} - \delta_{33} \qquad \textbf{Equation 2.10}$$

$$\kappa = 3(\delta_{22} - \delta_{iso})/\Omega \qquad \textbf{Equation 2.11}$$

The shielding Hamiltonian is shown in **Equation 2.12** where B_0 is applied magnetic field, $\boldsymbol{\sigma_{ZZ}}$ is the z shielding component, and I_z is the spin vector for z-component .

$$H = B_0\, \boldsymbol{\sigma_{ZZ}}\, I_z \qquad \textbf{Equation 2.12}$$

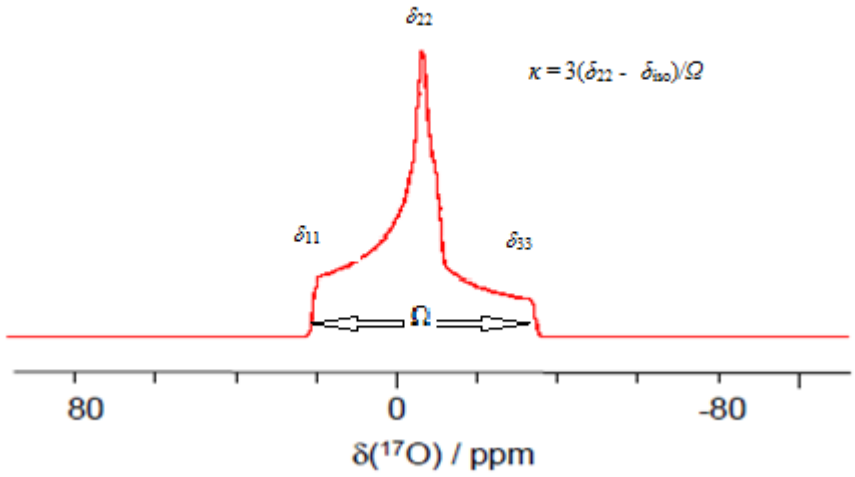

Figure 2.2: Span and skew

2.2.2 Direct dipole-dipole coupling

In direct dipole-dipole coupling, each spin influences the neighbouring spin due to their magnetic moments. This interaction is actually through space not through a bond. A dipolar coupling constant denoted R can be calculated directly from the spectrum in the case of an isolated spin pair. For sharper signals, ^{1}H decoupling is necessary to be able to observe

the spectra of nuclei of interest. The definition for R is shown below (see **Equation 2.13**) where r is the distance between two spins and γ_1 and γ_2 are the gyromagnetic ratios of both spins. The dipolar tensor is not just symmetric but axially symmetric and the isotropic value is zero since the trace is zero. Another factor also plays a role in dipolar coupling is the combinations of two spins coupling which includes α and α or β and β, or β and α, or α and β. Different energies will be obtained based on the direction of the spins coupling.

$$R = \frac{\gamma_1 \gamma_2}{r^3} \frac{h}{2\pi} \frac{\mu_0}{4\pi} \qquad \textbf{Equation 2.13}$$

2.2.3 Indirect spin-spin coupling

Spin-spin coupling also known as *J*-coupling, often arises between covalently bound nuclear spins. The *J*-coupling itself can be divided to five contributions including diamagnetic spin-orbital, paramagnetic spin-orbital, Fermi contact, spin-dipolar, and cross coupling where the largest contribution often arises from the Fermi contact coupling, which is due to the interaction between an electron at the nuclei and the nuclei. The Hamiltonian for spin-spin coupling and its tensor are shown in **Equation 2.14** and **Equation 2.15**. Here, h is Planck's constant, $\boldsymbol{J}$ is the spin-spin coupling tensor and I is the spin operator.

$$H = h\, I_1 \boldsymbol{J}\, I_2 \qquad \textbf{Equation 2.14}$$

$$\boldsymbol{J} = \begin{bmatrix} J_{xx} & J_{xy} & J_{xz} \\ J_{yx} & J_{yy} & J_{yz} \\ J_{zx} & J_{zy} & J_{zz} \end{bmatrix} \qquad \textbf{Equation 2.15}$$

2.2.4 Quadrupolar coupling

Lastly, the quadrupolar coupling interaction is present when the nuclei studied have spin quantum number $I > ½$. The nuclear electric quadrupole moment couples with the electric field gradient (EFG) generated by the surrounding charges in the molecule and

crystal. For quadrupolar spins, the charge distribution within the nuclei is anisotropic. The sum of the principal components of the electric field gradient tensor is equal to zero as shown in **Equation 2.16,** where the associated principal axes are usually closely dictated by the local molecular symmetry.

$$V_{xx} + V_{yy} + V_{zz} = 0 \qquad \textbf{Equation 2.16}$$

The first-order quadrupolar coupling averages to zero in isotropic liquids but does not in anisotropic liquids. In solids, interestingly, first- and second-order effects are usually observed in spectra. The quadrupolar nuclei itself is asymmetric which gives rise to these interactions. These first- and second- order interactions results from the quadrupolar moment, is equal for all oxygen, and the electric field gradient (EFG) which results from the orientation of the molecule. Essentially, a quadrupolar nuclei will have more splitting than just the central transitions, which are referred to the satellite transitions. This energy splitting will be different when these quadrupolar interactions are present. The quadrupolar coupling constant (C_Q) and the asymmetry parameter (η) can be calculated as shown in **Equation 2.17** and **Equation 2.18**.[8]

$$C_Q = \frac{eV_{zz}Q}{h} \qquad \textbf{Equation 2.17}$$

$$\eta = \frac{V_{XX} - V_{YY}}{V_{ZZ}} \qquad \textbf{Equation 2.18}$$

2.3 Quadrupolar nuclei

As mentioned above, quadrupolar nuclides do not have a perfect sphere of charge distribution, but instead have an uneven charge distribution.[3] Therefore; they have strong interactions between their quadrupolar moments and the local EFG. However, that

interaction may or may not be easily observed depending on the nature of the sample, e.g., whether it is in the liquid or solid state. For example, for nuclei with spin $I = \frac{5}{2}$, in isotropic liquids, the quadrupolar coupling will not affect the spectrum but instead a single peak will be observed, whereas in liquid crystals a quadrupolar doublet splitting will be observed in anisotropic liquids. In solid powders, the molecules all have random orientations and the quadrupolar splitting will be based on the orientation of the EFG tensor with respect to the applied magnetic field. What is observed is just the sum of all these orientations with frequencies close to each other. The weak intensity in the outer most shoulders is due to the fact that there is a higher chance for the electric field gradient axis to be perpendicular to the field rather than parallel to it. Based on the width of the spectra, one can determine the quadrupolar coupling constant which is measured in megahertz. Sometimes the spectra are too broad when one applies just a regular pulse and therefore a quadrupolar echo can be used. A broad spectrum is due to a very rapid decay of the FID which is hard to detect and therefore one can avoid this problem by using echo experiments which puts the NMR signal at time separated from the end of the pulse. This echo can then be repeated multiple of times to build up a signal with lower noise.[8]

In solids, quadrupolar interactions are studied extensively due to their importance in describing the charge distribution around the nucleus of interest since it provides valuable information on the geometrical bonding arrangement. Quadrupolar interactions lead to first- and second-order quadrupolar effects which can be observed in the spectra. The second-order quadrupolar interactions can also be observed when the quadrupolar coupling constants are large with respect to the Zeeman term. It is worth noting that both the first and second quadrupolar shifts are dependent on the EFG with respect to the orientation. In terms of the

energy levels for a quadrupolar spin, the energy difference across the central transition remains the same even after the contribution of both first- and second-order interactions as

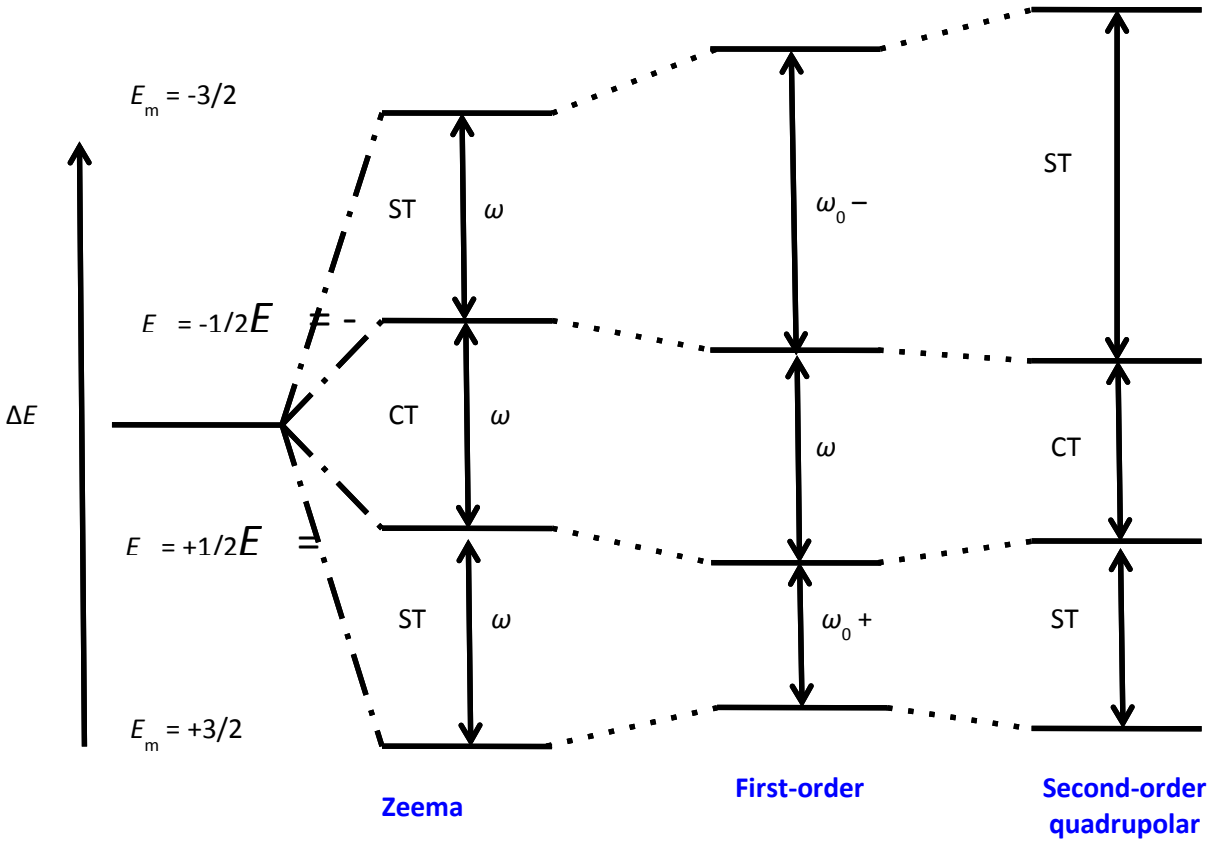

shown in **Figure 2.3** which shows the energy level diagram for a spin 3/2 nucleus, with the energy differences resulting from the first- and second-order quadrupolar interactions. It is worth noting that the second-order effects are inversely proportional to the applied magnetic field and their magnitudes decrease with spin state *I*. The first-order shift is proportional to $3\cos^2\Theta$-1 while the second-order is not.[9] As shown in F**igure 2.3**, the ω_0 is the angular frequency due to the splitting and the ω_Q is an angular frequency due to the first order quadrupolar shift

2.4 Solid-state NMR

2.4.1 The importance of solid-state SNMR

As mentioned, SSNMR plays a vital role in exploiting structural features that solution NMR cannot due to rapid tumbling of the molecules in solution. Thus, the parameters obtained from SSNMR can reflect the composition of the unit cell, in comparison to the solution NMR which only reflects the behaviour of an isolated (solvated) molecule. For single crystals, for instance, nuclei with the same position in a molecule will give rise to different frequencies due to their different orientations. In addition to that, molecules that are found in asymmetric units will have different packing (intermolecular) and geometry (intramolecular) arrangements and therefore two same molecules in a different layer of the single crystal will give rise to two different frequencies.

If the solid sample studied is not a single crystal, then it can take other forms which may contain disorder in its structure. First, it may be static or dynamic where atoms in the molecule can be at different positions or undergo exchange between two different locations. Another type of solid is amorphous when the atoms inside its molecules are in the range of the local fields which give rise to broad spectra. A large number of amorphous solids actually possess a property known as preferred orientation where polymers are directed in a specific orientation. A final type of crystalline material lie between the isotropic solution and the crystalline solid is called liquid crystalline states. It is clear by now that solid-state NMR is more complex than solution NMR due to the interactions mentioned earlier and therefore techniques such as high power proton decoupling (HPPD), magic angle spinning (MAS), and cross polarization are used, just to name a few. HPDD offers a solution to the large line broadening since when one is observing spectra for a nuclide coupled to a large

number of protons, distinction of sites is not possible. Therefore this technique will eliminate the dipolar coupling to observe more resolved spectra. Magic angle spinning also solves the large line broadening but for a different reason. The CSA causing broad lines can be resolved by rapid sample spinning at angle of 54.7° will average its interactions to produce sharp lines spectra. The intensity of the signals observed for a solid sample can also be an issue which usually leads to small signal-to-noise ratio. CP offers a solution to the low intensity where magnetizations transfer is allowed between protons and the nuclei of interest.[9]

2.4.2 Techniques in solid-state NMR

NMR experiments on solids are not just complex because of line broadening or signal intensity, but the setup itself is more sophisticated when compared to solution NMR.[3] First, one FID will not yield a spectrum with an observed signal and therefore the experiment is repeated a number of times and the FID of all runs are added to obtain a signal. However, one cannot just wait till the FID is finished and then repeat right away because time needs to elapse between each FID, known as the recycle delay. This recycle delay is dependent on T_1. Secondly, the length of the FID cannot be too long (which will lead to more noise), neither it can be too short (which will lead to truncation of the FID). This time is known as the acquisition time and is one of the important parameters one must consider when running a SSNMR experiment. Another important parameter is the spectral width, which is dependent on data points in the FID as shown in **Equation 2.19** where AT is the acquisition time, SW is the spectral width and TD is data points. It is not an issue if the spectral width is large, but if it is too small signals can end up falling outside the width range. The dead time is the time it

takes for a pulse to fully decay. There is no point in collecting data during the dead time, but it is essential in avoiding any distortion in the beginning of the FID. Finally, the receiver gain can also be adjusted for each experiment so that no signal baseline artefact is observed.[9]

$$AT = \frac{TD}{2SW} \qquad \textbf{Equation 2.19}$$

2.4.3 Equipment used in solid-state NMR

Since SSNMR is more sophisticated than solution NMR, different equipment is required.[3] First, high power amplifiers are required, which goes back to the fact that intense RF pulses are necessary in order to excite the entire spectral width. Faster sampling rates are required in SSNMR in comparison to solution NMR, which requires a high speed digitizer. High power probes are also required again because of the high RF and to be able to spin samples rapidly for MAS experiments. The rotor that holds the samples are usually made out of zirconia or silicon nitride. It is worth noting that the most common probe used is the double resonance probe which has the ability to perform cross polarization and MAS experiments.[3]

2.5 Introduction to powder X-ray diffraction

X-rays have provided an important technique to study structures of both liquids and solids.[10] NMR techniques are complementary to X-rays in most studies, where X-rays may serve as a secondary tool to confirm structural observations made using NMR spectra, or vice versa. X-rays are a high energy electromagnetic radiation with range between 200 eV and 1 MeV lying between ultraviolet and gamma rays. The production of X-rays is through a tube which consists of two metal electrodes inside a chamber. The tungsten filament cathode will produce electrons, which will accelerate towards the anode. The electrons at

that point will have a high velocity and it will collide with the anode. These electrons will convert to X-ray beams due to the impact of collision. The atoms that are in the sample studied have a specific arrangement in a periodic array to them, which can diffract the light. Shown in **Equation 2.20**, the Bragg law's formula where d_{hkl} is the distance between the parallel planes of atoms, and the wavelength fixed.

$$\eta\lambda = 2d_{hkl}\sin\Theta \qquad \textbf{Equation 2.20}$$

The position and the intensity of the peaks observed are unique to the structure of the sample studied. The position and the intensity of the peaks are representatives of the distance between the planes of the atoms arranged, d_{hkl}, and the arrangement of the atoms respectively. The arrangement of the atoms can be studied by a structure factor which is the sum of all the scattering from all of the atoms. It is also worth noting that the peak position is dependent on the wavelength which can be different for different elements. Also, the diffraction for different samples will be at different angles which are denoted by 2Θ, which is the angle between the incident beam and the detector. In powders, the sample will contain thousands of random orientations and therefore, the peaks can overlap when the quantity of the sample is small but usually this is not a problem when the volume is large since larger contribution will give rise to the diffraction. Single crystals on the other hand, have a longer range order which indicated that for each set of planes there is equal number of crystallites which will diffract.[11]

X-rays studies done on liquid water were done by plotting the intensity of the peaks as a function of the angle between the scattered radiation and the incident beam. The study done by Bernal and Fowler indicated that the distance between molecules and the neighbours is not random, that over a large concentration molecules exist at about 2.9, 4.5-5.3, 6.4-7.8

Å, and lastly that each molecules have four closest neighbours. All these results were confirmed later by NMR both in solid and solution states.[12]

2.6 Computational methods

Computational methods have become an important part of chemical research in different fields since they provide powerful techniques for obtaining calculated results useful enough to provide useful insights into the compounds studied. Valuable computational methods include Hartree-Fock (HF), density functional theory (DFT), configuration interaction (CI) and Moller Plesset perturbation theory (MP) to name a few. Most of these computational methods are based on wave functions and an operator acting on them except for DFT which uses charge density instead of wave functions. These computations can be used to determine calculated values for EFG and CSA tensors.

2.6.1 Theory of computational chemistry

All properties of a stable state can be obtained by solving the Schrödinger equation as represented by **Equation 2.21** shown below. H is an operator that sums the kinetic and potential energy components and E is the energy value also known as an eigenvalue, and most importantly ψ is the wave function.

$$H\,\psi = E\,\psi \qquad \textbf{Equation 2.21}$$

The operator H, as mentioned, accounts for the kinetic energy of the electrons, nuclei, electrostatic interaction between electrons and nuclei (attractive) and between the electrons (repulsive). The wave function ψ describes the behaviour of all electrons or the molecular orbitals and can take any form as long as it is an eigenfunction of the Hamiltonian operator and it is antisymmetric. In principle, a Slater determinant which is a determinant of a matrix

containing rows of molecular orbital of spins is the simplest form of a wave function. Two conditions must be satisfied, however, which are that the Slater determinants must be antisymmetric and that no spin orbital must be associated with specific electron spin. Another important aspect of wave functions is exchange where all spins of α can exchange among with themselves and all spins β can also exchange among them. Second, the correlation factor must be taken into consideration where correlation refers to electrons allowed to adjust to one other's position. It is worth noting that it is impossible to determine the exact or true wave function but one can find as close as possible to the true form of ψ using these various methods that will yield a lowest *E*. The HF method is an *ab initio* (no use of experimental results) method and has a single determinant wave function where the spin orbitals in that determinant can be optimized to obtain the lowest *E*. However, HF does not account for correlation where in reality, as mentioned, electrons adjust to one another. The HF equation then accounts for the energy of electron, attraction of nuclei and electron, repulsion between the electron and nuclei and the exchange factor. Slater determinants formed by two-electron integrals are not easy to calculate and therefore another way to calculate the wave functions is using Gaussian in form of basis sets. These basis sets can be as large as to include all possible orbitals, including virtual ones, or as small as including only core orbitals. Large basis sets, accounting for more molecular orbitals which usually bring the calculated result closer to the experimental result. Gaussian functions are proportional to $e^{-\alpha(r-R)^2}$ where *R* is the position of the nucleus where the orbital is centered, α is the Slater orbital exponent, and *r* is position of the electron.

It must be noted that Gaussian functions do not represent the exact shape of Slater determinant and to improve that usually α is adjusted to reproduce the salter's exact shape.

CI solves the issue of using a single Slater determinant which is used by HF which is the cause of the missing correlation factor by forming a linear combination of the single Slater determinants. Therefore, a CI matrix is simply a large matrix with single Slater components replaced by virtual orbitals which are called excited determinants. For instance, a doubly excited determinant is one where two spin orbitals of the HF determinant are replaced by two virtual orbitals. This matrix becomes problematic itself because of its large and size and therefore some virtual orbitals which are highest in energy can be excluded. The disadvantage of using CI is size consistency, where calculations involving CI can yield different results since degrees of freedom can be different for each. MP is based on the perturbation theory which uses a Taylor expansion to determine the closest value to the *H* (the true Hamiltonian) and uses HF as a starting point. In MP, the true Hamiltonian is used in order to determine the true energy using first, second, third orders of corrections to the energy term (MP1, MP2, etc.). Another important method CC will be used a sum of T operators which will act on the HF determinant to generate singly excited determinants which can then be size consistent. These methods are only discussed here to show the different methods used by chemists, however only DFT and Gaussian are used in this study. First, CASTEP which uses DFT is used for two reasons; one theoretical and the other practical. The theoretical reason is that DFT is based on the electronic density around the nucleus and therefore it accommodates for the intramolecular interactions. Also, studying NMR literature, one can see that CASTEP is widely used by NMR chemists because it gives good correlation with experimental results. The Perdew, Burke, and Ernzerhof (PBE) based method belongs to generalized gradient approximation for the exchange and correlation functional.[13] The uniqueness of this exchange correlation energy is that it is dependent on the density at given local point. Gaussian is also used to measure how hydrogen bond

geometries affect parameters for molecule in vaccum..Specifically speaking B3LYP is a hybrid functional, implying that it has an exact exchange portion in it. Exact exchange basically comes from HF which means that alpha and beta spins can exchange with one another. These hybrids functional give good correlation with experimental results, and that is the major reason for using it in this study. CASTEP calculation however is known to be computationally expensive and therefore one cannot rely on them for all of the computational calculations obtained in this study. Next sections will discuss density functional theory thoroughly.

2.6.2 Density Functional Theory

The previous methods have simply generated sums of single determinants in different ways in order to obtain the best of approximation of *E*. DFT instead uses the charge density approach to explaining the electronic structure of a molecule. It is rather simpler to use a density function than a complicated wave function, yet to get the density one must calculate the wave function first. Hohenberg-Kohn stated that the energy of a specific system can be expressed in terms of the density as shown in the equation below.[14]

$$E = E\,[p(r)] \qquad \textbf{Equation 2.21}$$

This energy function can be expressed as the sum of the kinetic energy, electron-electron repulsion and the exchange correlation factors as shown in **Equation 2.22**.

$$E\,[p(r)] = T\,[p(r)] + U\,[p(r)] + E_{XC}\,[p(r)] \qquad \textbf{Equation 2.22}$$

The electron-electron repulsion factor itself is the sum of the Coulombic attraction of nuclei and electrons and Coulombic repulsion of electron density and itself. The exchange and correlation (XC) component can be approximated by an integral of the product of electron density and exchange and correlation energy density. Accurate results for the XC can be

determined by local density approximation (LDA) which treats each point in space to have a XC energy density similar to jellium model which have charges spread out in space homogenously.[14]

2.6.3 Gauge including projector augmented wave (GIPAW) calculations

GIPAW method is DFT based and is used to calculate the magnetic resonance properties. While other methods allows us to calculate NMR properties on isolated molecules, the advantage of GIPAW is that it takes into consideration the intermolecular interactions in solid yielding much closer values to the experimental values. Put simply, GIPAW describes the behaviour of electrons in a solid periodic crystal. This is done first through calculating the quantum mechanical response the electrons will have to magnetic field and secondly through the pseudopotential to indicate the relation between the core and valence electrons state.[15] The advantage of using pseudopotentials is that they allow one to eliminate the core electrons from the calculation since they have a smaller contribution to shielding in comparison to the valence ones, and to smooth the valence wave functions which are close to the nucleus.[15] The original projector augmented wave method relies on the field-dependent operator T_B which determines the valence pseudo wave functions on all electron wave functions and imposes translational invariance. This operator will then act on the pseudo eigenstates which are generated from all of the electron's eigenstates to give another wavefunction that can describe the behaviour of all electrons in the crystal.[16]

Shown in **Equation 2.23** is how the magnetic shielding is calculated using GIPAW where the induced magnetic field is calculated using perturbation theory and then the wave functions and the density around the nucleus is reconstructed. As shown in **Equation 2.24,**

the Hamiltonian used to calculate the chemical shielding which is dependent on atomic coordinates.[17]

$$B_{ind}(r) = \frac{1}{c}\int j(r_{\cdot}) \times \frac{r-r'}{r-r'^{3}} dr' = -\sigma B_{ext} \qquad \textbf{Equation 2.23}$$

$$H = \frac{1}{2}\left[p + \frac{1}{c}A(r)\right]^{2} + V(r\text{-}t) \qquad \textbf{Equation 2.24}$$

CHAPTER THREE:
HYDROGEN BONDING AND ^{17}O NMR LITERATURE REVIEW

Hydrogen bonding remains a relevant topic since it is essential in a variety of chemical and biological systems. In this chapter, the definition of a hydrogen bond will be discussed along with the structure of liquid and solid water. Infrared (IR) spectroscopy will also be discussed, including its usage in detecting hydrogen bonding. ^{1}H NMR is important and can provide insight in the behaviour and the structure of water that other techniques cannot. ^{1}H SSNMR can provide even further valuable information, since the dynamics of water are not averaged out due to molecular tumbling like in solution, where the parameters can directly related to the H-bonding geometry. Finally, in order to put the NMR parameter ranges in perspective, this chapter also includes an extensive literature review on ^{17}O SSNMR on ice and other solid systems including acid derivatives, magnesium silicates, and nucleic acid components, to name a few.

3.1 What is a hydrogen bond and why are they important?

In 1920, W. M. Latimer and W. H. Rodebush described that water has a tendency to gain and lose hydrogen while a free pair of electrons on the oxygen attracts hydrogen on another water molecule, which forms two molecules bound together.[18] Indeed, even now this description remains qualitatively true. A hydrogen bond can be defined as a bond that is present between a functional group A-H and an atom B, as shown in **Figure 3.1**, which can be present in the same or different molecules.[12] This definition must also satisfy two requirements: evidence of bond formation and evidence that it is the H linked to A (hydrogen donor) that is the one bonding to B (hydrogen acceptor). The formation of a hydrogen bond

will alter the arrangement of atoms and the electronic structure of a molecule. These physical property changes can be directly observed using different spectroscopic methods such as NMR, IR, Raman spectroscopy, and ultraviolet and visible spectroscopy.[12]

Hydrogen bonding can occur with main group elements in fragments such as C-H, S-H, P-H, Si-H, As-H, and Se-H just to name few.[12] Also, only weak hydrogen bonds can form with halogens, which has been a surprising finding since halogens are highly electronegative and should form strong hydrogen bonds. Dunitz and Taylor studied over five thousand molecules containing C-F bonds, which act as B fragment, with the potential of forming hydrogen bonds. Only thirty seven of these molecules participated in hydrogen bonding.[19] Selenium, silicon, phosphorus, tin, and arsenic can act as B fragments where the strength of the hydrogen bond forming is directly related to their electronegativity. Hydrogen bonding can also form with metals where it can either be directly bond with metal center or ligands. The importance of hydrogen bonding is widely observed in biological systems, crystal packing, materials, enzymatic catalysis, and water chemistry to name a few.[12]

3.2 The structure of ice and liquid water

The geometry of O-H•••O is important since the length and the strength of the bond is what provides evidence of hydrogen bonding. In hydrates, the water molecule, with its combination of acidic and basic activity, is what provides stability to the crystals where the hydrate molecules bond together.[12] In both organic and inorganic hydrates, the hydrogen bond (O_w-H•••O) length ranges between 2.65 and 2.90 Å (as shown in **Figure 3.1**). Since water can be acidic and basic, the H-O-H angles will indicate the locale of non-bonding

electrons of the water. In most cases, the decreasing strength of acidity of water molecules can be linked to longer H-bonds in organic acids, carboxylic acids, phenols, and alcohols.[20]

The most basic form of ice is ice I with a hexagonal geometry.[20] Each oxygen is centered in a tetrahedron with four surrounding oxygens at a distance of 4.5 Å and a hydrogen bond distance of 2.75 Å (as shown in **Figure 3.1**). The oxygen lone pair is directed towards two of its O-H neighbours forming two O-H•••O hydrogen bonds.[20] The hexagonal rings of the water molecules have a chair conformation forming layers perpendicular to the *c* crystal axis. The length of the H-bond in ice decreases from 2.76 Å to 2.74 Å when the temperature is decreased from 0 to -180 °C. Locating the hydrogen atom positions in ice is more difficult than the oxygen, however, since X-rays are not as effective for finding hydrogen.[20] Generally, there is more than one possible arrangement for the hydrogen atoms. Peterson and Levy studied solid D_2O and claimed that the O-D bond is 1.01 Å, which is slightly longer than O-H bond length at equilibrium and found that the D-O-D angle is 5° larger than in an isolated water molecule.[21] Chidambaram proposed a structure where a deuteron is 0.04 Å off the O•••O axis and the O-D•••O moiety is bent by 6.8°. Hence, water molecules in ice have O-H distances and H-O-H angles very close to those in isolated molecules, which are 1.0 Å and 109.5° respectively.[22] Later studies of ice using NMR confirmed this structure proposed by Chidambaram.[22]

There are nine polymorphic types of ice including ice II, III, V, VI, VII, and VIII which are rhombohedral, tetragonal, monoclinic, tetragonal, cubic, and cubic with distances to nearest neighbours of 2.75-2.84, 2.76-2.80, 2.76-2.87, 2.81, 2.86, and 2.86 Å, respectively. All have disordered hydrogens except ice II.[20]

In liquid water, the tetrahedral ice lattice is still present but the distance to the nearest neighbour is 2.8 to 2.9 Å which is slightly longer than in ice. There is still 4.5 Å between each oxygen and the others which simply means that each water molecule is in the middle of four surrounding water molecules. There are three main important structural characteristics of liquid water, which are as follows. First, the orientation of hydrogen bond acceptor water molecules in the first coordination is more defined than in the two hydrogen bond donor water molecules. Second, the distance between water molecules in the first coordination shell is at 3.2-3.8 Å but is closer than the second shell which is at 4.5 Å. Lastly, the H-O•••O formed between two water molecules has the smallest angle with a mean of 57°. It is worth noting that the hydrogen bond angles are more sensitive to crystal changes than the hydrogen bond distance. The solute type can affect the hydrogen bond angle in different molecules. Polar solutes have the tendency to increase the population of the bent hydrogen bonds while the apolar solute decreases the population of the bent hydrogen bonds. The water-water hydrogen bond angle is also affected by the hydration heat capacity, the stability of the molecule as a function of temperature, of the solute whether it is a protein or an inorganic molecule where high hydration heat capacity means there are more linear hydrogen bonds and low hydration heat capacity implies that there are less linear hydrogen bonds.[23]

3.3 Detection of hydrogen bonds using IR spectroscopy

Infrared spectroscopy is one of the most used methods to study hydrogen bonding. When a hydrogen bond forms between two non-linear molecules, three degrees of rotational and another three degrees of transitional freedom are converted to six low-frequency intermolecular modes with vibrational wavenumber less than 400 cm^{-1}.[24] When an A-H•••B

hydrogen bond forms, the vibrational frequency will decrease to a lower frequency value, which is known as the red-shift.[24] The red-shift is then directly related to the lengthening and shortening of the H-bond and the bonding energy. Sharp and Vanderkooi[25] studied the vibrational frequencies of O-H bond, for different solutes, which arise from H-O-D decoupled from water (samples prepared from D_2O and H_2O). Some of the solutes that were used included sodium chloride, urea, and trimethylamine N-oxide (TMAO) where the lowest frequency shift was for TMAO and the highest was for sodium chloride indicating a stronger hydrogen bond formed with TMAO. Nucci et al.[23] studied ions that promote linear H-bonding where anions with higher negative charge were ranked higher. The OH stretch showed that it was linear for Mg^{2+} and bent for K^+, which indicates that due to the larger size of potassium, the hydrogen bond is weaker.

3.4 Solution-state ^{1}H NMR and why it is important in studying water

^{1}H NMR can provide valuable information that cannot be deduced from other methods. Using this method, one can extract the hydrogen bond chemical shift, dissociation and exchange times, relaxation, and the H position in hydrogen bond crystals.[20] First, the chemical shift is directly affected by the solvent and temperature in which a spectrum is acquired. As the hydrogen bond is formed, the ^{1}H NMR signal moves towards high chemical shift and as it breaks, the signal moves towards lower chemical shifts. Therefore, one can predict the chemical shift range expected based on the length and the strength of the hydrogen bond.[20] Second, in solution hydrogen bonded moieties usually show one proton resonance due to molecular motion. Ogg et al.[26] acquired a spectrum for anhydrous liquid ammonia and liquid ammonia which contained 10^{-7} mole fraction of water. The anhydrous

ammonia gave a triplet, which arises from the spin-spin interactions between each hydrogen and ^{14}N. This was not observed in liquid ammonia with a trace of water, which instead showed a singlet due to rapid transfer between the hydrogen in the water and ammonia. Hence, by reducing the temperature when acquiring the spectrum one can measure the hydrogen bond dissociation and exchange time. Third, measurements of viscosity as a function of relaxation can reveal valuable information on association or hydrogen bond formation. Since relaxation is dependent on the line width, the local environment including the hydrogen bond will alter that line width. Mays and Brady[12] observed behavioural changes in water on titanium dioxide such as immobilization when the coverage reaches one monolayer. It was observed using the line width that ice formed at higher coverages of titanium dioxide.

Quadrupolar nuclides such as ^{2}D, ^{14}N, ^{35}Cl, ^{37}Cl, and ^{17}O can be used to study hydrogen bonds since their non-zero quadrupolar coupling constant is sensitive to the electron distribution near the nuclei. Konski and Flautt[12] studied the quadrupole coupling constants of ammonia when they observe twelve percent decrease of the coupling constant upon the condensation of ammonia gas due to an increase in ionic character when hydrogen bond forms.

A study done by Wittebort et al.[27] looking at the molecular orientation in ice using proton and deuterium magnetic resonance revealed that dynamics are directly related to the broadening of the powder pattern. ^{2}H NMR spectra were acquired for D_2O using a solid-echo pulse sequence over a temperature range of 220 to 267 K. At 220 K, the spectrum is the broadest with a coupling constant of 216 kHz and asymmetry parameter of 0.1. Parameters are reduced to zero at the highest temperature due to molecular tumbling. The

spectra also changes with the correlation time and the activation energy over the temperature range. The activation energy determined using the correlation time and temperature is 13.3 kcal/mol.

Modig and Halle[28] studied the proton magnetic shielding in liquid water. As mentioned, due to molecular tumbling the magnetic shielding tensor is averaged. In this study, they measured the proton relaxation rate as a function of magnetic field on a water sample with variable temperature experiments over the range from 0° to 80° C. The relaxation measurements were obtained for an applied magnetic field range of 2.35 to 18.8 T on a sample of D_2O with 1% of H_2O. The shielding tensor has the same orientation as the ^1H-^{17}O dipole-dipole coupling tensor and therefore the two relaxation mechanisms involve the same orientational time correlation function. It was noted that when the water sample was enriched with ^{17}O, the ^{17}O will affect the relaxation of the protons in two ways: ^1H-^{17}O dipole-dipole coupling will contribute to R^{DD} which can be directly used to calculate the rotational correlation time of water molecules, and the addition of a scalar relaxation contribution, which is due to spin-spin coupling, $J(^1H\text{-}^{17}O) = 80$ Hz. It was determined that as the temperature was increased from 0° to 80° C, the rotational correlation time for the O-H bond in water decreased exponentially, the average proton shielding anisotropy linearly decreased, and the isotropic shielding linearly increased in liquid water. Their results also showed that the temperature dependence of the proton shielding anisotropy in water is four times stronger than that of the isotropic shielding.

3.5 Solid-state ^{1}H NMR

Huang et al.[29] studied the proton magnetic shielding for water in carbon nanotubes (CNT) using (GIPAW) computational methods. The calculations included the water's oxygen in the center of the CNT with one orientation where the O-H is parallel to the tube axis and the other where both of the O-H bonds are perpendicular to the axis tube. The largest change in the chemical shift upon the encapsulation of the water in the nanotube is by 22 ppm upfield in comparison to an isolated water molecule. The shielding for the proton in isolated water, the parallel component of the shielding tensor of the proton inside the carbon nanotube, and the perpendicular component of the shielding tensor of the proton inside the carbon nanotube are 30.12, 52.8, and 52.83 ppm respectively. Also, the shielding anisotropies spans were 16.95, 7.48, and 29.68 ppm for a proton in isolated water, the parallel component of the shielding tensor of the proton inside the carbon nanotube, and the perpendicular component of the shielding tensor of the proton inside the carbon nanotube, respectively. The study covered thermally average proton shielding for 34 water molecules inside two different CNT, with diameters of 11.0 and 15.0 Å. The isotropic shielding and the anisotropic shielding for liquid water are 48.5 and 25.3 ppm for tube with diameter 11.0 A° and 47.1 and 25.3 ppm for tube with diameter 15.0 Å. This shows that the difference in proton shielding between the two tubes is only 1.5 ppm which basically shows that the shielding is independent of the tube's size.

More recently, Lee et al.[30] studied the T_1 relaxation times for water in proton-exchange membranes: Aquivion E-87-05, Nafion 117, and sulfonated radal. It was determined that at low hydration levels of ^2H_2O, the molecular motion will be affected by the presence of the sulfonic acid groups in the membrane where the water is coordinated. On the

other hand, at high hydration levels, the effect on the mobility of water is dependent on the separation of hydrophilic/hydrophobic domains. These effects were directly measured using relaxation times. In all membranes, as the humidity increased, the T_1 relaxation times increased linearly. More recent publications used proton or deuterium magnetic resonance to study the water mobility inside membranes, since it provides valuable biological information.[31,32]

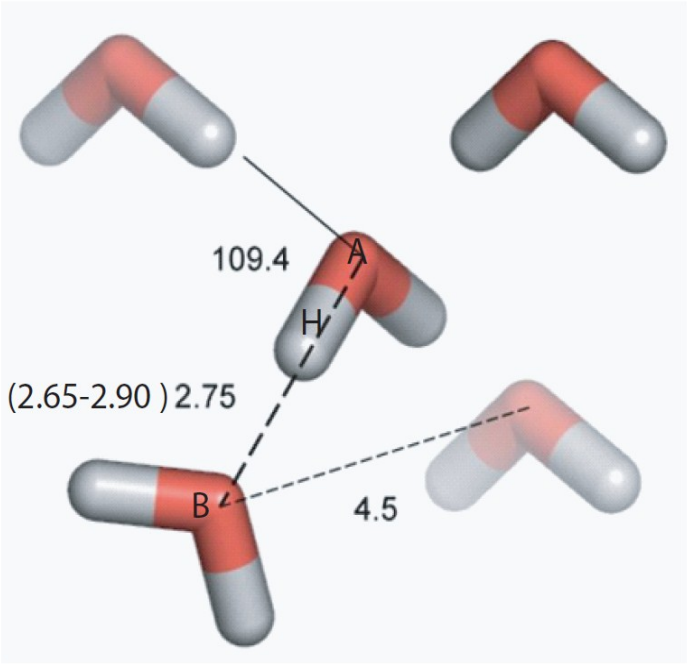

Figure 3.1: Structure of water. Adapted from "Water on the Half Shell: Structure of Water, Focusing on Angular Structure and Solvation," by K.A. Sharp and J.A. Vanderkooi, 2010, Accounts of Chemical Research, 43, p. 232. Copyright 2010 by American Chemical Society.

Wu et al.[33] studied the relationship between the proton chemical shift tensors and the hydrogen bond geometry using ^{1}H-^{2}H dipolar SSNMR for water molecules inside crystalline inorganic hydrates. The study first examines the difference between O-H•••O hydrogen bonds when they have linear versus bent geometries, implying that the ^{1}H CS tensors will be different based on this difference. The authors stated that the real interest behind this study

is that previous studies focused on only strong and medium strength H-bonds whereas this study focuses on weak hydrogen bonds, there is a wide range for hydrogen bond lengths, and the possibility of using this ^{1}H-^{2}H dipolar technique to study powdered samples instead of single crystals. In the solid state, water will undergo two fold jumps about the axis bisecting the H-O-H angle and therefore one of the principal components of the shielding tensors will be along this axis while the other two will be perpendicular to it. This is not to imply that the true values of these principal components are dependent on the molecular motion. The principal axis system will also have a different orientation for flipping and stationary water molecules in inorganic hydrates. Study of stationary water molecules, obtained experimentally by freezing the hydrate samples, revealed that the most shielded component for a stationary water molecule lies along the O_W•••O internuclear vector. Ten proton CS tensors of flipping water molecules in crystalline hydrates were obtained with δ_{iso} in the range of 5.0 to 10.5 ppm. The organic crystalline hydrates seemed to have lower chemical shifts in comparison to the inorganic crystalline hydrates. The CS tensors could not be related to the local geometry of the water molecules, which included the hydrogen bond distance and the H-O-H angle. This is due to the fact that there are more than just these contributions to the change in chemical shift. Computations done in this study reveal that as the hydrogen bond length increases, the proton chemical shift decreased, and $\delta_{11,}$ $\delta_{22,}$ and δ_{33} decreased, decreased, and increased respectively. It was concluded that as the hydrogen bond shortens, the parallel component of the proton CS tensor becomes more shielded and the perpendicular component becomes less shielded.

3.6 Literature review on ^{17}O NMR of ice

Groves and Pennington[34] studied ^{17}O spin-lattice relaxation times for pure ice, HCl doped ice, and KOH doped ice to determine the activation energies for proton motion of each. HCl and KOH atoms present an impurity and are located at interstitial or substitution sites such as when these impurities are frozen, they are mostly expelled from the ice phase but some remain to form impurity-solid-solution in ice. This is of interest because when ice is doped with HCl, the HCl will introduce D-defects, which are crystallographic defects arising from hydrogen bond having two protons or no protons instead of one, to the structure while the KOH dissociates to form protonic defects. The purposes behind comparing the relaxation times for all of the three samples are to determine how the dopants affect the proton arrangement and determine the activation energies which will yield information on the proton motion. Plotting ln $(1/T_1)$ versus $(\frac{1}{T})$ yields an activation energy of 3.4 kcal/mol, an activation energy of 4.4 kcal/mol, and an activation energy of 1.0 kcal/mole for pure ice, ice doped with HCl, and doped with KOH respectively. It was concluded that the data for pure ice follow the Arrhenius behaviour with an indication that there is proton motion along the hydrogen bond, the data for HCl-doped ice shows that the relaxation is reduced by addition of HCl and that the hydronium ion remains mobile even at 0 °C, and the data for the KOH-doped ice follow the Arrhenius equation with an acceleration in the effect of the correlation time has on the relaxation times as the concentration dependence increases.

Ba et al.[35] studied the reorientation of ice and tetrahydrofuran clathrate hydrate via line shape analysis of ^{17}O spin echo NMR. The quadrupolar coupling constant and the asymmetry parameters are 6.43 MHz and 0.935 for both ice and THF hydrate samples, which shows that the water molecule in both cases has a similar local environment. The kinetics

were also studied by observing the line shape and obtaining the relaxation times at different temperatures. The value of the quadrupolar coupling constant and asymmetry parameter are similar to those values obtained in other studies. Spiess et al.[36] obtained values of 6.66 MHz and 0.935 respectively for D_2O ice over the temperature range of 253 to 263 K. This is however different for ice II where the quadrupolar coupling constant and the asymmetry parameters are 6.893 MHz and 0.865, respectively. As mentioned, as the temperature increases the line shape becomes more featureless due to dynamic averaging. However, the results in this study reveal that the dynamics in THF hydrate are faster than the dynamics in pure ice. Similar to the previous study, the activation energies of proton motion for ice and THF hydrate were obtained using relaxation times and different temperatures, yielding 55.2 kJ/mol and 30.5 kJ/mol. The modeling of effects of dynamic exchange on central transition line shape shows that there are twelve different orientations of equal probability for single water molecule in either ice or THF hydrate. The population of these orientations is what determines the line shape of NMR spectrum with a slow region of reorientation exchange at the low temperatures and rate constants determines the line shapes at the high temperatures. Therefore, rapid reorientation exists between the tetrahedral and octahedral orientations and they are faster than the first-order line width while the second order central transition averages to an anisotropic shape. **Figure 3.2**, shown below, illustrates the line width for ice at different temperatures.

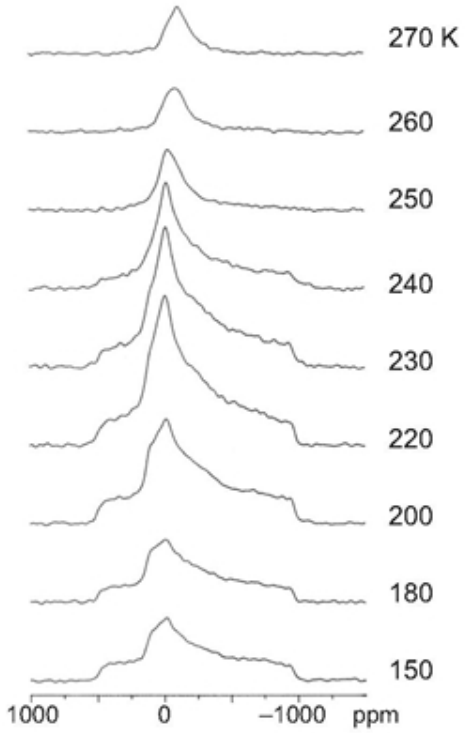

Figure 3.2: ^{17}O static NMR for 45% enriched water with ^{17}O obtained at different temperatures. Reprinted from "Water molecular reorientation in ice and tetrahydrofuran clathrate hydrate from line shape analysis of ^{17}O spin-echo NMR spectra," by Y. Ba, J.A. Ripmeester, and C.I. Ratcliffe, 2011, *Canadian Journal of Chemistry, 89*, p. 1057. Copyright 2011 by Canadian Journal of Chemistry.

3.7 Literature review on ^{17}O NMR

In this section, a selective literature review will be presented to give the reader an overview and background on ^{17}O NMR studies which have been done not just on hydrogen bonding or water in general but also on other systems which include organic materials, inorganic materials, and proteins to name a few. This will provide the reader with a broader perspective on the typical range of possible NMR parameters for different systems in order to be able to identify where the ^{17}O NMR of hydrates, studied in this work, fits into the bigger picture. **Table 3.1**, below, summarizes all the NMR parameters for several different functional groups.

Table 3.1: Summary of experimental results obtained for ^{17}O NMR parameters for different compounds based on findings from a literature review.[7, 36-42]

Compound	C_Q (MHz)	η	δ_{iso} (ppm)
Sodium(2-^{17}O) pyruvate	10.8 ± 0.2	0.48 ± 0.05	543 ± 1.0
Lithium (2-^{17}O) pyruvate	8.5 ± 0.5	1.0 ± 0.05	62 ± 1.0
(2-^{17}O) thymine	6.65	1.0	200
(2-^{17}O) Uracil	7.61	0.5	245
(2-^{17}O) Cytosine	7.20	0.70	230
(6-^{17}O) Guanine	7.10	0.80	230
((1-5)-^{17}O)Hydroxyl-chondrodite	2.3-2.7	0.2-0.3	14.3-63.0
((1-9)-^{17}O)Hydroxyl-clinohumite	2.4-2.8	0.2-0.3	14.5-63.5
((1-4)-^{17}O) avidin biotin	5.75-7.90	0.2-0.7	219-282
Orthorhombic triphenylphosphine	-4.59	0.01	45.1
Monoclinic triphenylphosphine	-4.57	0.03	53.0
2-aminoethane-1-sulfonic acid	-6.40	0.05	190.8
4-aminobutane-1-sulfonic acid	-7.23	0.16	170.4
nitroso-N,N-dimethylalinine•HCl	14.0	-	263
$ZnCl_2$(nitroso-N,N-dimethylalinine)$_2$	13.0	-	600

Zhu et al.[37] studied ^{17}O NMR of keto and gem-diol forms of α-keto acid derivatives where they measured the quadrupolar coupling and chemical shift tensors for both sodium pyruvate and lithium pyruvate enriched with ^{17}O. It is worth noting that in studies such as this one, MAS experiments are used to obtain the C_Q, η, and δ_{iso} and then these parameters are used as a starting point to determine the rest of the parameters using the static experiments. The ^{17}O static spectra for sodium pyruvate had a span of 1500 ppm which

showed that the carbonyl group had large ^{17}O chemical shift anisotropy. This was also confirmed by the presence of many sidebands in the MAS NMR spectra. The parameters obtained from the MAS spectra for C_Q, η, and δ_{iso} are 10.8 MHz, 0.48, and 543 ppm, respectively. The CS tensor was found, using static spectra, to have $\delta_{11,}$ $\delta_{22,}$ and δ_{33} of 1020 ppm, 640 ppm, and -40 ppm respectively. The δ_{11} is determined to lie along the direction of smallest QC tensor component V_{xx}, and δ_{22} coincides with largest QC tensor component V_{zz}. The ^{17}O static spectra for lithium pyruvate had a total width that was invariant of the magnetic field unlike the sodium pyruvate. The MAS spectra was used to determine the C_Q, η, and δ_{iso} which are 8.5 MHz, 1.0, and 62 ppm. As the data shows there is more symmetry about oxygen in both the ester and hydroxyl molecules and their charge distribution in comparison to the oxygen in sodium pyruvate. The CS tensor was found, using static spectra, to have $\delta_{11,}$ $\delta_{22,}$ and δ_{33} values of 140 ppm, 45 ppm, and 0 ppm, respectively. The study also used computational methods (GIPAW) to determine the NMR parameters for both compounds. Two different computational approaches were used; crystal lattice and the molecular cluster approach where the crystal lattice approach has a greater agreement with the experimental results than does the molecular cluster approach.

Another study by Wu et al.[38] looked at the solid-state ^{17}O NMR of *C*-nitrosoarene compounds along with computational calculations. The quadrupolar coupling constants for these organic compounds are on the order of 10 to 15 MHz which are considered the largest in comparison to other organic compounds studied previously. Also, the ^{17}O CS tensor has a high sensitivity towards the nitroso bonding scheme where the compound with the lowest CSA had a range of 250 ppm and the compound with the highest CSA has a range of 2800 ppm which are the largest values for CSA in other organic compounds studied. The four

compounds, all contained nitroso-N,N-dimethylalinine (NODMA), studied are NODMA.HCl, $ZnCl_2$ $(NODMA)_2$, $SnCl_2Me_2$ $(NODMA)_2$, and NODMA had a (N=O) distances of 1.374 Å, 1.304 Å, 1.296 Å, and 1.247 Å while their δ_{iso} values are 263 ppm, 600 ppm, 717 ppm, and 1200 ppm which shows that there is an increasing trend in δ_{iso} as the distance decreases. Computational studies were also done to further examine the dependence of the ^{17}O NMR on binding of nitrosoarene to metals. The results reveal that κ^1-N-binding, κ^1-O-binding, and η^2-NO-binding have δ_{iso} of 1300 ppm, 1000 ppm, and 400 ppm while the C_Q values are 14 MHz, 13 MHz, and 11 MHz respectively. This is a strong indication that the NMR tensors can be used as sensitive probes for binding modes of these compounds to metal complexes. The CS tensor components are determined to be dependent on the molecular orbital mixing and the π-bond order for the four compounds. The ^{17}O CS tensor components were as a function of π-bond order of the compounds which revealed a strong linear increase for δ_{11}, a medium linear increase for δ_{22} and a weak linear increase for δ_{33} as the π-bond order increased.

Kong et al.[39] studied variable temperature ^{17}O NMR to evaluate the molecular dynamics of organic solids, sulfonic acids. The three compounds, 2-aminoethane-1-sulfonic acid (T), 3-aminopropane-1-sulfonic acid (HT), and 4-amino-butane-1-sulfonic acid (ABSA) all exist as zwitterionic structures where the SO_3^- in the NH_3^+-R- SO_3^- is involved in hydrogen bonding. The C_Q values ranged between -7.23 and -6.40 MHz, the η ranged from 0.05 to 0.16 and the δ_{iso} ranged from 170.4 to 190.8 ppm which shows that there is not much difference in the local environment of the three compounds due to similar parameters. For the first compound T, slow motion existed at room temperature while the line shapes for HT and ABSA showed significant change upon cooling. Even though the δ_{iso} range is only 20

ppm there is a clear correlation between the δ_{iso} and the hydrogen bond length where the δ_{iso} decreases as the H-bond length decreases. Finally, the activation energies for the three compounds were calculated using the relaxation times data at different temperatures to give 48 kJ/mol, 42 kJ/mol, and 45 kJ/mol for T, HT, and ABSA respectively. These activation energies have a direct correlation with the SO_3 rotation angle where the activation energies for the sulfonate group rotations increase in the order of T> HT> ABSA.

Martel et al.[40] used ^{17}O MAS NMR to study actinide bearing compounds to provide insight into 5f chemistry. The compounds studied by NMR and single-ion model calculations are ThO_2, UO_2, NpO_2, PuO_2, and AmO_2. Due to the cubic fluorite these compounds exist in, the oxygen-17 quadrupolar coupling constants for all of them are zero since there is no EFG and a featureless signal is observed. The chemical shifts are 576 ppm, 717 ppm, 475 ppm, 54 ppm, and -754 for ThO_2, UO_2, NpO_2, PuO_2, and AmO_2 respectively. It is worth noting that the static and MAS NMR spectra for AmO_2 differed by 100 ppm because of the sensitivity of paramagnetic shift to the sample temperature. The static spectra for AmO_2 have a line broadening which is due to presence of two phases and local disorder in the sample. There is no clear relation between the number of 5f electrons and the T_1 relaxation times but it is worth noting that ThO_2 which has zero 5f electrons has T_1 of 1000 s which much larger than the other compounds which have T_1 on order of 0.001 to 1 s, which is a characteristic of paramagnetic samples. The paramagnetic shifts are generally dependent on the bond angle and cation-anion distance but in the case of these dioxide compounds, it is only the distance of actinide-oxygen distance. There is a decreasing trend in the An-O distance as the paramagnetic shift decreases. The calculated and measured values were in good agreement.

Zhu et al.[7] studied ^{17}O NMR of large protein-ligand complexes to determine the relevant NMR parameters and T_1 relaxation times. The ^{17}O T_1 relaxation times for these proteins are typically on the order of milliseconds, which means that data may be collected rapidly. In this study, sensitivity-enhancement methods were used such as double-frequency sweep (DFS), rotor-assisted population transfer (RAPT), and hyperbolic secant (HS) pulses. The two protein complexes studied are avidin biotin and transferrin-Al-oxalate, where simulations show that C_Q, η, and δ_{iso} are 5.8 MHz, 0.4, and 270 ppm for avidin biotin and 5.75 MHz, 0.7, 219 ppm for O1, 6.30 MHz, 0.6, 237 ppm for O2, 7.70 MHz, 0.45, -240 ppm for O3, and 7.90 MHz, 0.2, and 282 ppm for the oxalate. The parameters obtained for the oxalate complex are very similar to those obtained in solution implying a similar behaviour in both phases. The overall agreement between the experimental and calculated values is good but the authors report the need for further exploration of NMR crystallography on both proteins, specially the oxalate. The T_1 and T_2 are obtained for biotin and oxalate to be 3.5 and 0.5 milliseconds for biotin and 6.6 and 2.4 milliseconds for the oxalate, acquired at 11.7 T. Moreover, the T_1 decreased as the applied magnetic field increased which indicates that there is a rapid motion in the solid proteins due to the presence of methyl groups in the vicinity of the ligand. Finally, the techniques used such as HS produced a factor of two in sensitivity enhancement to obtain better spectra.

Griffin et al.[41] studied the ^{17}O NMR of hydrous magnesium silicates in search for proton dynamics and to relate the proton geometry to the NMR parameters. The compounds studied are hydroxyl-chondrodite (five oxygen sites) and hydroxyl-clinohumite (nine oxygen sites) which are model molecules to the incorporation of water in the earth`s upper mantle. The structures of both minerals consist of *n* forsterite-like layers where the first compound

has $n = 2$ and the second has $n = 4$. It is worth noting that diffraction studies of the two compounds reveal that for each of the hydroxyl group, there are two distinct H sites where the adjacent protons are 1 Å apart. This indicates that the occupancy of the two H sites has an unstable configuration. Two ^{17}O experiments were acquired which are multiple-quantum magic angle spinning (MQMAS) and satellite transition magic angle spinning STMAS. The MQMAS spectrum shows four resonances with intensity ratio of 1:1:1:1 for the first compound, which corresponds to four sites. The hydroxyl oxygen was not observed which is due to larger quadrupolar coupling constant and the slow MAS rate used. For the second compound, the spectrum showed five resonances with intensity ratio of 2:2:2:1:1. These peaks correspond to eight sites with overlap with three of them. Again, the hydroxyl oxygen is not observed due to the large quadrupolar coupling constant. The calculated spectra, produced using parameters calculated using DFT methods (CASTEP), on the other hand predict many more peaks for both compounds including the hydroxyl oxygen which showed up at a higher chemical shift while the other sites were close to each other. This indicates that all the oxygen sites are not equivalent and are in different local environments due to the variety of arrangements of the hydroxyl groups. The study then considers the interchange between the hydroxyl groups and two inequivalent protons at rate larger than the ^{17}O isotropic shifts that result from interchange of proton positions. It is this case that will lead to only four resonances observed in the spectra. The isotropic chemical shifts of both compounds ranged from 25 to 45 ppm. There is a direct relation between the Si-O distance and the ^{17}O chemical shifts; as the distance increases, δ_{iso} increases. The STMAS experiment for both compounds displayed broadening of most resonances making it less useful than the MQMAS experiments. Finally, the parameters obtained from the MQMAS NMR spectrum

indicate that the occupancy disorder of the hydroxyl protons is not static in nature, at room temperature.

Wu et al.[42] conducted an important study on the ^{17}O NMR of nucleobases. Combined simulations of static and MAS NMR spectra reveal the C_Q, η, and δ_{iso} values for all oxygen sites in thymine, uracil, cytosine, and guanine. The crystal structure of thymine shows two oxygen sites where the thymine molecules are linked through C=O•••H-N bonds. One of its oxygen sites forms two H-bonds while the other does not hydrogen bond and therefore the C=O distances are 1.246 Å for the site that H-bonds and only 1.193 Å for the site with no hydrogen bond. The C_Q is therefore different in both sites where it is 6.65 MHz for the site that forms a hydrogen bond and 8.40 MHz for the free site. In uracil, only one of the site H-bonds while the other stays free where both of the C=O distances are exactly the same. The linkage here between the uracil molecules are through amide bonds and the C_Q values for the two sites are 7.61 and 7.85 MHz. The similarity in the two values is due to two competing factors, which are that amide groups have larger C_Q at the oxygen site and that direct involvement in hydrogen bonding reduces the C_Q. It is worth noting that the chemical shift difference between the two oxygen sites in thymine is 125 ppm while it is 30 ppm in uracil. Unlike thymine and uracil, cytosine has long C=O distance which is 1.241 Å which indicates strong hydrogen bonding. The cytosine molecules are not just linked through C=O•••H-N but also through N-H•••N hydrogen bonds. The oxygen site in cytosine has a C_Q of 7.20 MHz and δ_{iso} of 230 ppm. Guanine has C=O•••H-N and N-H•••N hydrogen bond lengths of 2.93 and 2.83 Å, respectively. There is a good agreement between both experimental and calculated spectra.

Bryce et al.[43] studied the ^{17}O NMR of monoclinic and orthorhombic polymorphs of triphenylphosphine oxide. The two polymorphs had similar C_Q values, which are -4.59 MHz and -4.57 MHz for monoclinic and orthorhombic forms, respectively. However, the ^{17}O CS tensor spans for both of the polymorphs are 135 ppm and 155 ppm which indicates distinct difference. The MAS NMR experiments showed that the second-order quadrupolar interaction dominates, which can be observed in the central transition line shapes, and a *J* coupling between the phosphorus and the oxygen with a value of 150 Hz. The η is less than 0.01 and 0.03 while the δ_{iso} is 45.1 and 53.0 ppm for both the orthorhombic and monoclinic polymorphs, respectively. Again these variations are little and the asymmetry parameter gives a clear indication of the symmetry at the oxygen site. These results suggest that the quadrupolar parameters are sensitive to the CS and the highly shielded chemical shifts indicate little paramagnetic contribution to the shielding tensor.

CHAPTER FOUR:
RESULTS AND DISCUSSION

In this chapter, I present five crystalline hydrates' ^{17}O SSNMR spectra acquired under both static and MAS conditions. The five crystalline hydrates are: (1) oxalic acid dihydrate, (2) barium chlorate monohydrate, (3) lithium sulphate monohydrate, (4) potassium oxalate monohydrate, and (5) sodium perchlorate monohydrate. In this chapter, the experimental data, including the ^{17}O NMR static and MAS spectra and their NMR parameters obtained from fitting software WSolids, for each of the five crystalline hydrates will be presented. The crystal structures for all of these compounds are also discussed in search for a correlation between the structural geometry and the NMR parameters. ^{17}O MAS experiments at different temperatures were done for barium chlorate monohydrate to determine the effect of the temperatures on the NMR parameters. Computational methods were used for oxalic acid dihydrate and barium chlorate monohydrate to study the effect of structural changes such as hydrogen bond distance, water angle (H-O-H), and water molecule distance on the NMR parameters. Here, oxalic acid dihydrate serves as a molecular model for organic acid hydrates while barium chlorate monohydrate serves as a molecular model for inorganic hydrates. Further computational studies looked at the calculated parameters for metal-water complex in a vacuum and by changing the structural changes to determine the effect on the NMR parameters. The experimental procedure followed for preparing samples, X-ray, and SSNMR will be shown first.

4.1 Experimental methods

4.1.1 Sample preparation using ^{17}O enriched water

^{17}O enriched water was purchased from Sigma Aldrich and Cortnecnet. All five hydrates are available commercially from Sigma Aldrich (natural abundance in ^{17}O). The water used in experiments discussed in this work has 40% ^{17}O-enrichment. Five samples of different inorganic crystalline hydrates were enriched with ^{17}O water where some were 20% enriched while others are 10% enriched. 0.25 grams of the powder samples were dissolved in 0.6 ml water. After all solids dissolved, the samples were left for four hours at room temperature to allow the water to evaporate; subsequently, the enriched solid from each sample was collected for NMR experiments. Another technique was used whereby the powder was dissolved in the water and the solution was heated in an open vial containing the sample at a temperature of 85 °C for 30 minutes, yielding the desired products. However, at 110 °C, the enriched water escaped from the sample which was confirmed using X-ray. Different temperatures were used for the same duration to determine the most ideal procedure where the lower the temperature, the longer it took for the water to evaporate. This was tested with regular non-enriched water. It is worth noting that if the sample was left on a hot plate over night at temperatures ranging from 85 °C to 105 °C, it was observed that the enriched water escaped the sample.

4.1.2 X-ray experimental methods

The X-ray data were obtained at University of Ottawa using basic powder x-ray diffraction (PXRD) technique. 200 mg of each five samples were grinded lightly (to avoid loss of water) and placed on a metal sample holder. It is worth noting that some of the compounds such as sodium chlorate hydrate lost its water molecule when grinded too hard.

The measurements were obtained using RIGAKU Ultima IV diffractometer with Cu Kα radiation which has a wavelength of 1.54184 Å and Bragg-Brentano geometry. The data were collected 1.0°/min. for a diffraction angle from 5° to 80°. Shown below are the X-ray results for oxalic acid hydrate (**Figure 4.1**), potassium oxalate hydrate (**Figure 4.2**), sodium perchlorate hydrate (**Figure 4.3**), and lithium sulphate hydrate (**Figure 4.4**).

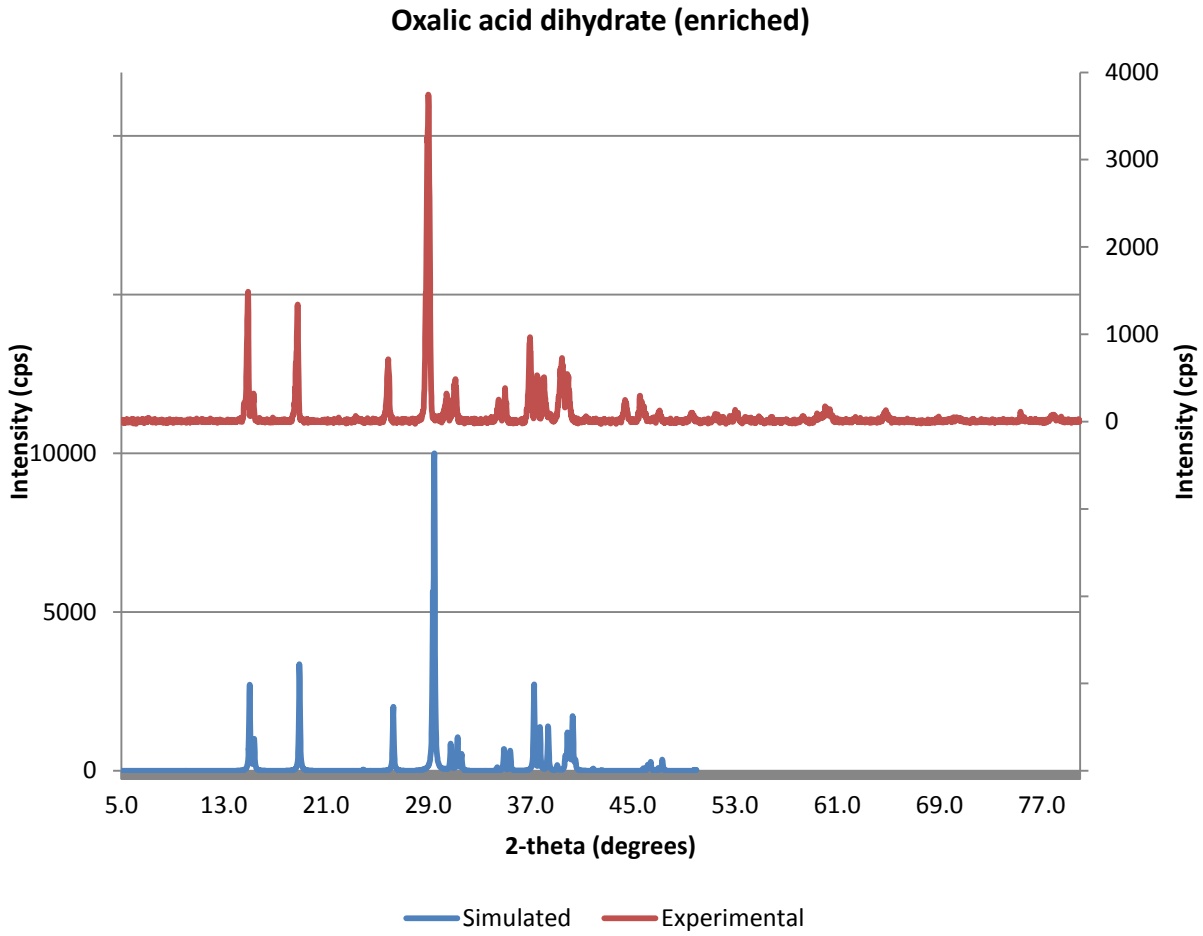

Figure 4.1: X-ray result for oxalic acid dihydrate.

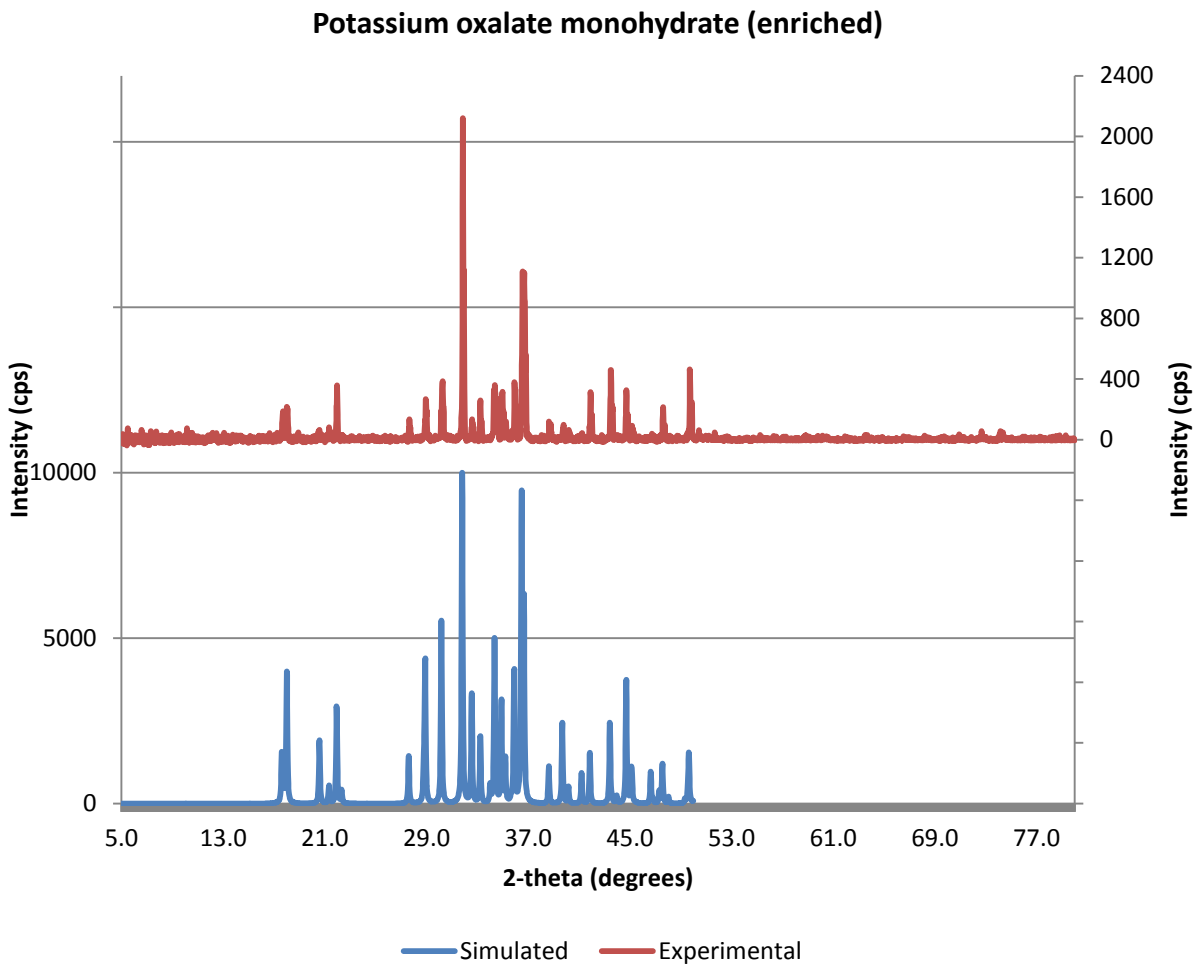

Figure 4.2: X-ray result for potassium oxalate monohydrate.

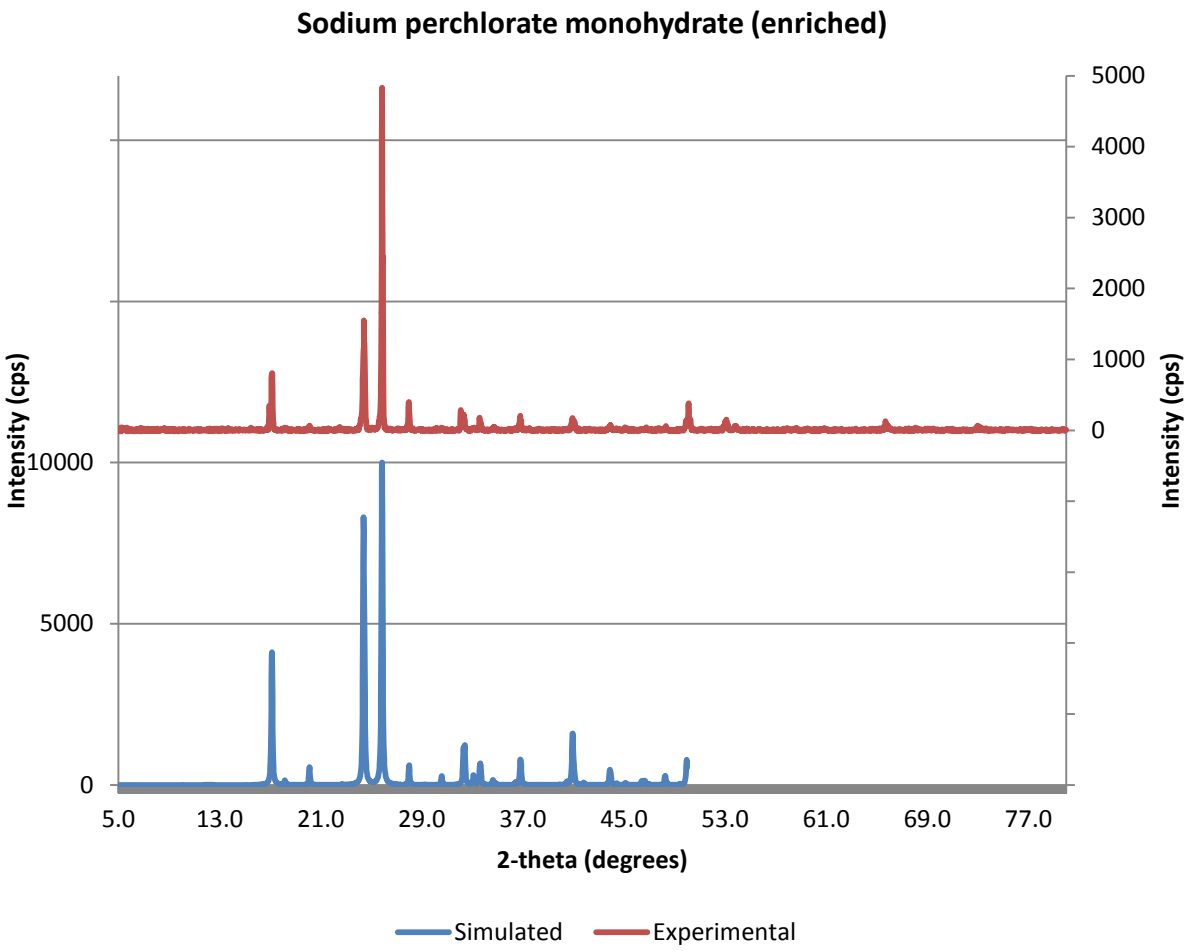

Figure 4.3: X-ray result for sodium perchlorate monohydrate.

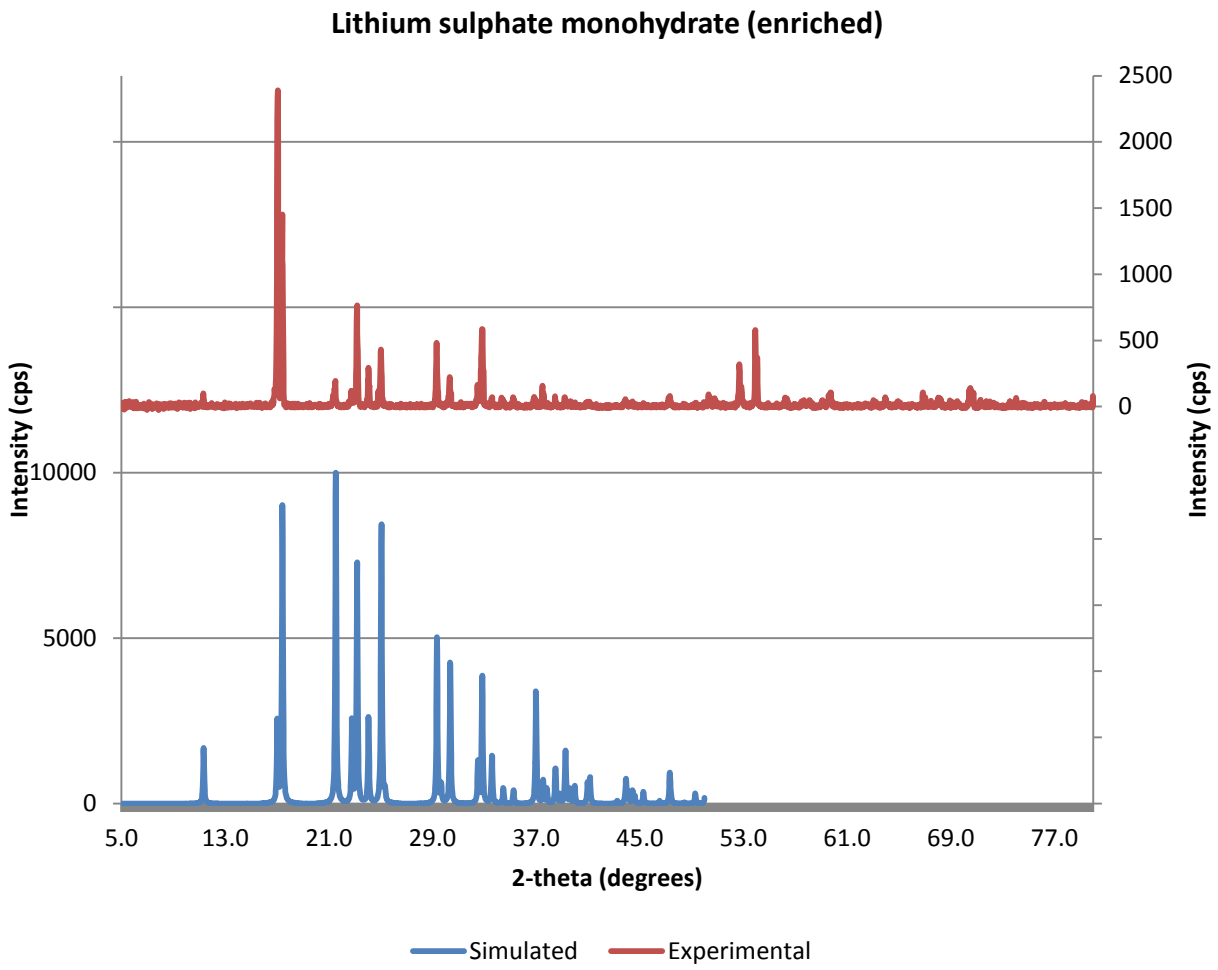

Figure 4.4: X-ray result for lithium sulphate monohydrate.

4.1.3 SSNMR experimental methods

The data were acquired at 9.4 T and 21.1 T at the University of Ottawa and the National Ultrahigh-field NMR Facility for Solids in Ottawa. The spectra acquired at ^{17}O Larmor frequencies of 54.25 MHz and 121.94 MHz, respectively. At 9.4 T, a 4 mm Bruker HX MAS probe was used to obtain powder spectra for all samples while at 21.1 T, a home built 5 mm static and 4 mm Bruker HX MAS were used to obtain the static and MAS spectra for the powder samples as well. ^{1}H decoupling was used at both fields for all samples. All

samples were referenced to water and the 90° pulse was calibrated to be 2.07 μs. At 9.4 T, the spectral width is 200 MHz, the dwell time is 2.5 μs, and the time domain is 1024 points. At 21.1 T, the spectral width is 250 MHz, the dwell time is 2.0 μs, and the time domain is 2048 points. It is worth noting that for oxalic acid dihydrate (3 sites) higher power was used to excite the entire spectrum. The SSNMR line shapes were fitted using WSolids simulation software to be able to analyze the CSA and quadrupolar effects and to also obtain the NMR parameters. First, the quadrupolar coupling constant, asymmetry parameter, and isotropic chemical shifts were determined using MAS experiments which are then used as starting point to determine the rest of the parameters using static experiments.

4.1.4 Computational methods

GIPAW DFT calculations were performed using version 4.1 of CASTEP NMR which is implemented in Material Studio 4.0 where the single X-ray structure crystallographic information files were input into the program for each of the compounds: oxalic acid hydrate, sodium perchlorate hydrate, lithium sulphate hydrate, barium chlorate hydrate and potassium oxalate hydrate. These crystal structures were used with optimized hydrogen positions. The ultra-fine cutoff energies were used for all of the GIPAW calculations. CASTEP and the cut-off energies, based on the unit cell, predominated the k-points fields for all calculations. On the fly pseudo-potentials were used for all atoms. The generalized gradient approximation (GGA) exchange correlation functional of Perdew, Burke, and Ernezerhofe (PBE) was employed for all the hydrates. The structure crystallographic information for each hydrate was obtained from the existing neutron diffraction literature.[44,45,47,48,49] Isolated molecular models for both barium chlorate hydrate, oxalic acid hydrate and metal-water systems using Gaussian 09 package. The basis sets used

for all Gaussian calculations were 6-311G + (d, p) with B3LYP as hybrid functional. All the geometries chosen for all of these systems covered a range which is directly related to the actual geometries obtained from the neutron diffraction structures. It is worth noting that CASTEP is the chosen method for this study because, as mentioned, it is GIPAW DFT based which means it accommodates for the intramolecular interactions and therefore it is appropriate for one to compare with experimental results.

4.2 ^{17}O static and MAS NMR spectra: Results

4.2.1 Oxalic acid dihydrate

The crystal structure for oxalic acid dihydrate, studied by Sabine et al.[44] using neutron diffraction, shows that the hydrogen bond (O_w-H•••O) length is 1.917 Å forming with the nearest oxygen in the acid. The distance between the oxygen in the water and the nearest oxygen in the acid is 2.864 Å. The water angle (H-O-H) is determined to be 105.9° and the (O_W-H•••O) angle for both hydrogen are 157° and 167° respectively. These geometry parameters are shown in **Figure 4.5**, as an illustration.

The ^{17}O MAS NMR experiment revealed that for this compound the C_Q, η, δ_{iso} values were 7.01 ± 0.01 MHz, 0.77 ± 0.03, and 8.0 ± 1.0 ppm, respectively. As shown in the spectra in **Figure 4.6**, three sites are observed, which represent the water oxygen (most shielded), the hydroxyl oxygen (middle shielded), and the carbonyl oxygen. The rest of the parameters were obtained by fitting the ^{17}O static NMR spectra using the three mentioned values as a starting point where the span, skew, δ_{11}, δ_{22}, and δ_{33} were determined to be 26.0 ± 4.0, -0.6 ± 0.3, 12.0 ± 4.0, 2.8 ± 2.0, and -2.5 ± 2.0 respectively (see **Figure 4.7**). CASTEP/GIPAW calculations show an overestimation of the C_Q, and the δ_{iso} which were -

8.25 MHz and 14.4 ppm with a good agreement for the η which is 0.75. The full comparison between the experimental and the calculated values is shown in **Table 4.1**. Not surprisingly, the static spectra also show the three sites with a clear distinction in the NMR parameters such as chemical shifts with no suspected overlaps. The chemical shifts, quadrupolar coupling constants, and asymmetry parameters for the hydroxyl and the carbonyl oxygen obtained from this experiment lie in the same range as ones studied elsewhere (see **Table 3.1**).

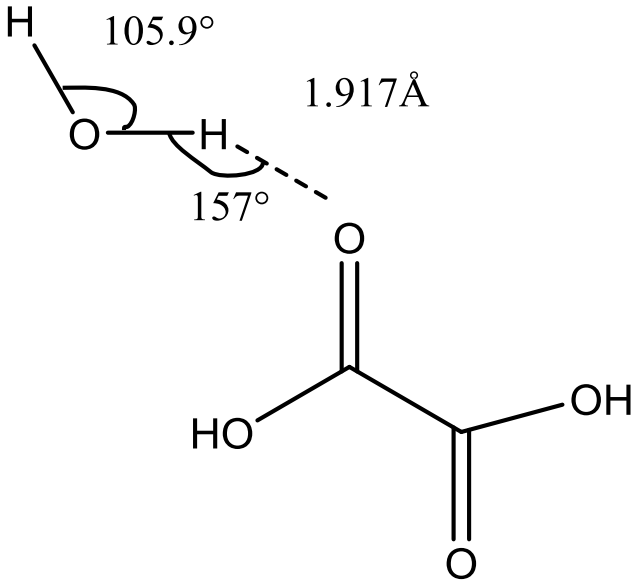

Figure 4.5: The geometrical parameters describing the hydrogen bond for oxalic acid hydrate, i.e., O_w-H•••O distance, H-O-H angle and O_w-H•••O angle.

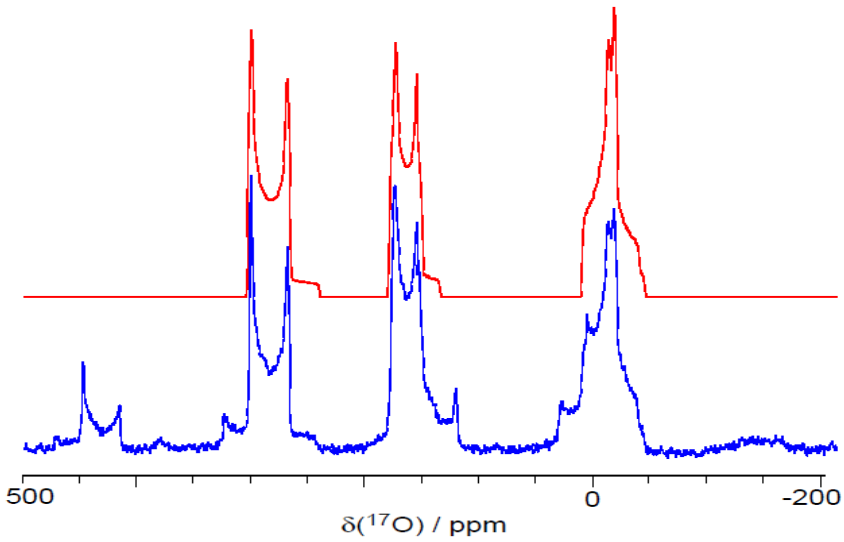

Figure 4.6: ^{17}O MAS NMR for oxalic acid hydrate experimental (blue) and simulated (red) obtained at 21.1 T.

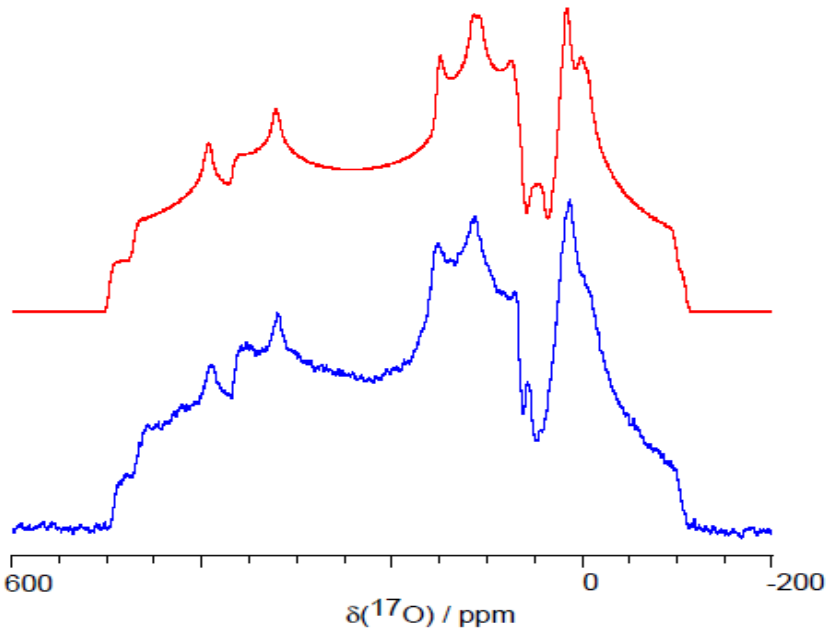

Figure 4.7: ^{17}O static NMR for oxalic acid hydrate with experimental (blue) and simulated (red) obtained at 21.1 T.

4.2.2 Barium chlorate monohydrate

The crystal structure for barium chlorate monohydrate shows that the hydrogen bond distance (O_w-H•••O) in this inorganic hydrate is 1.99 ± 0.01 Å while the distance between the water oxygen and the oxygen in the chlorate ion is 2.891 ± 0.014 Å. The water angle (H-O-H) is 110.7° and the hydrogen bond angle (O_W-H•••O) is 163.6°. The Ba-O distance has a distance of 2.76 Å which indicates that there is a shorter distance between the metal to the water than between the two water molecules. It is also worth noting that the Ba-O_w-H angle is 163.7° and that the dihedral angle of H-O_w-H-O is surprisingly high which can be due to the electrostatic interactions of the hydrogen and its neighbouring atoms.[45]

According to the ^{17}O MAS NMR spectra shown in **Figure 4.8**, there is one site present which represents the water molecule with C_Q, η, δ_{iso} values of 6.91 ± 0.03 MHz, 0.98 ± 0.02, and 19.6 ± 1.5 ppm, respectively. The rest of parameters were obtained by fitting the ^{17}O static spectra, shown in **Figure 4.9**, using the three mentioned values as a starting point where the span, skew, δ_{11}, δ_{22}, and δ_{33} were determined to be 30.0 ± 1.0 ppm, -0.42 ± 0.08, 36.7 ± 2.0 ppm, 15.5 ± 3.0 ppm, and 6.6 ± 2.0 ppm, respectively. CASTEP calculations show an overestimation of the C_Q, and underestimation of the η and δ_{iso} values, which were 8.75 MHz, 0.87 and 12.2 ppm, respectively. The full comparison between the experimental and the calculated values is shown in **Table 4.1**. It is also worth noting that CASTEP underestimated the principal components of the CS tensor, which were 29.6 ppm, 3.40 ppm, and 3.02 ppm, respectively.

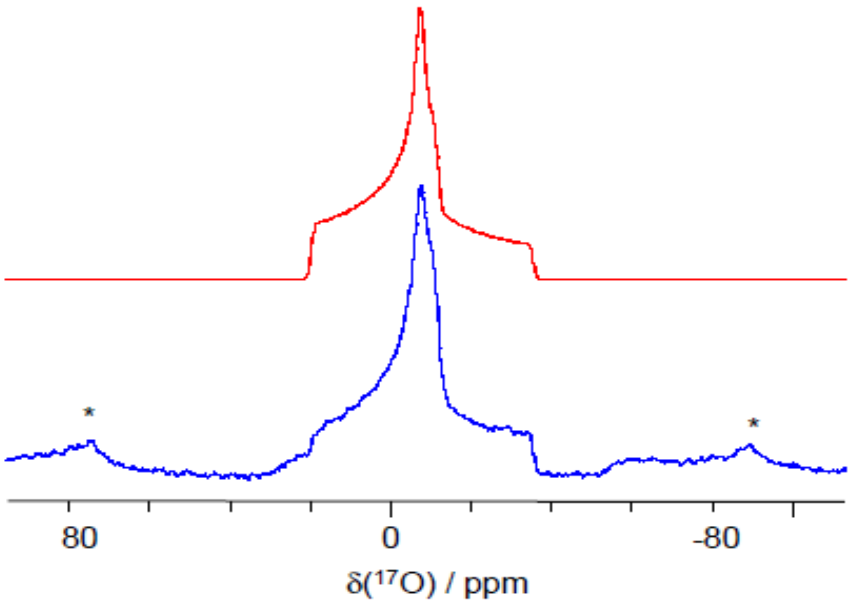

Figure 4.8: ^{17}O MAS NMR for barium chlorate hydrate with experimental (blue) and simulated (red) obtained at 21.1 T.

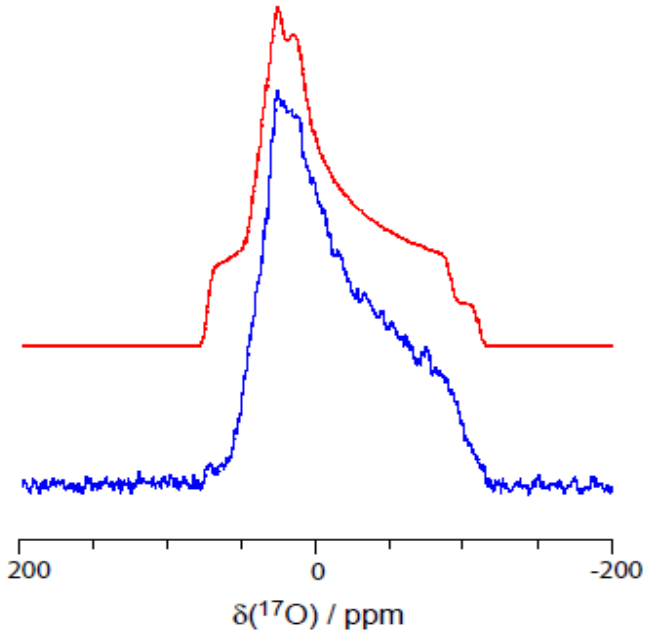

Figure 4.9: ^{17}O static NMR for barium chlorate hydrate with experimental (blue) and simulated (red) obtained at 21.1 T.

4.2.3 Lithium sulphate monohydrate

The crystal structure for lithium sulphate monohydrate has been known since 1934 by Zieglar.[46] Furthermore, the neutron diffraction of this compound studied by Smith et al.[47] revealed that the hydrogen bonding existing between water molecules is weak, where the distance between oxygen in one water and the oxygen in its neighbouring molecule is 2.95 ± 0.01 Å while the water-water angle (O_w-H-$O_{w'}$) is far from being linear (151°) which implies bent hydrogen bonding instead of linear hydrogen bonding. It is also worth noting that the O-H distance in this crystal is longer in comparison to other inorganic hydrates, which is 1.00 ± 0.04 Å and 0.95± 0.02 Å while it is 0.926 and 0.958 Å and in barium chlorate monohydrate. The H-O-H angle is also determined to be 110.7° ± 2.1°. This value is the same for barium chlorate monohydrate which also had an H-O-H angle of 110.7°.

According to the ^{17}O MAS NMR spectra shown in **Figure 4.10**, there is one site present which represents the water molecule. C_Q, η, δ_{iso} were determined to be 6.85 ± 0.02 MHz, 0.85 ± 0.01, and -8.0 ± 1.0 ppm, respectively. The rest of parameters were obtained by fitting the ^{17}O static spectra, shown in **Figure 4.11,** using the three mentioned values as a starting point where the span, skew, δ_{11}, δ_{22}, and δ_{33} were determined to be 48.0 ± 1.0 ppm, 0.2 ± 0.08, 14.4 ± 2.0 ppm, -4.8 ± 2.0 ppm, and -33.6 ± 4.0 ppm, respectively. CASTEP calculations show an overestimation of C_Q and for η which were -8.15 MHz and 0.93, respectively. Overall, there is also close agreement between the experimental and calculated ^{17}O chemical shift tensor components.

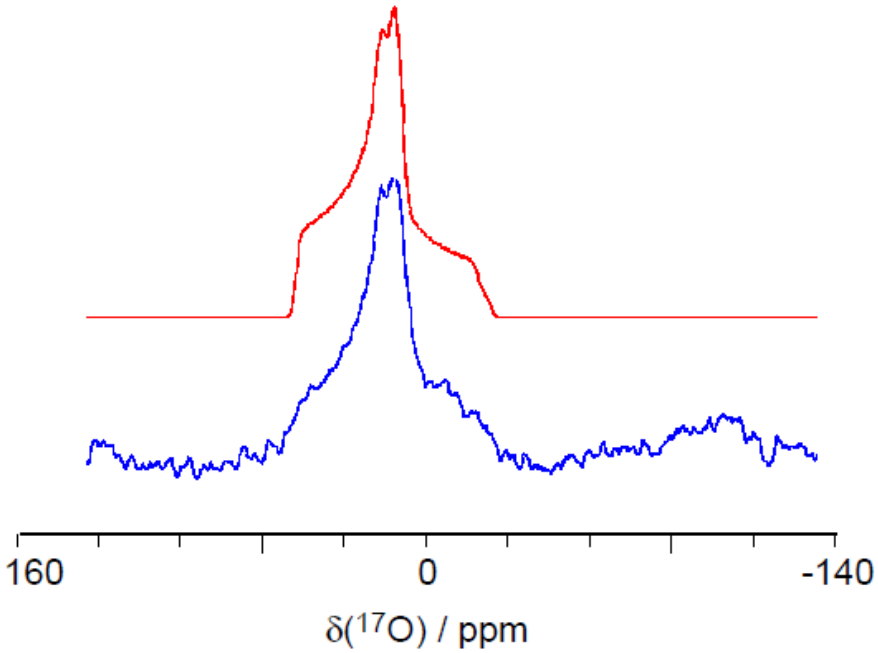

Figure 4.10: ^{17}O MAS NMR for lithium sulphate monohydrate with experimental (blue) and simulated (red) obtained at 21.1 T.

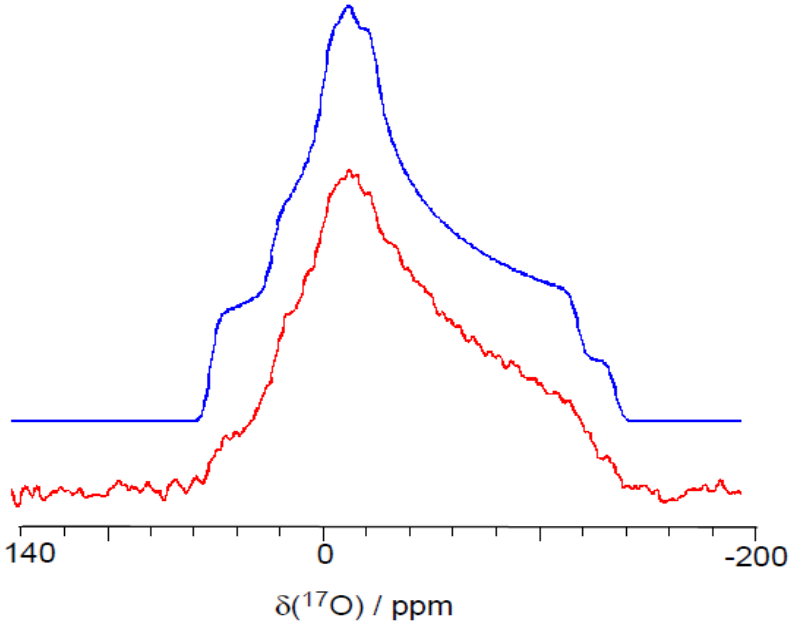

Figure 4.11: ^{17}O static NMR for lithium sulphate monohydrate with experimental (blue) and simulated (red) obtained at 21.1 T.

4.2.4 Sodium perchlorate monohydrate

A neutron diffraction study of sodium perchlorate monohydrate by Berglund et al.[48] revealed disorder in the crystal structure due to large amplitudes of thermal vibration in the two protons of the water lying in the same plane. The amplitudes were 0.53 Å and 0.46 Å for the protons with angles 0.4° and 3.7° out of the water plane. The O-H bond distances for the hydrogen atoms are considered short at 0.905 Å and 0.935 Å. The hydrogen bond distances (O_w-H•••O) were all approximately around 2.4 Å. The H-O_w-H angle is also determined to be 105.7° which indicates that the H-O_w-H is less affected by the thermal motion where in free water the H-O_w-H angle is 104.5°.

According to the MAS spectra shown in **Figure 4.12**, there is one site present that represents the water molecule with C_Q, η, and δ_{iso} determined to be 7.39 ± 0.04 MHz, 0.75 ± 0.02, and -15.0 ± 0.3 ppm, respectively. The rest of parameters were obtained by fitting the ^{17}O static spectra, shown in **Figure 4.13**, using the three mentioned values as a starting point where the span, skew, δ_{11}, δ_{22}, and δ_{33} were determined to be 27.0 ± 1.0 ppm, 0.95 ± 0.08, -5.8 ± 2.0 ppm, -6.5 ± 2.0 ppm, and -32.8 ± 2.0 ppm, respectively. CASTEP calculations show an overestimation of the C_Q and for underestimation of η and δ_{iso} which are 8.75 MHz, 0.89 and -31.6 ppm. It is worth noting that CASTEP calculations for the Euler angles were not in good agreement with the experimental results, nor were the chemical shift tensors. By far, the asymmetry parameter is the lowest for this hydrate, which will later be discussed. The correlation between the calculated and experimental values decreases from δ_{11} to δ_{33}.

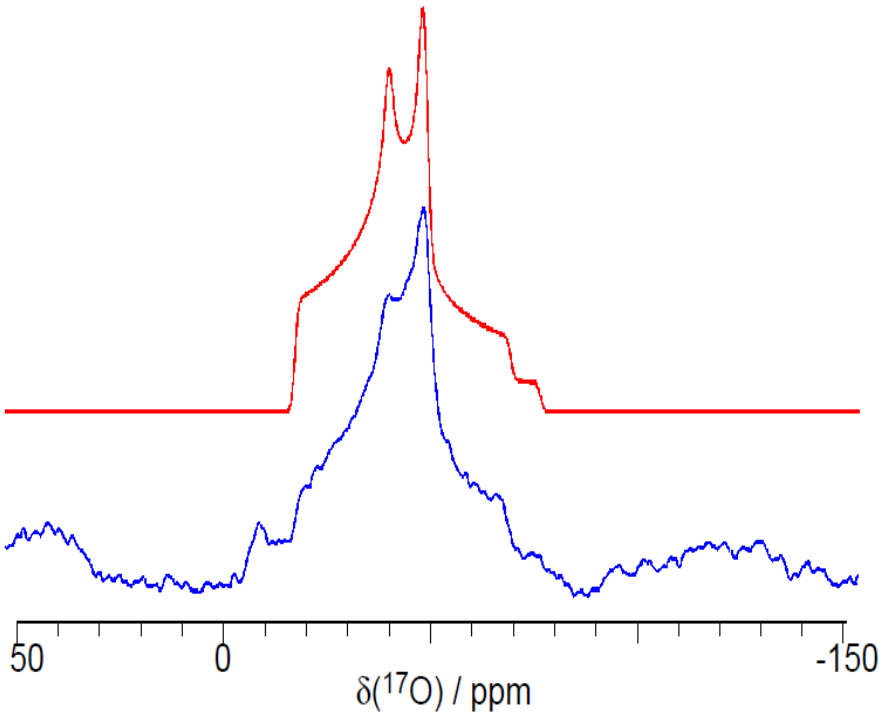

Figure 4.12: ^{17}O static NMR for sodium perchlorate monohydrate with experimental (blue) and simulated (red) obtained at 21.1 T.

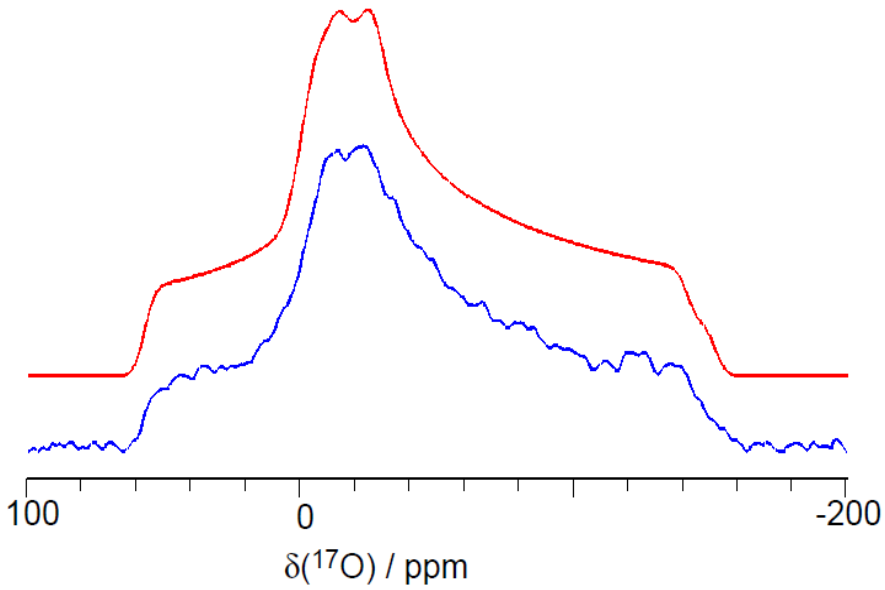

Figure 4.13: ^{17}O static NMR for sodium perchlorate monohydrate with experimental (blue) and simulated (red) obtained at 21.1 T.

4.2.5 Potassium oxalate monohydrate

The crystal structure for potassium oxalate monohydrate studied by Sequeira et al.[49] using neutron diffraction, shows that the hydrogen bond distance is 2.75 Å. The hydrogen bond angle (O_w-H•••O) is 169.6° which makes it close to linear, and the H-O_w-H angle is 107.6° which is approximately the average of the H-O_w-H angles for the other crystalline hydrates in this study (range 105.6° to 110.6°). The thermal motion for the oxygen in the water molecule is observed to be larger than the hydrogen atoms in the same plane. The coordination of the water molecule itself has two hydrogen atoms and two potassium atoms lying in a plane around the water oxygen.

The MAS spectra, shown in **Figure 4.14**, show that only one oxygen site is present, which represents the water molecule, with C_Q, η, δ_{iso} determined to be 6.75 ± 0.05 MHz, 1.0 ± 0.02, and 0.8 ± 0.2 ppm, respectively. The rest of parameters were obtained by fitting the ^{17}O static spectra, shown in **Figure 4.15**, using the three mentioned values as a starting point where the span, skew, δ_{11}, δ_{22}, and δ_{33} were determined to be 60.0 ± 2.0 ppm, 0.22 ± 0.05, 28.6 ± 2.0 ppm, 5.2 ± 2.0 ppm, and -31.4 ± 2.0 ppm, respectively. It is clear to say that in this case, there was no water exchange as only oxygen from water site is showing in spectra. It is worth noting that the span is largest for this hydrate in comparison to the others. CASTEP calculations show an overestimation of the C_Q with a value of -7.5 MHz, which is by far the closest parameter to the experimental result in comparison to the other hydrates. The CASTEP calculations are also in a good agreement for η and δ_{iso} which are 0.93 and 4.2 ppm.

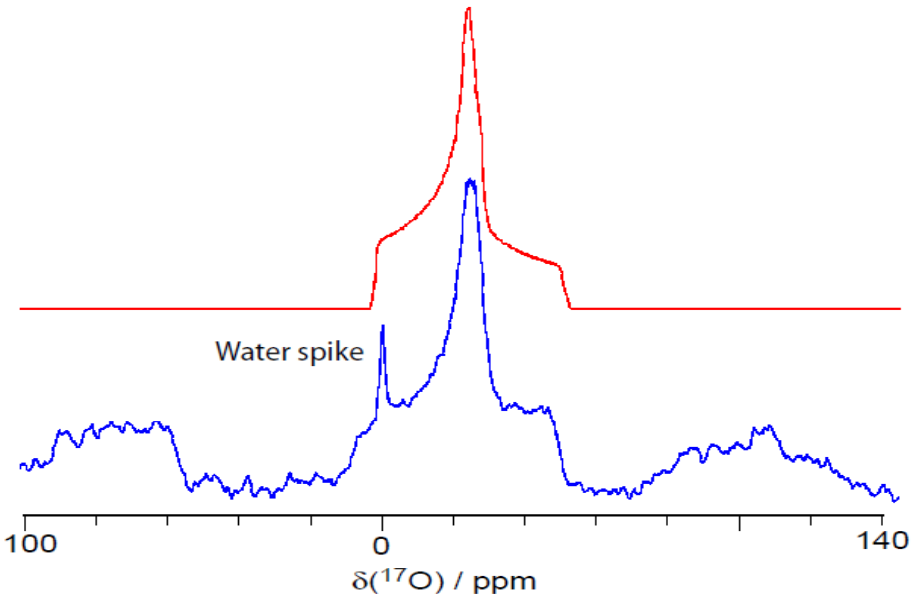

Figure 4.14: ^{17}O MAS NMR for potassium oxalate monohydrate with experimental (blue) and simulated (red) obtained at 21.1 T.

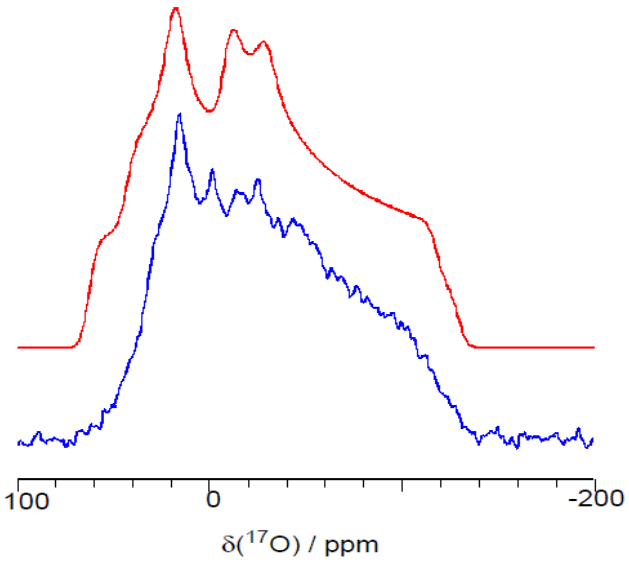

Figure 4.15: ^{17}O static NMR for potassium oxalate monohydrate with experimental (blue) and simulated (red) obtained at 21.1 T.

4.3 Variable temperature ^{17}O MAS NMR

^{17}O MAS NMR experiments were done for barium chlorate monohydrate at temperatures of -20 °C, 0 °C, 33 °C, and 40 °C to measure the impact the temperature has on the quadrupolar coupling constant, asymmetry parameter, and chemical shift. It is important to note that the biggest change in the quadrupolar coupling constant and asymmetry parameter is due to the temperature change from -20 °C to 0 °C where the quadrupolar coupling constant changes from 7.08 MHz to 6.94 MHz while the asymmetry parameter changes from 0.94 to 0.955. The impact is much less for temperature change above 0 °C where the quadrupolar coupling constant changes from 6.94 MHz to 6.88 MHz over 40 °C and the asymmetry parameter changes from 0.955 to 0.98 over the same range. The value of δ_{iso} on the other hand changed mostly from 18.9 to 19.8 ppm over a range of 0°C to 33 °C. This experiment served as a way to determine the changes in the NMR parameters upon increase in the temperature since the experimental parameters for all of the hydrates were obtained using MAS and static experiments where the samples were at higher temperatures during MAS experiments due to fast spinning. **Figure 4.16** shows the correlation between the temperature and quadrupolar coupling constant and shows the ^{17}O MAS NMR experiments for barium chlorate monohydrate at the four different temperatures. It is worth noting that drawing a linear trend line is in no way claiming that there is a linear trend expected but only to determine if there in an increase or a decrease relationship between the quadrupolar coupling constant and the temperature.

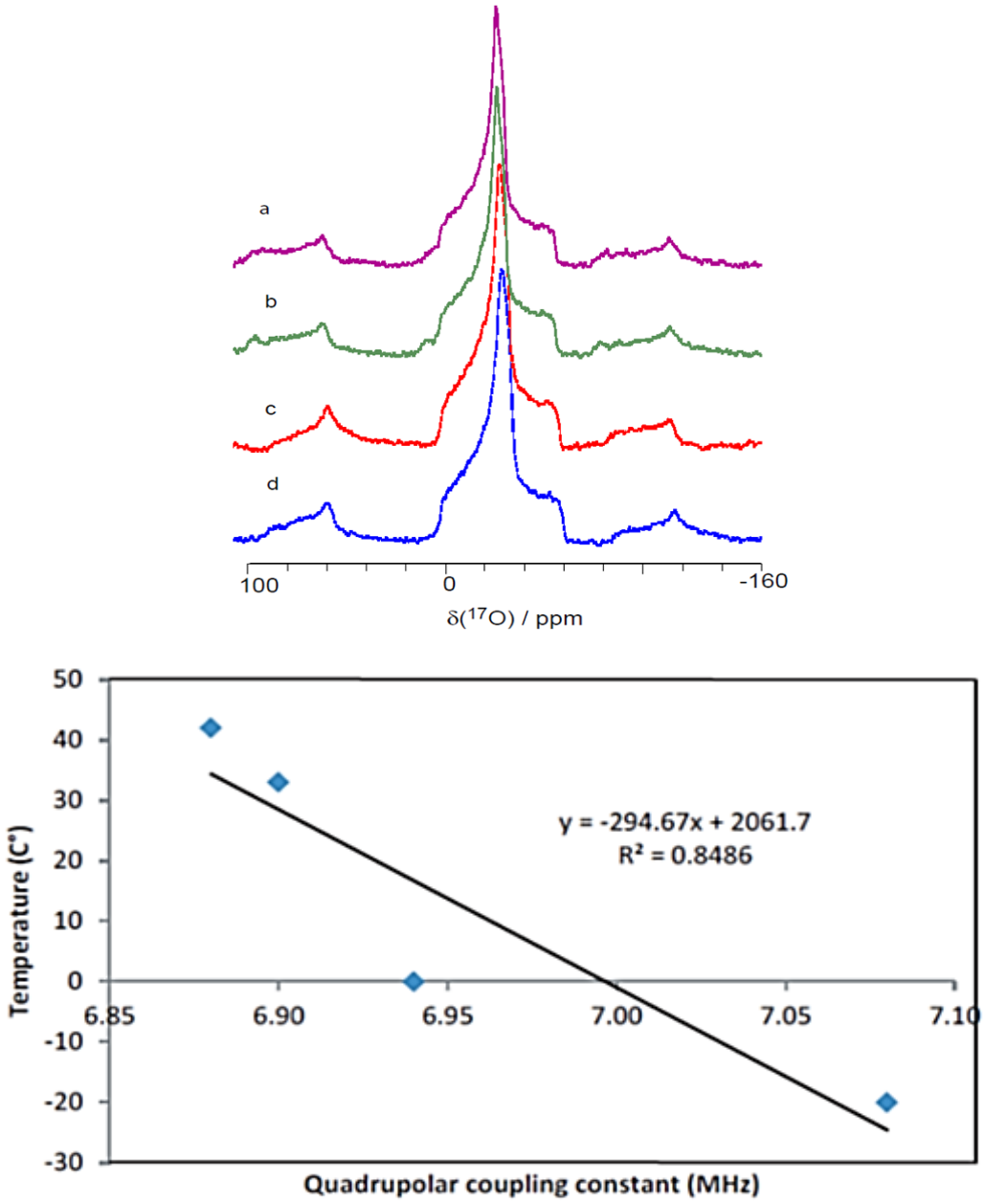

Figure 4.16: (Top) ^{17}O MAS NMR of barium chlorate hydrate at -20 °C(a), 0 °C(b), 33 °C(c), and 40 °C (d) obtained at 21 T, and (Bottom) the correlation between the temperature and quadrupolar coupling constant for barium chlorate hydrate.

Table 4.1: A summary of all NMR parameters obtained using experiments and computational calculations, along with the crystal information for each hydrate: (1) oxalic acid dihydrate, (2) barium chlorate monohydrate, (3) lithium sulphate monohydrate, (4) sodium perchlorate monohydrate, and (5) potassium oxalate monohydrate.

Compound	C_Q (MHz)		η		δ_{iso} (ppm)		δ_{11} (ppm)		δ_{22} (ppm)		δ_{33} (ppm)		κ		Ω (ppm)		R(H••O) (Å)	∠H-O-H (°)	∠O_w-H••O (°)
	Expt.	Calc.	Expt.	Calc.	Expt.	Calc.	Expt.	Calc.	Expt.	Calc.	Expt.	Calc.	Expt.	Calc.	Expt.	Calc.			
α-$(COOH)_2$•$2H_2O$	7.01± 0.01	-8.25	0.77± 0.03	0.75	8.0± 1.0	14.4	12.0± 4.0	41.5	2.8± 2.0	6.30	-2.5± 2.0	-4.48	-0.6± 0.3	-0.53	26.0± 4.0	46.0	1.91844[44]	105.7[44]	166.9[44]
$Ba(ClO_3)_2$•H_2O	6.91± 0.03	8.75	0.98± 0.02	0.87	19.6± 1.5	12.0	36.7± 2.0	29.6	15.5± 3.0	3.40	6.65± 2.0	3.02	-0.42± 0.08	-0.97	30.0± 1.0	26.6	1.991[45]	110.7[45]	163.6[45]
$NaClO_4$•H_2O	7.39± 0.05	-8.35	0.75± 0.02	0.89	-15.0± 0.2	-31.6	-5.78± 2.0	-10.0	-6.45± 2.0	-21.86	-32.8± 2.0	-62.85	0.95± 0.05	0.55	27.0± 2.0	52.7	2.152[48]	105.7[48]	155.5[48]
Li_2SO_4•H_2O	6.85± 0.02	-8.15	0.85± 0.01	0.93	-8.0± 1.0	-12.5	14.4± 2.0	14.6	-4.80± 2.0	-8.3	-33.6± 4.0	-44.6	0.2± 0.08	0.22	48.0± 1.0	59.2	1.99[47]	110.6[47]	153[47]
$K_2C_2O_4$•H_2O	6.75± 0.05	-7.5	1.0± 0.02	0.93	0.8± 0.2	4.2	28.6± 2.0	30.7	5.2± 2.0	30.7	-31.4± 2.0	-33.6	0.22± 0.05	0.53	60.0± 2.0	64.3	1.801[49]	107.6[49]	169.6[49]

4.4 Computational results

In this section, DFT calculation results are shown to illustrate the impact structural changes have on ^{17}O NMR parameters. These results include C_Q, η, δ_{iso}, δ_{11}, δ_{22}, and δ_{33} which are reported for an organic acid hydrate molecular model, oxalic acid hydrate, an inorganic hydrate molecular model, barium chlorate hydrate, and finally a simplified metal-water system. The metal water system consists of an unbonded metal cation and a water molecule in vacuum where the distance between the metal and the water is varied to determine the effect it will have on the NMR parameters. Note that the quadrupolar coupling constant, asymmetry parameter, and the isotropic chemical shift will first be shown for all the structural changes, and then the chemical shift tensor principal components will be shown second for all of the structural changes for each of these molecular models. Again it is worth noting that the use of linear trend lines in no way to imply that there is an expectation that these trends will be linear but the two major reasons are to determine if the trend is positive or negative and to measure the slope which will indicate the magnitude of impact the geometry has on each parameter.

4.4.1 Barium chlorate hydrate as an inorganic molecular model

Calculations were done using B3LYP/6-311+(d, p) for all of the results mentioned for barium chlorate hydrate. First, the quadrupolar coupling constant, asymmetry parameter, and isotropic chemical shifts were calculated as a function of the water angle (H-O-H), the hydrogen bond distance (O_w-H•••O), and the O-H distance to identify the trends in each of these parameters respectively. First, the H-O-H angle were set for range of 108 ° to 112 ° which keeps in perspective the range of the H-O-H angles in all of the hydrates. As shown in **Figure 4.17**, the quadrupolar coupling constant showed a decreasing trend from 9.21 MHz to

9.02 MHz, with a slope of -0.041 MHz/° as the H-O-H increased from 108 ° to 112 °. The asymmetry parameter increases from 0.79 to 0.91 with a slope of 0.03/°, as the H-O-H angle increases. The isotropic chemical shift has an increasing trend from -550 ppm to -260 ppm with a slope of 70.87 ppm/°.

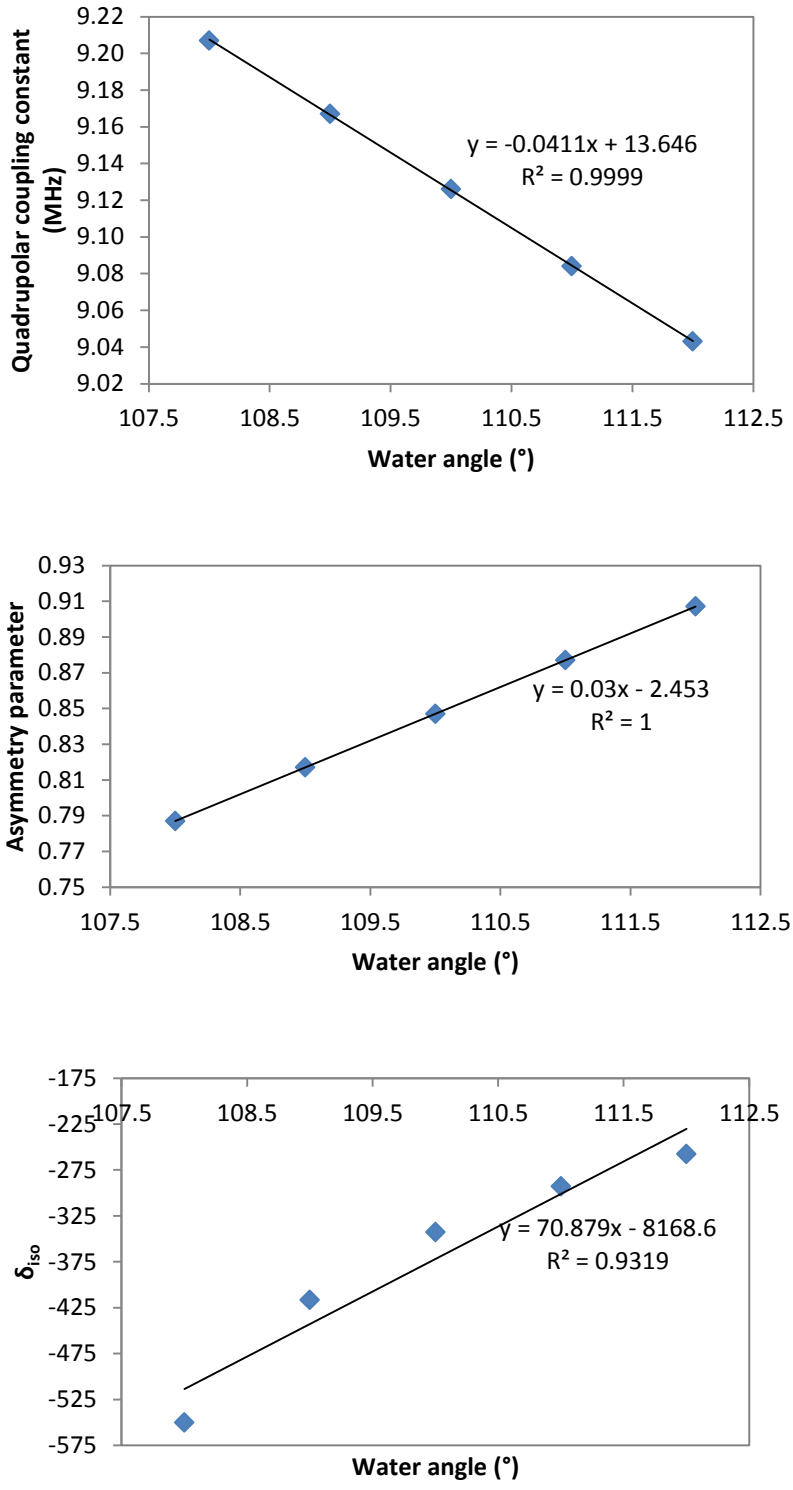

Figure 4.17: Computational results obtained using B3LYP/6-311+G (d,p) for the ^{17}O quadrupolar coupling constant, asymmetry parameter and isotropic chemical shift as a function of H-O-H angle for barium chlorate hydrate.

Next, the hydrogen bond (O_w-H•••O) distance was varied from 2.68 Å to 2.83 Å to observe the changes in the parameters. As shown in **Figure 4.18**, the quadrupolar coupling constant increased from 9.06 MHz to 9.21 MHz with a slope of 1.01 MHz/Å, while the asymmetry parameter decreases from 0.85 to 0.84 with a slope of -0.092/Å and the isotropic chemical shift increase from -900 ppm to -100 ppm with a slope of 4680 ppm/Å. This change in the isotropic chemical shift is considered really large as the hydrogen bond increases which shows that the parameter will be sensitive to the hydrogen bond distance.

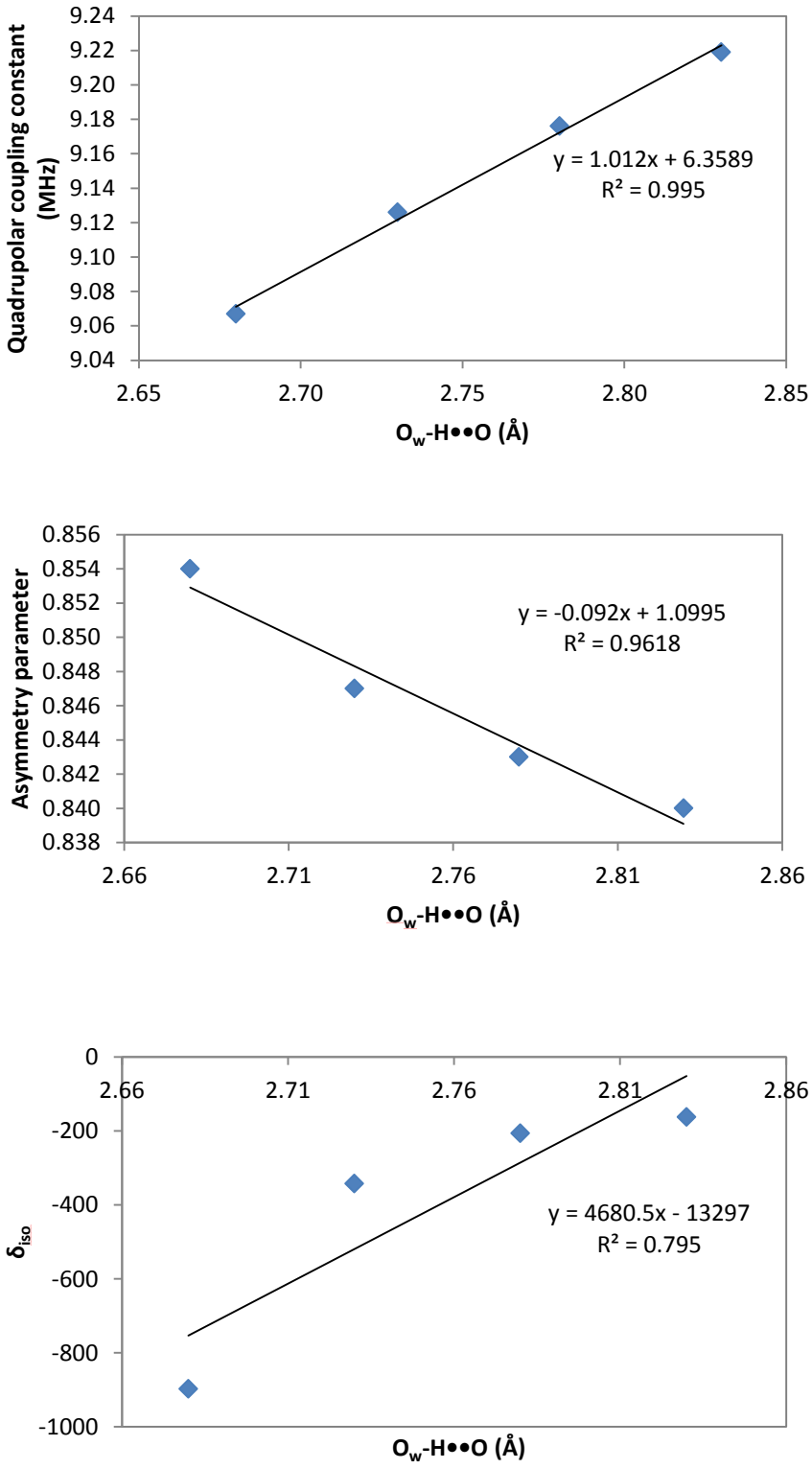

Figure 4.18: Computational results obtained using B3LYP/6-311+G (d,p) for the ^{17}O quadrupolar coupling constant, asymmetry parameter and isotropic chemical shift as a function of hydrogen bond distance for barium chlorate hydrate.

Thirdly, the O-H distance was varied from 0.89 Å to 0.99 Å where, as shown in **Figure 4.19**, the quadrupolar coupling constant had an increasing trend from 9.06 MHz to 9.26 MHz while the asymmetry parameter decreases from 0.857 to 0.83. The isotropic chemical shift had a decreasing trend over range of -260 ppm to -380 ppm with a slope of -1299 ppm/Å. These results show that the quadrupolar coupling constant is most sensitive to O-H distance, while the asymmetry parameter is as sensitive to the three structural changes, and the isotropic chemical shift is most sensitive to the hydrogen bond.

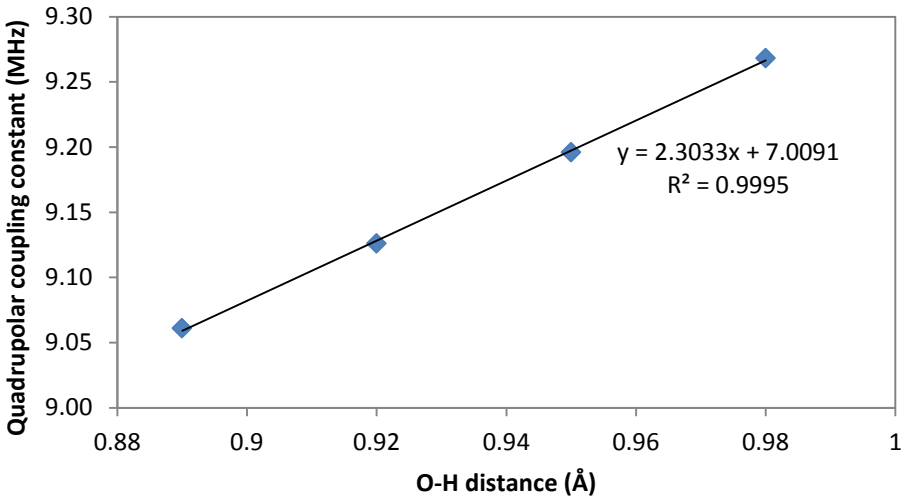

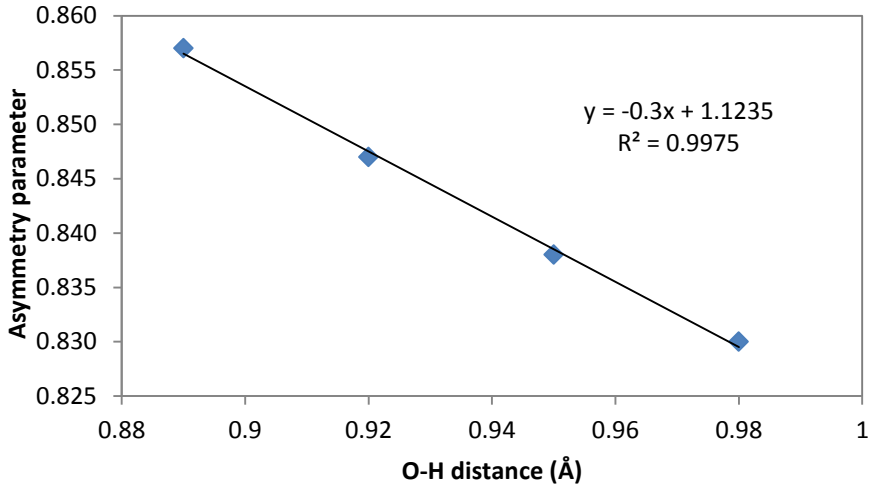

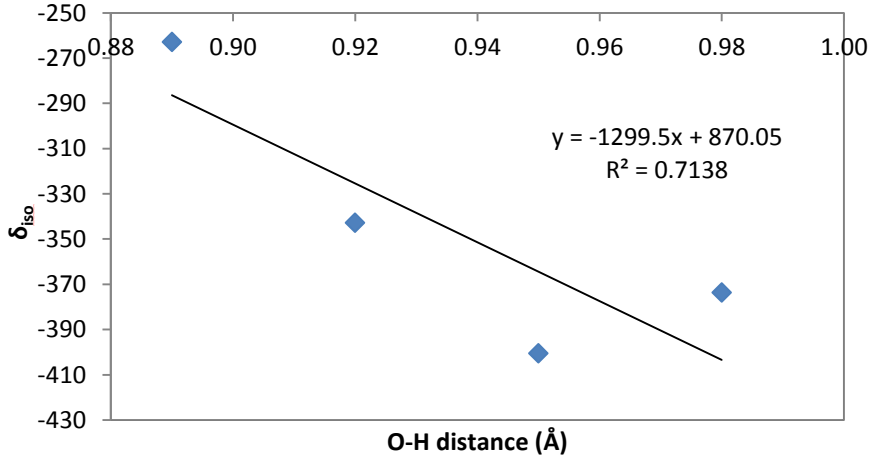

Figure 4.19: Computational results obtained using B3LYP/6-311+G (d,p) for the ^{17}O quadrupolar coupling constant, asymmetry parameter and isotropic chemical shift as a function of O-H distance for barium chlorate hydrate.

The chemical shift tensor principal components (δ_{11}, δ_{22}, and δ_{33}) were also calculated as a function of the H-O-H angle, O_w-H•••O, and O-H distances, shown in **Figure 4.20**. First, the value of δ_{11} (least shielded) had a decreasing trend over a range of 700 ppm to 375 ppm as the H-O-H increase with a slope of -85 ppm/º while δ_{22} increased over range of -222 ppm to -212 ppm with a slope of 2.73 ppm/º and δ_{33} increased over a range of -2200 ppm to -900 ppm with a slope of 295 ppm/ º.

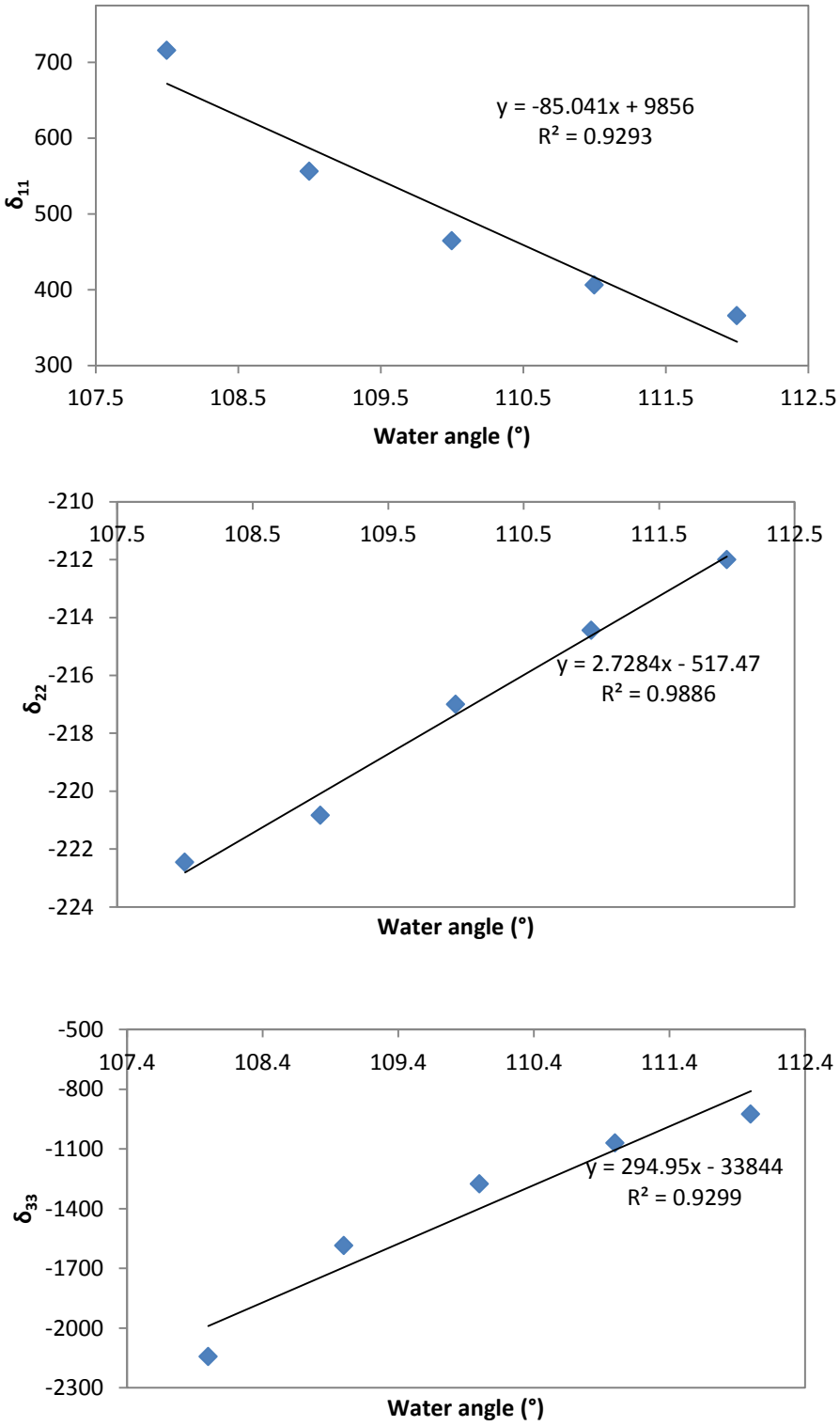

Figure 4.20: Computational results obtained using B3LYP/6-311+G (d,p) for the ^{17}O chemical shift principal components as a function of H-O-H angle for barium chlorate hydrate.

Second, the chemical shift tensors were calculated as a function of the hydrogen bond distance, shown in **Figure 4.21**, to determine its impact. The value of δ_{11} had a decreasing trend ranging from 1500 ppm to -100 ppm with a slope of -10471 ppm/Å which is considered a huge difference, the value of δ_{22} had increasing range of -200 ppm to 250 ppm with slope of 3718 ppm/Å and δ_{33} had an increasing range of -4000 ppm to 500 ppm with slope of 29303 ppm/Å. This difference in the third component is considered the largest out of all chemical shift tensors of all hydrates.

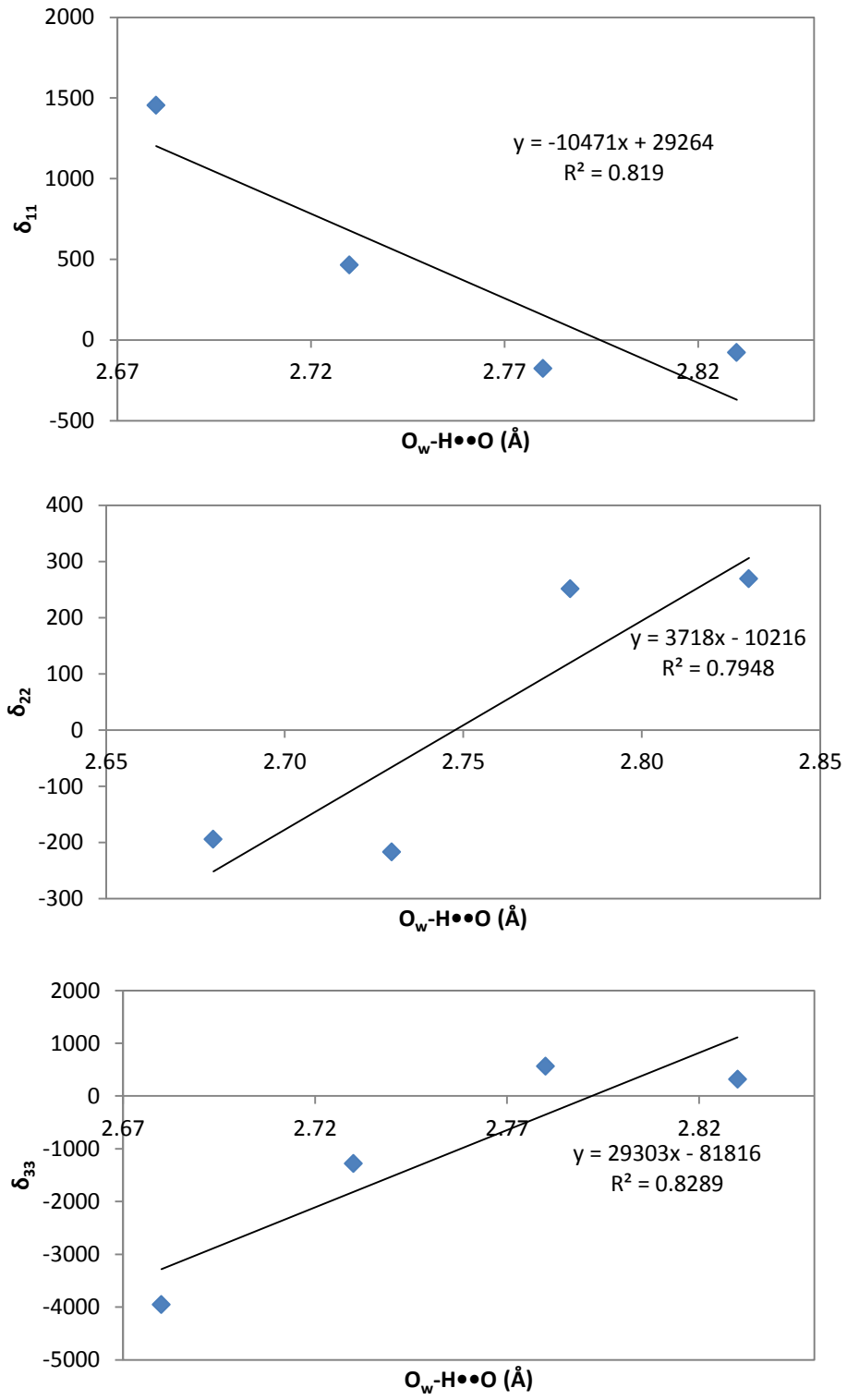

Figure 4.21: Computational results obtained using B3LYP/6-311+G (d,p) for the ^{17}O chemical shift principal components as a function of hydrogen bond distance for barium chlorate hydrate.

Thirdly, the chemical shift principal components are calculated as a function of O-H distance, as shown in **Figure 4.22** below. The value of δ_{11} increased over range of 300 ppm to 900 ppm with slope 6590 ppm/Å, while δ_{22} increased over range of -200 ppm to -50 ppm with slope of 1287 ppm/Å and δ_{33} decreased over range of -950 ppm to -1950 ppm with slope of -1171 ppm/Å.

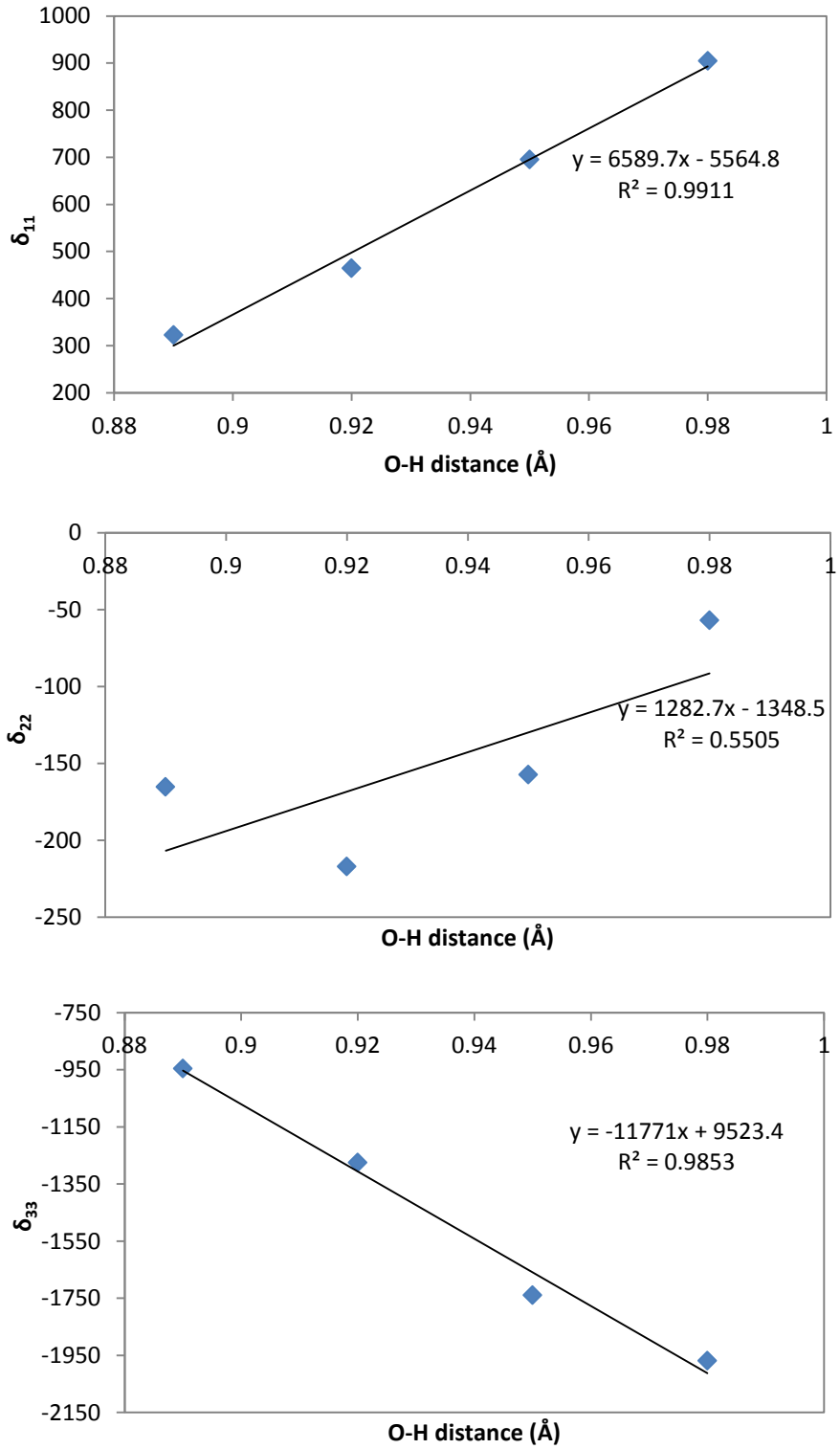

Figure 4.22: Computational results obtained using B3LYP/6-311+G(d,p) for the ^{17}O chemical shift tensors as a function of O-H distance for barium chlorate hydrate.

The largest difference in δ_{11} is due to O-H distance while the least impact is due to the H-O-H angle. Secondly, the largest impact on δ_{22} is also due to the O-H distance changes. It is worth noting that δ_{22} decreased as the H-O-H angle, hydrogen bond distance and the O-H distance increased. The value of δ_{33} is most sensitive to the hydrogen bond distance due to a large negative slope.

4.4.2 Oxalic acid dihydrate as an organic molecular model

Computational calculations were done using B3LYP/6-311+(d, p) for all of the results mentioned here. First, the quadrupolar coupling constant, asymmetry parameter, and isotropic chemical shifts were measured as a function of the water angle (H-O-H), the hydrogen bond distance (O_w-H•••O), and the O-H distance to identify the trends in each of these parameters, respectively. First, the H-O-H angle was varied from 103 ° to 109° which keeps in perspective the range of the H-O-H angles in all of the hydrates. As shown in **Figure 4.23**, the quadrupolar coupling constant showed a decreasing trend from 10.07 MHz to 9.91 MHz, with a slope of -0.036 MHz/° as the H-O-H increased from 103° to 109°. The asymmetry parameter increases from 0.86 to 0.99 with a slope of 0.029/°, as the H-O-H increases. The isotropic chemical shift has an increasing trend from -30.5 ppm to -30.0 ppm with a slope of 0.10 ppm/°.

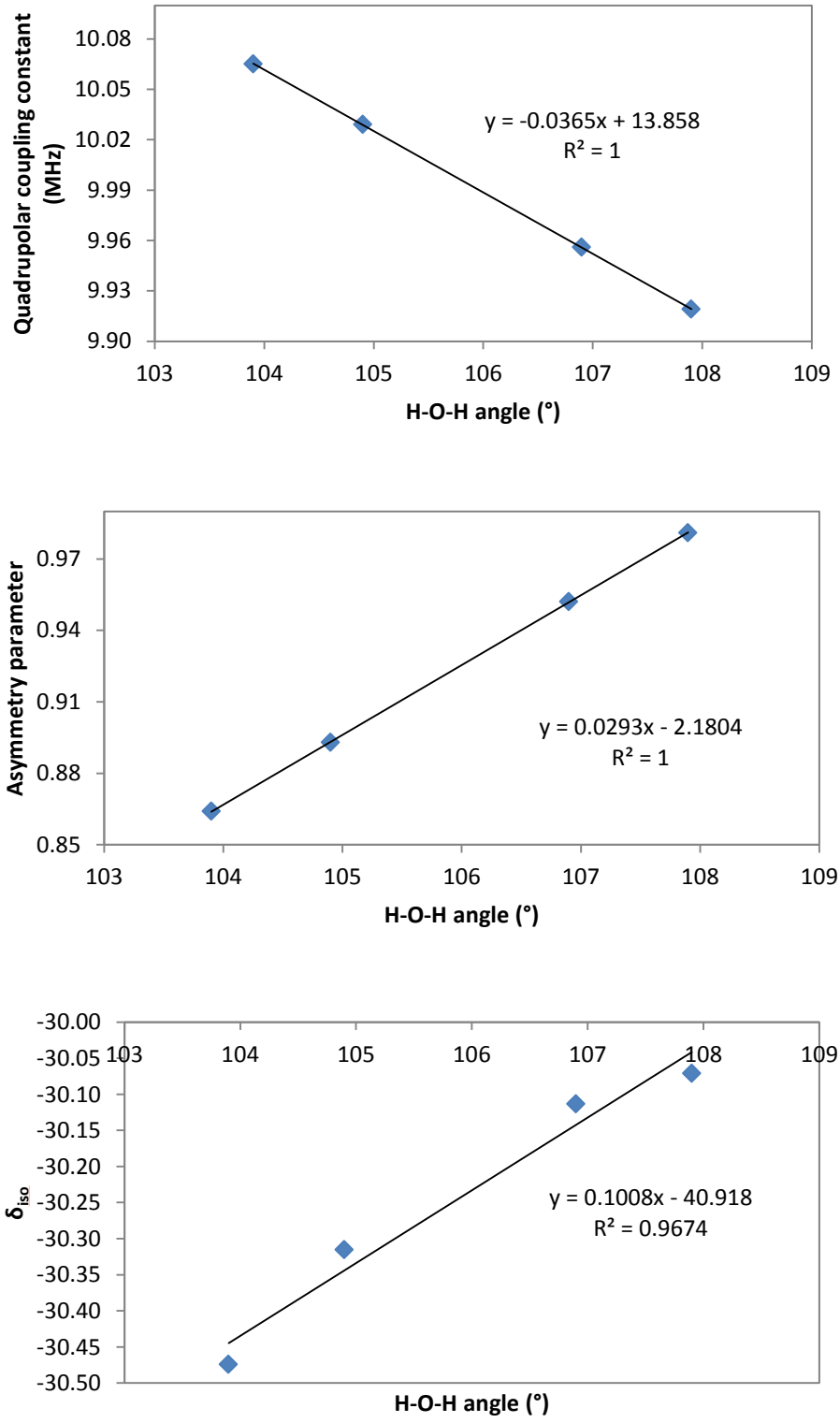

Figure 4.23: Computational results obtained using B3LYP/6-311+G (d,p) for the ^{17}O quadrupolar coupling constant, asymmetry parameter and isotropic chemical shift as a function of H-O-H angle for oxalic acid dihydrate.

Next, the hydrogen bond (O_w-H•••O) distance was varied from 1.77 Å to 2.17 Å to observe the changes in the parameters. As shown in **Figure 4.24**, the quadrupolar coupling constant increases from 9.6 MHz to 10.32 MHz with a slope of 1.64 MHz/Å, while the asymmetry parameter decreases from 0.99 to 0.89 with a slope of -0.266/Å and the isotropic chemical shift increase from 357.2 ppm to 361.0 ppm with a slope of 9.4 ppm/Å.

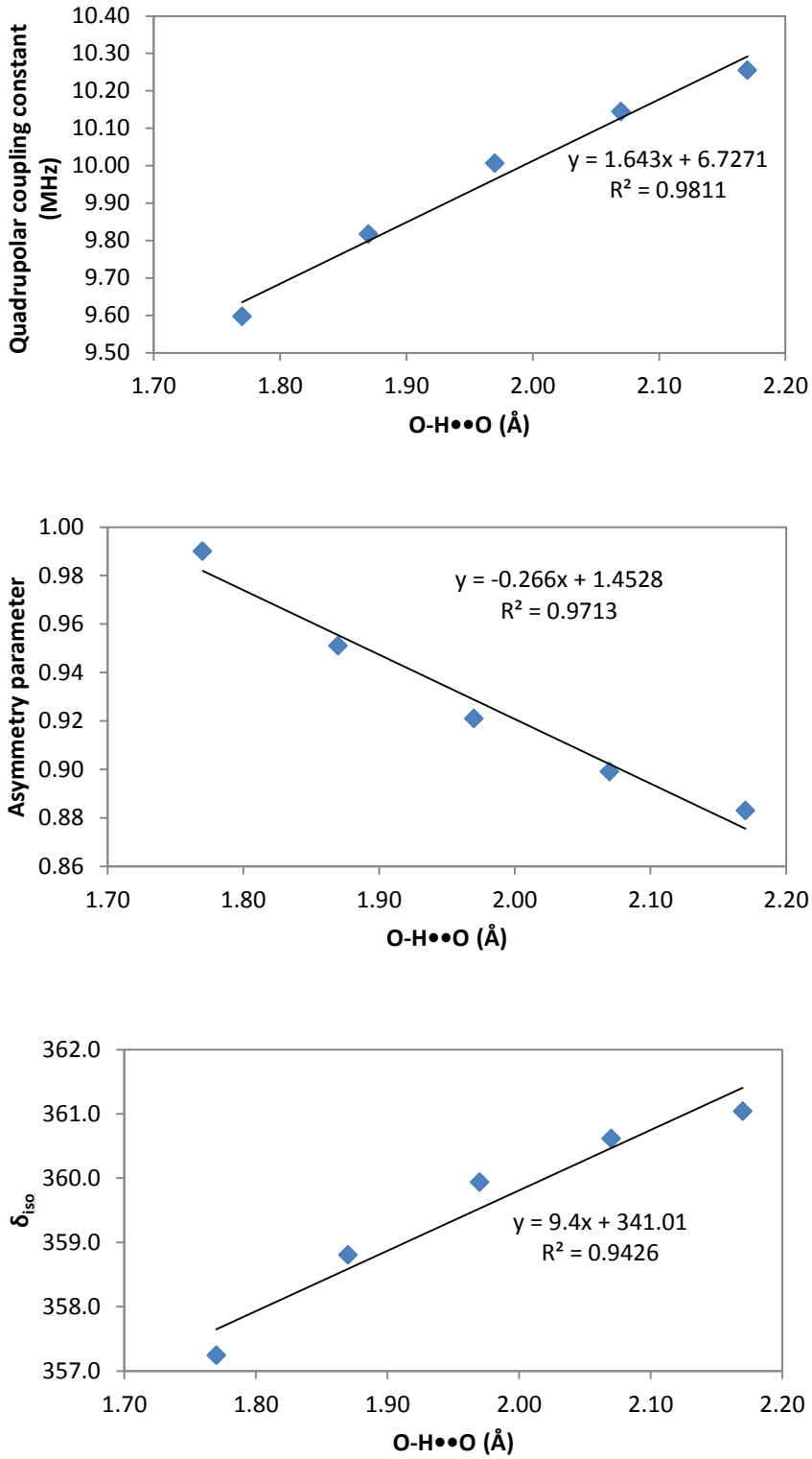

Figure 4.24: Computational results obtained using B3LYP/6-311+G(d,p) for the ^{17}O quadrupolar coupling constant, asymmetry parameter and isotropic chemical shift as a function of hydrogen bond distance for oxalic acid dihydrate.

Thirdly, the O-H distance was varied from 0.91 Å to 0.97 Å where, as shown in **Figure 4.25**, the quadrupolar coupling constant had an increasing trend from 9.7 MHz to 10.15 MHz while the asymmetry parameter decreases from 0.97 to 0.9. The isotropic chemical shift had an increasing trend where over the 0.915 Å to 0.975 Å, it increases from -37.5 ppm to -26 ppm.

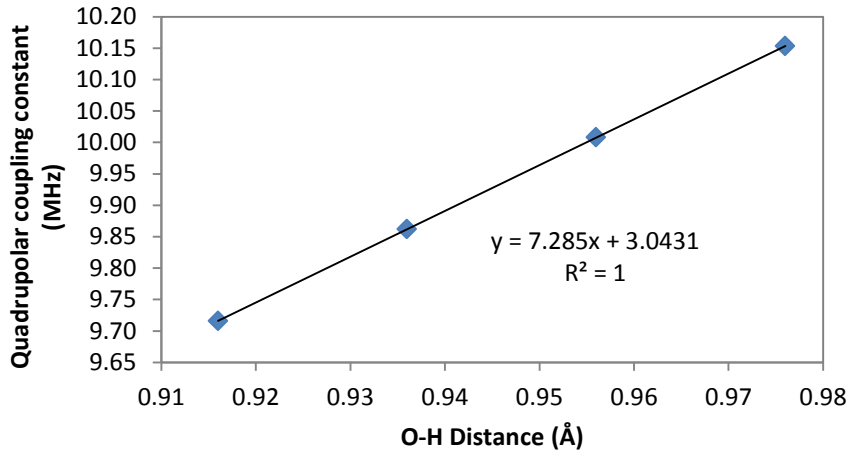

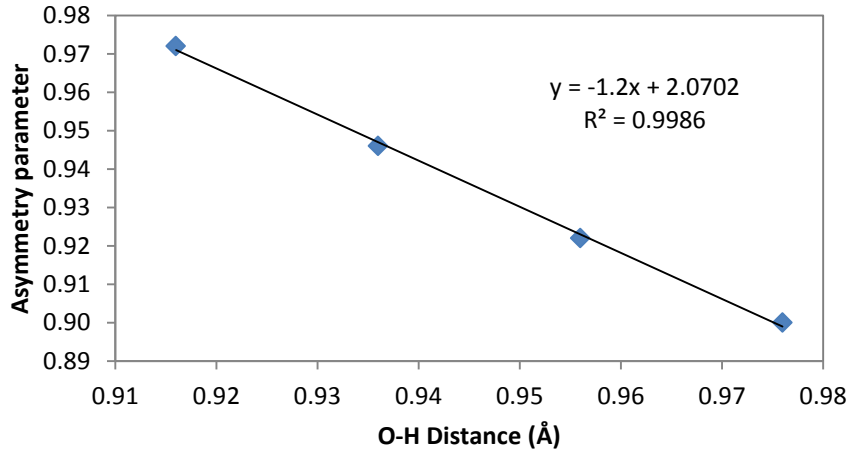

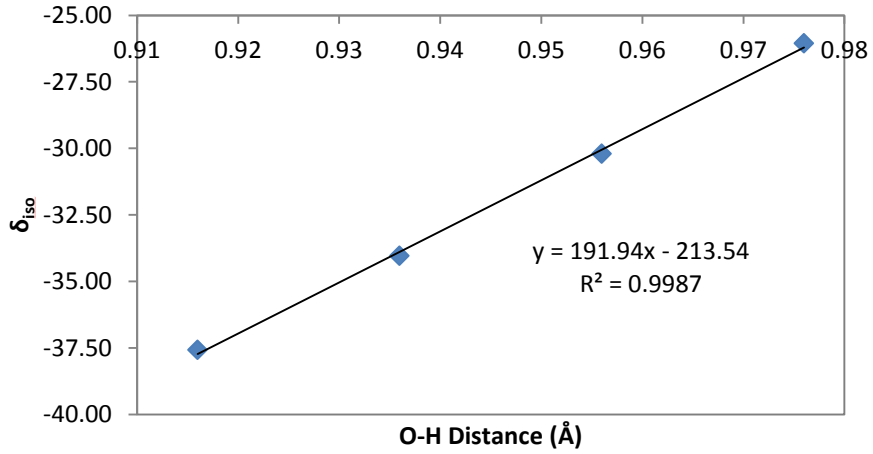

Figure 4.25: Computational results obtained using B3LYP/6-311+G(d,p) for the ^{17}O quadrupolar coupling constant, asymmetry parameter and isotropic chemical shift as a function of O-H distance for oxalic acid dihydrate.

According to the results above, it is worth noting that the change in the hydrogen bond distance had the most impact on the quadrupolar coupling constant while the H-O-H angle had the least impact. Also, the most noticeable impact on the asymmetry parameter and the isotropic chemical shift are due to the changes in the O-H distance while the least impact is due to the H-O-H angle.

The chemical shift tensor principal components (δ_{11}, δ_{22}, and δ_{33}) were also calculated as a function of the H-O-H angle, O_w-H•••O distance, and O-H distance. First, as shown in **Figure 4.26**, the value of δ_{11} (least shielded) had an increasing trend over a range of 5.5 ppm to 9.5 ppm as the H-O-H angle increases, with a slope of 0.96 ppm/°. The value of δ_{22} decreased over range of -24.7 ppm to -27.2 ppm with a slope of -0.66 ppm/° and δ_{33} increased over a range of -72.37 ppm to 72.36 ppm with a slope of 0.002 ppm/°.

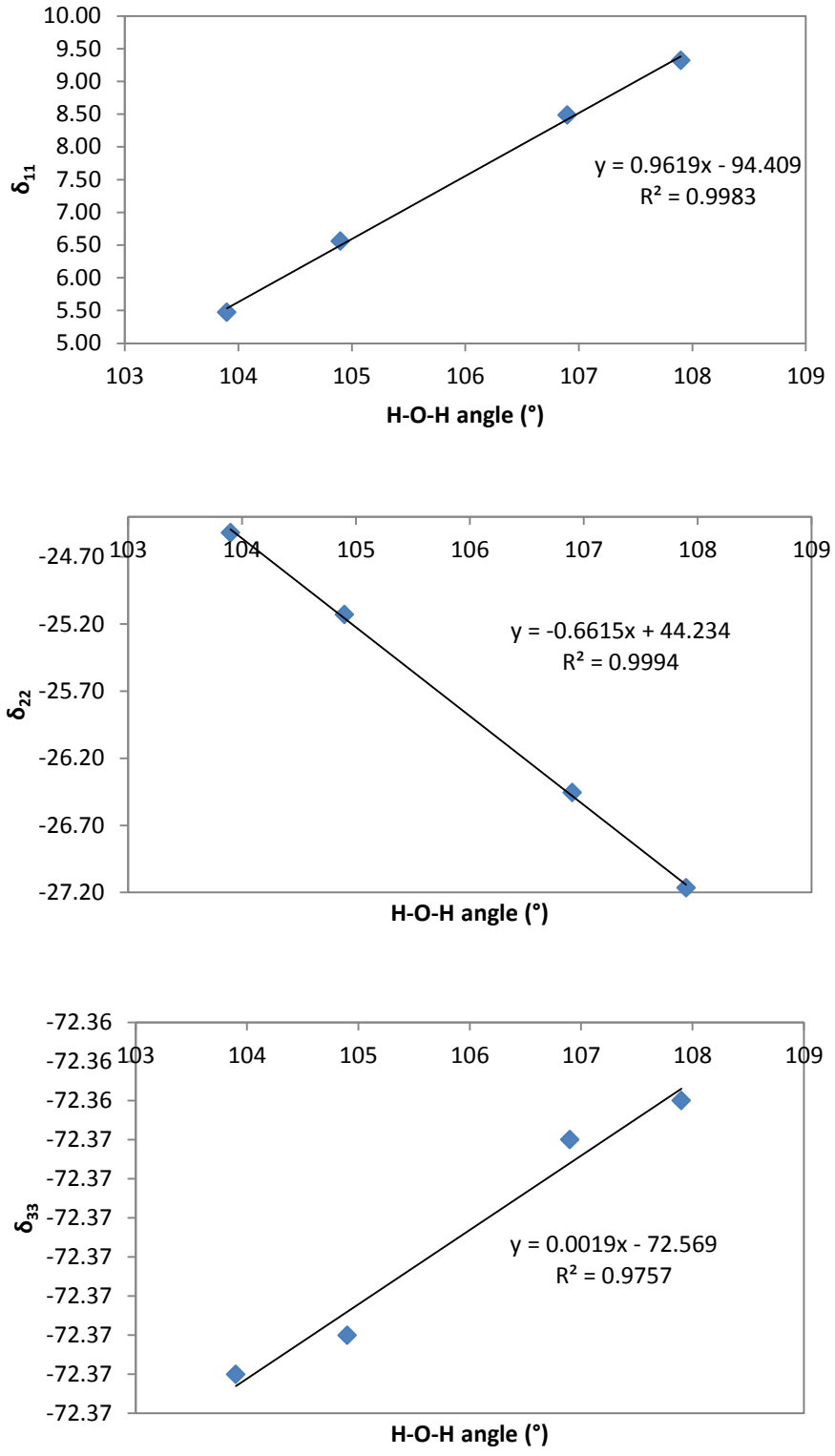

Figure 4.26: Computational results obtained using B3LYP/6-311+G (d,p) for the ^{17}O chemical shift principal components as a function of H-O-H angle for oxalic acid dihydrate.

Second, shown in **Figure 4.27**, the chemical shift tensors were calculated as a function of the hydrogen bond distance to determine its impact. All CS tensor components had an increasing pattern as a function of increasing hydrogen bond distances. The value of δ_{11} increased from 270 ppm to 286 ppm with a slope of 39 ppm/Å, the value of δ_{22} increased from of 310.5 ppm to 315 ppm with slope of 10 ppm/Å, and δ_{33} increased from 357 ppm to 361 ppm with slope of 9.4 ppm/Å.

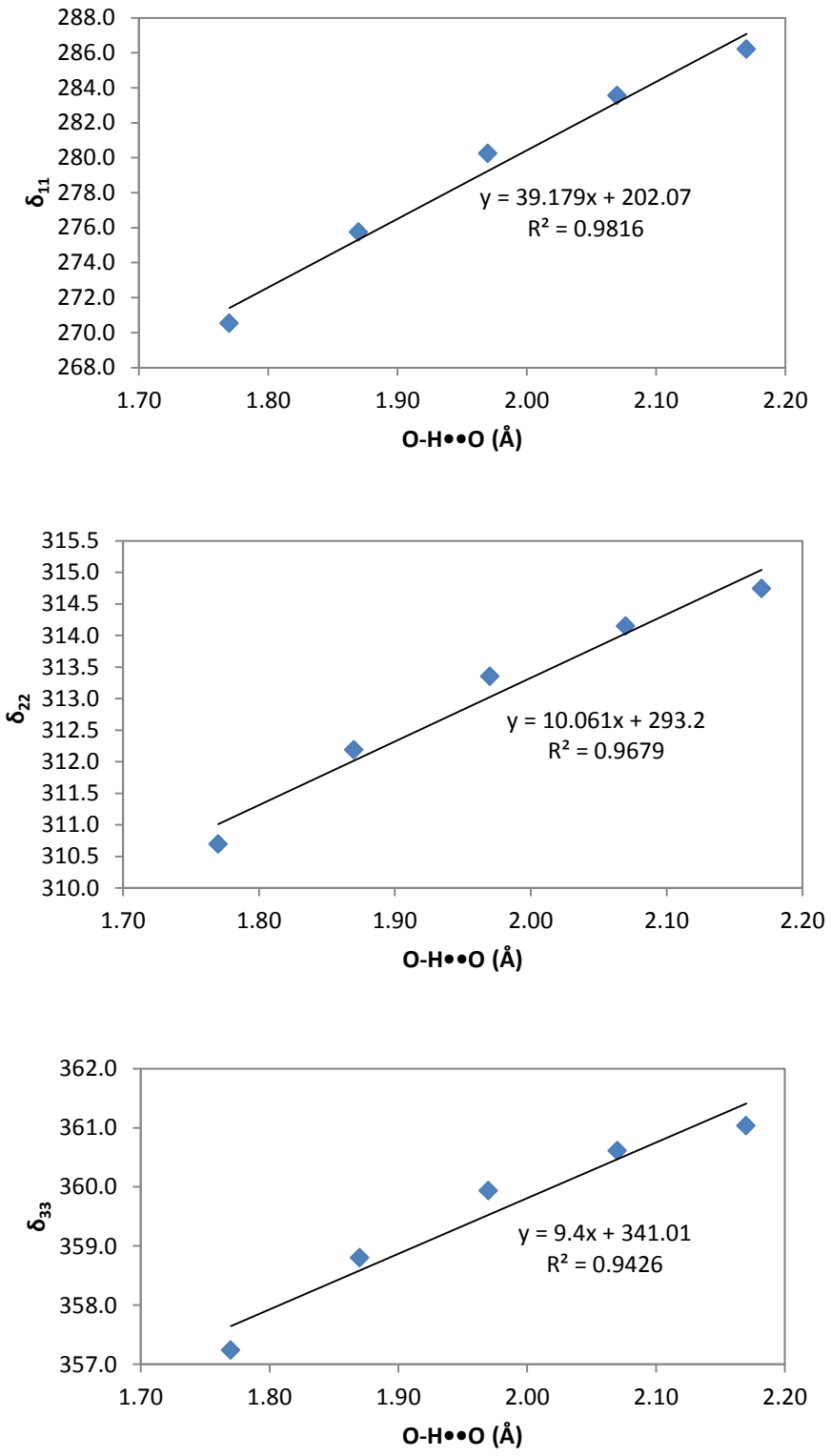

Figure 4.27: Computational results obtained using B3LYP/6-311+G (d,p) for the ^{17}O chemical shift principal components as a function of hydrogen bond distance for oxalic acid dihydrate.

Thirdly, the chemical shift tensors are calculated as a function of O-H distance, as shown in **Figure 4.28** below. Again all three chemical shift components have an increasing trend as a function of increasing O-H distance. δ_{11} increased over a range of 0 ppm to 12 ppm with slope 195.6 ppm/Å, while δ_{22} increased over the range of -34.0 ppm to -22.0 ppm with slope of 207 ppm/Å and δ_{33} increased over the range of -79.0 ppm to -69.0 ppm with slope of 172 ppm/Å.

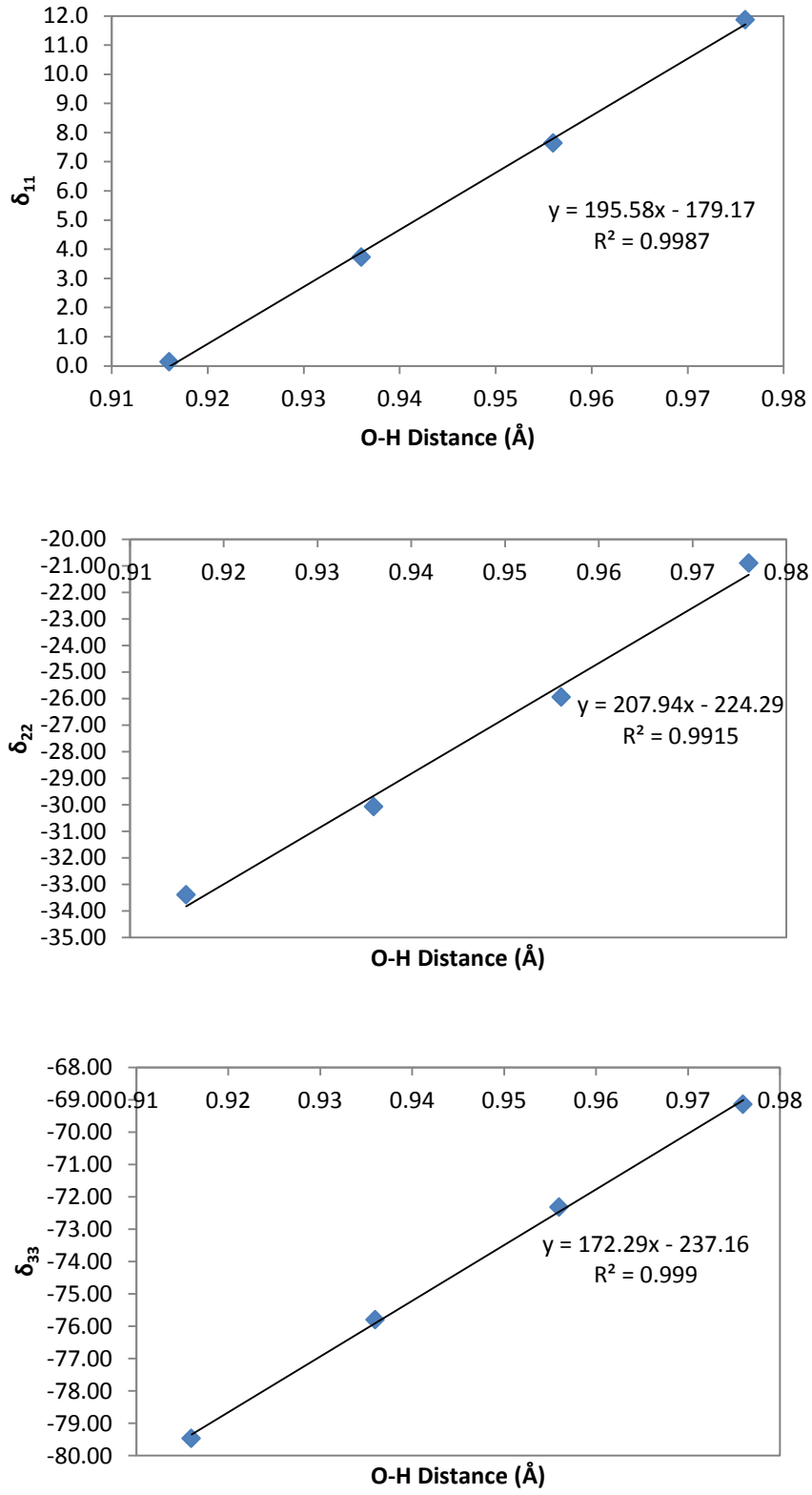

Figure 4.28: Computational results obtained using B3LYP/6-311+G (d,p) for the ^{17}O chemical shift principal components as a function of O-H distance for oxalic acid dihydrate.

It is evident that the CS tensor components generally increased with each of the tested geometrical parameters. It is worth noting that the increase of the O-H distance had the most impact on all three chemical shift tensor components while the change in the H-O-H angle had the least impact of all. This is somewhat similar for the parameters C_Q, η, and δ_{iso}.

4.4.3 The effect of the distance between a metal and water molecule on NMR parameters

Next, using the same method and basis set (B3LYP/6-311+G(d, p)), an isolated molecular system was built where a free metal cation (Ba, Na, Li, and K) is distanced from a water molecule to determine how the distance between a metal and water molecule can affect the NMR parameters. In the computational results section, NMR parameters including C_Q, η, Ω, δ_{11}, δ_{22}, and δ_{33} are all plotted against the hydrogen bond distance. The results will be shown for each metal-water system, where the distance range for each result takes in perspective the actual distance between the metal and water in available crystal structures.

Ba•••OH_2

As shown in **Figure 4.29** C_Q, η, and Ω are plotted against the Ba-O distance which varies between 2.68 Å to 2.83 Å. The value of C_Q is observed to increase from -12.55 MHz to -12.10 MHz with slope of 2.88 MHz/Å. The η also shows an increasing trend ranging from 0.86 to 0.95 with slope of 0.52/Å while the Ω decreases from 436 ppm to 390 ppm with a slope of -310.6 ppm/Å.

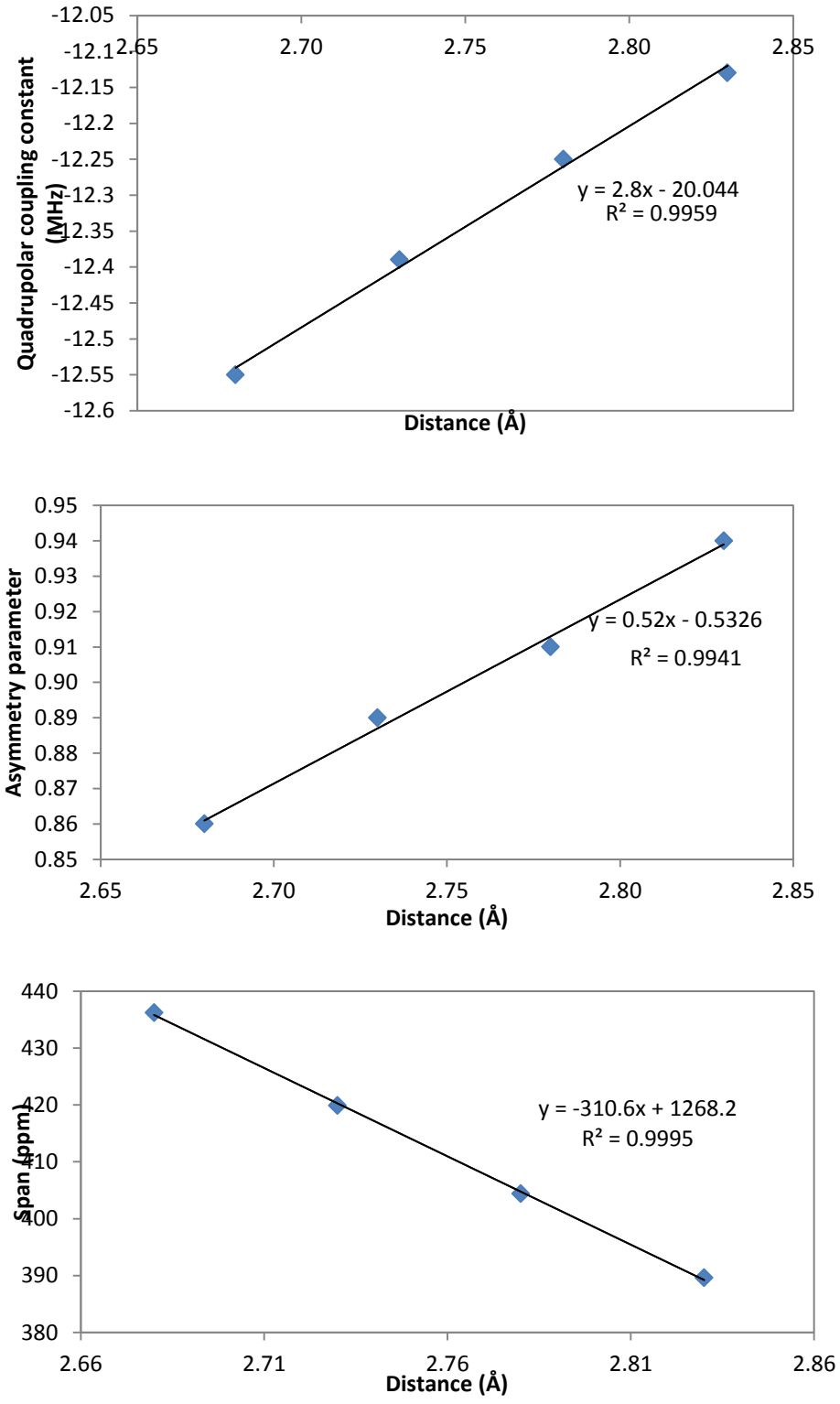

Figure 4.29: Computational results obtained using B3LYP/6-311+G(d,p) for C_Q, η, and Ω as a function of the Ba-O_w distance.

The chemical shift tensor components are plotted next as a function of metal-water distance where all three had a decreasing trend. The value of δ_{11} (least shielded) decreased from 422 ppm to 372 ppm with a slope of -324.4 ppm/Å, δ_{22} decreased over the range of 198 ppm to 177 ppm with a slope of -139.2ppm/Å and δ_{33} (most shielded) decreased over the range from -14 ppm to -15.6 ppm with a slope of -9.8 ppm/Å. It is clear that the change in the distance had the most impact on δ_{11} and least impact on δ_{33}. The results are shown below in **Figure 4.30**.

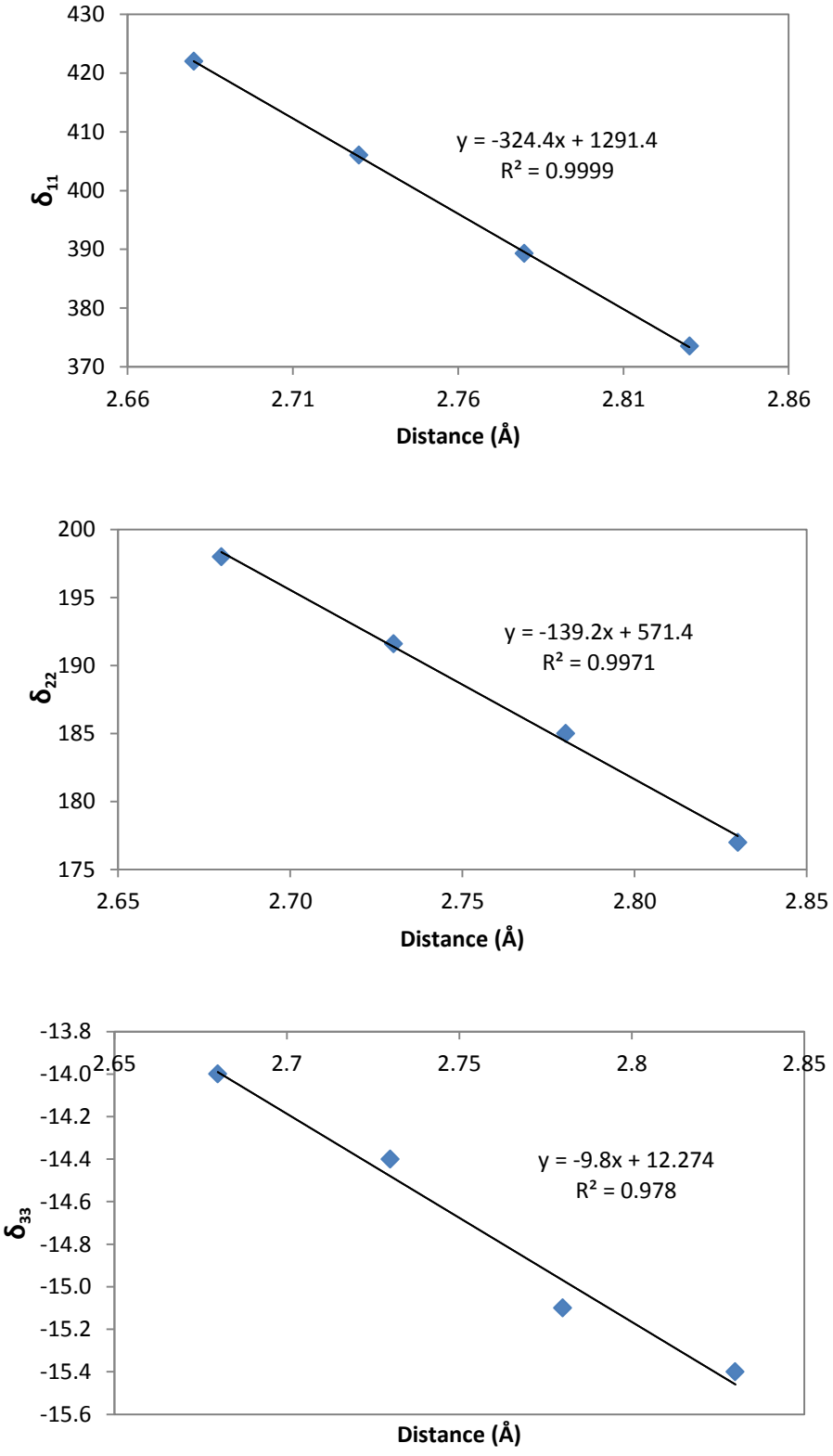

Figure 4.30: Computational results obtained using B3LYP/6-311+G(d,p) for $\delta_{11,}$ $\delta_{22,}$ and δ_{33} as a function of Ba-O_w distance.

Na•••OH_2

As shown in **Figure 4.31**, the C_Q, η, and Ω are plotted against the Na-O distance which varies between 2.32 Å to 2.52 Å. The C_Q is observed to increase from 11.22 MHz to 11.29 MHz with slope of 0.37 MHz/Å. The η shows a decreasing trend ranging from 0.989 to 0.940 with slope of -0.23/Å while the Ω decreases from 165 ppm to 162 ppm with a slope of -63.4 ppm/Å.

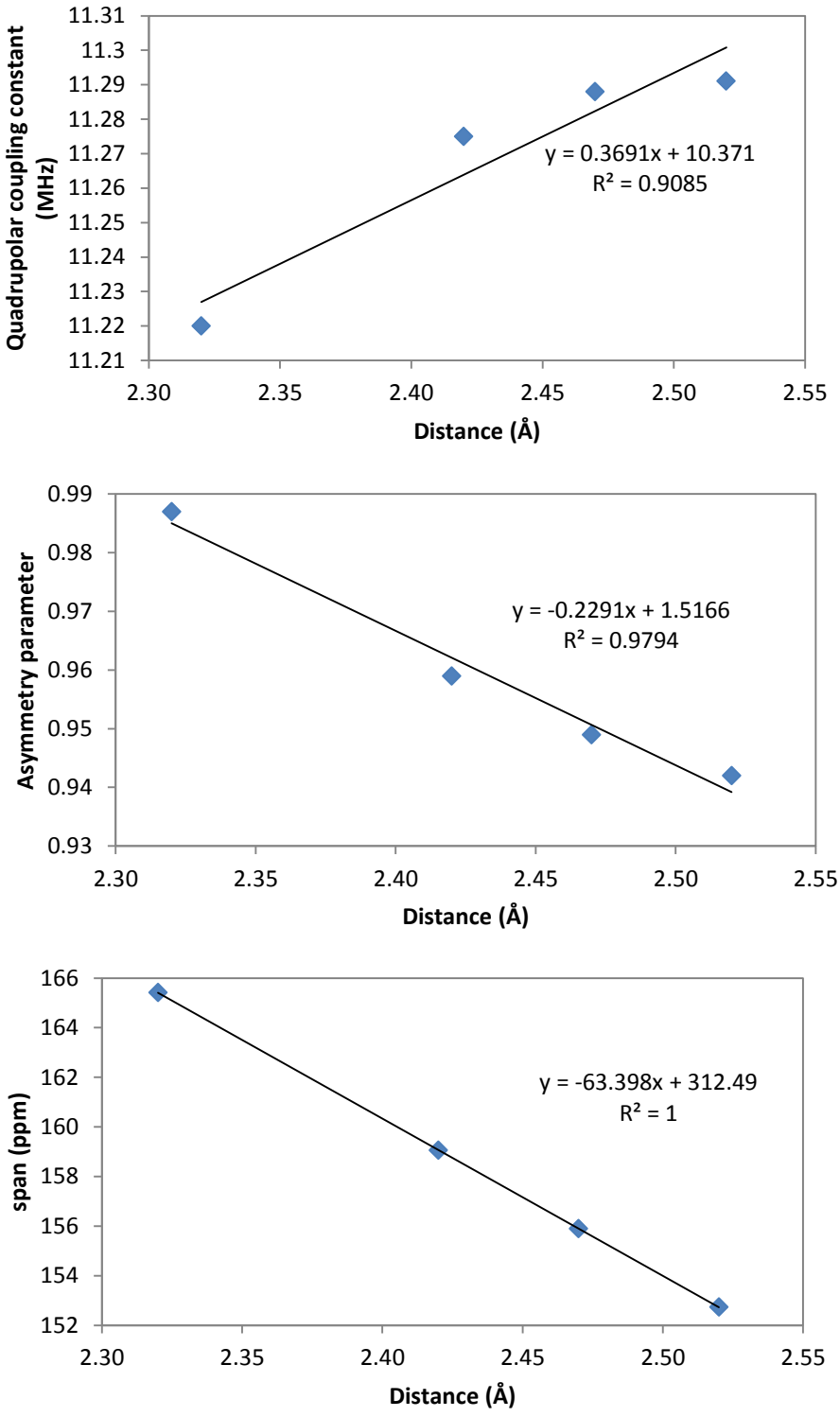

Figure 4.31: Computational results obtained using B3LYP/6-311+G(d,p) for C_Q, η, and Ω as a function of Na-O_w distance.

As shown in **Figure 4.32**, the chemical shift tensor components are plotted next as a function of metal-water distance which all had a decreasing trend. δ_{11} decreased over the range from 123 ppm to 109 ppm with a slope of -71.6 ppm/Å, δ_{22} decreased over the range of 28.6 ppm to 26 ppm with a slope of -12.8 ppm/Å and δ_{33} (most shielded) decreased over range from -14 ppm to -15.4 ppm with a slope of -8.3 ppm/Å. Unlike the case of the barium-water complex, all chemical shift tensor components were not affected that much by the change of sodium-water distance with a very similar change for δ_{33} observed for both systems.

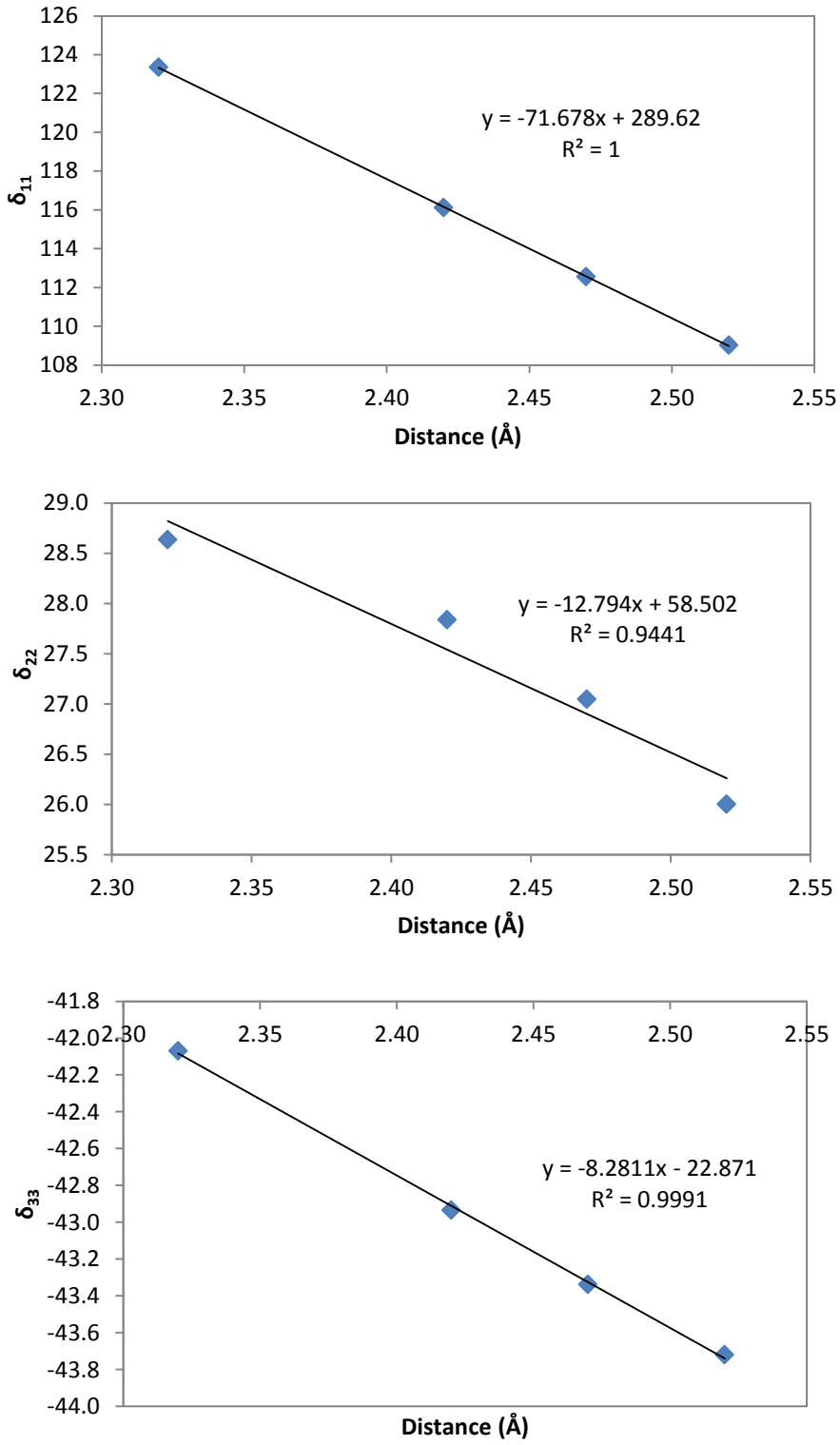

Figure 4.32: Computational results obtained using B3LYP/6-311+G(d,p) for $\delta_{11,}$ $\delta_{22,}$ and δ_{33} as a function of Na-O_w distance.

K•••OH_2

As shown in **Figure 4.33**, the C_Q, η, and Ω are plotted against the K-O distance which varies between 2.81 Å to 3.01 Å. The C_Q is observed to increase from 11.720 MHz to 11.785 MHz with slope of 0.316 MHz/Å. The η shows a decreasing trend ranging from 0.93 to 0.90 with slope of -0.15/Å while the Ω decreases from 163 ppm to 153 ppm with a slope of -53.0 ppm/Å.

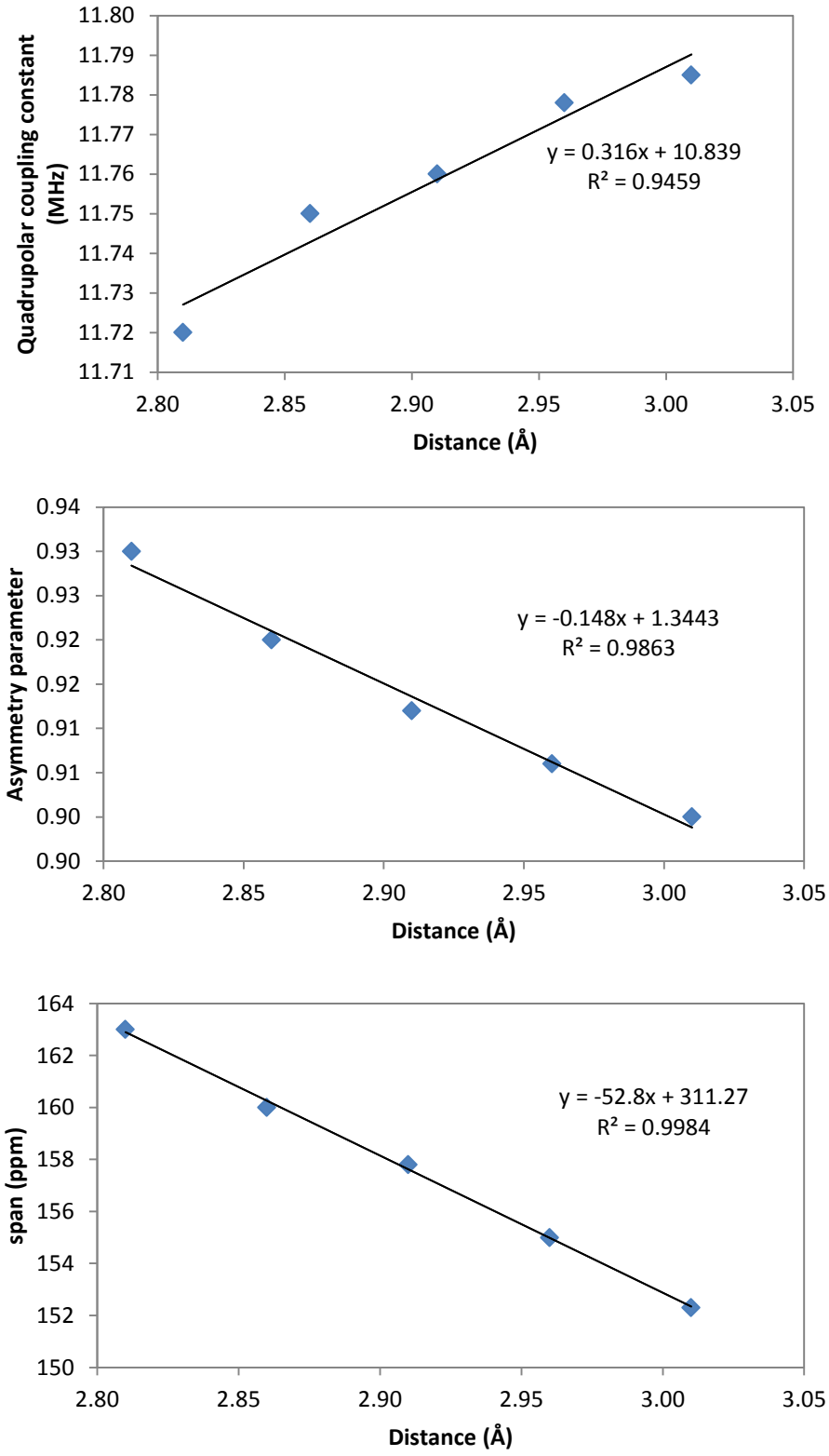

Figure 4.33: Computational results obtained using B3LYP/6-311+G(d,p) for C_Q, η, and Ω as a function of Na-O_w distance.

As shown in **Figure 4.34**, the chemical shift tensor components are plotted as a function of metal-water distance which all had a decreasing trend. The value of δ_{11} decreased over range from 125 ppm to 117 ppm with a slope of -55.1 ppm/Å, δ_{22} decreased over range of 54 ppm to 46 ppm with a slope of -39.4 ppm/Å and δ_{33} decreased over range from -42.0 ppm to -42.40 ppm with a slope of -1.6 ppm/Å. Again, unlike the case with the barium-water complex, all CS components were not affected that much by the change of potassium-water distance. The impact here is even less than in the sodium-water complex. It is also worth noting that almost no change happened in δ_{33} as a function of the distance.

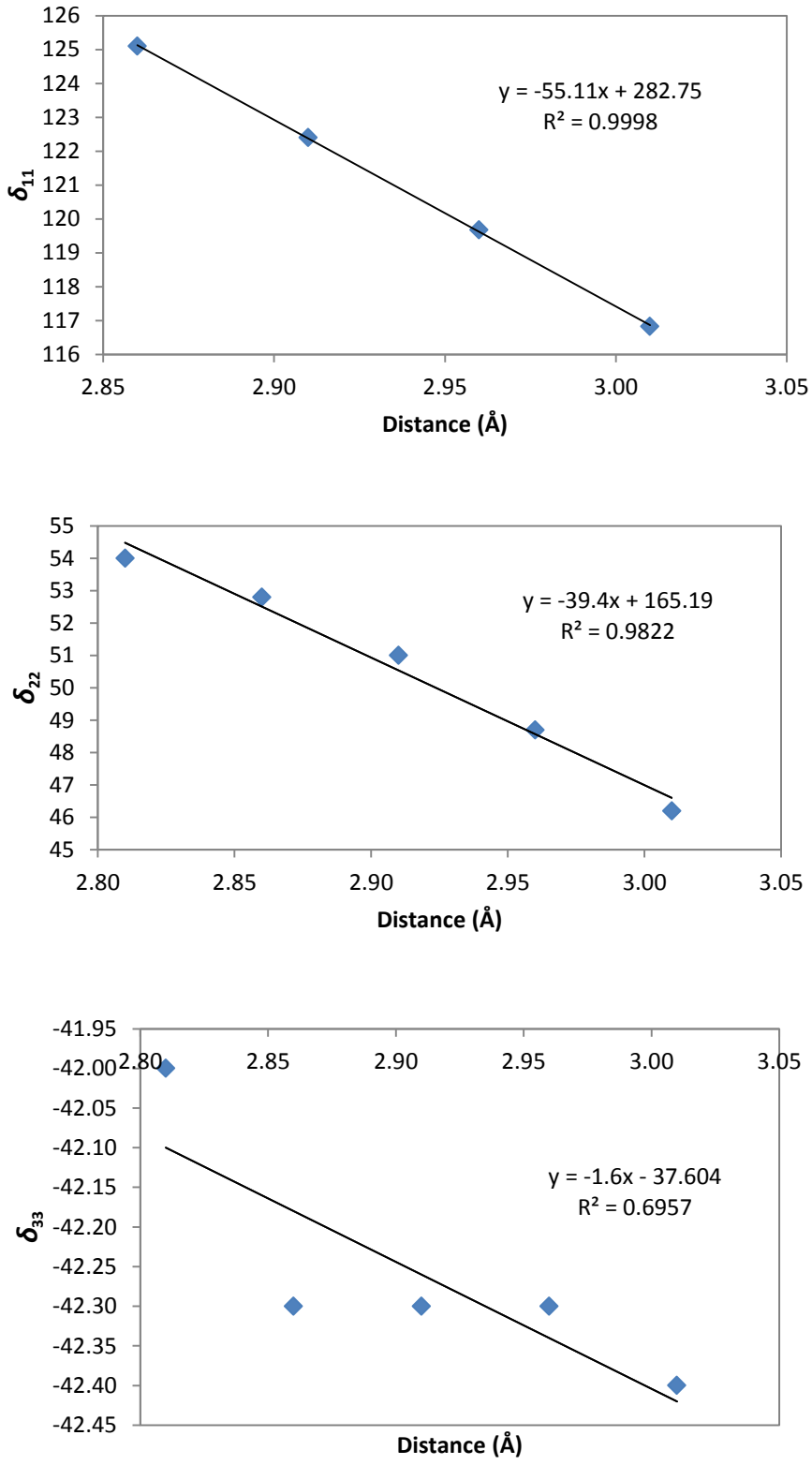

Figure 4.34: Computational results obtained using B3LYP/6-311+G(d,p) for $\delta_{11,}$ $\delta_{22,}$ and δ_{33} as a function of K-O_w distance.

Li•••OH_2

As shown in **Figure 4.35**, the C_Q, η, and Ω are plotted against the Li-O distance which varies between 1.91 Å to 2.06 Å. The C_Q value is observed to increase from 11.80 MHz to 11.96 MHz with slope of 1.02 MHz/Å. The η shows a decreasing trend ranging from 0.98 to 0.90 with slope of -0.386/Å while the Ω decreases from 258 ppm to 242 ppm with a slope of -108.6 ppm/Å.

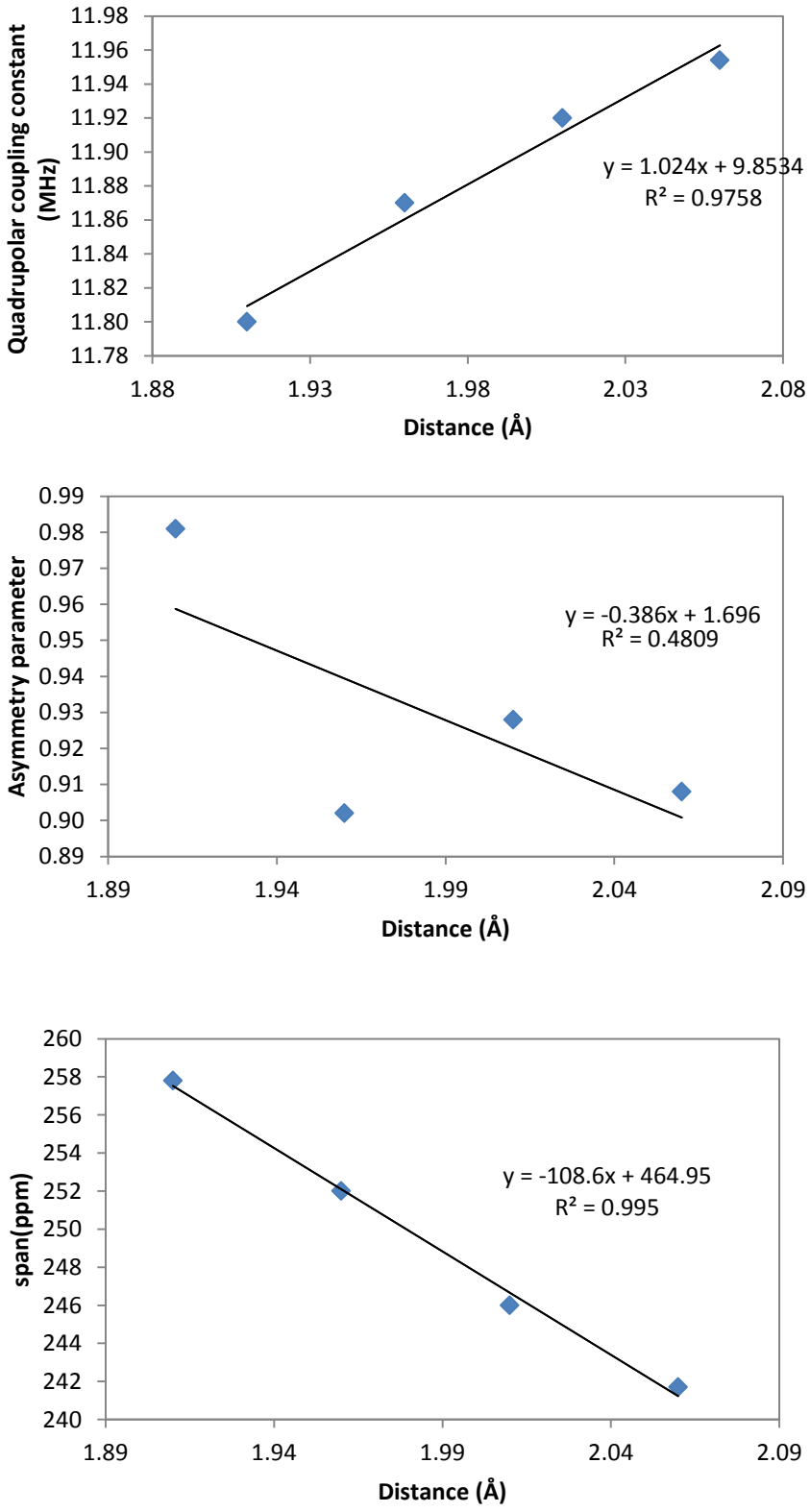

Figure 4.35: Computational results obtained using B3LYP/6-311+G(d,p) for C_Q, η, and Ω as a function of Li-O_w distance.

As shown in **Figure 4.36**, the chemical shift tensor components are plotted next as a function of metal-water distance where δ_{11} and δ_{33} had a decreasing trend but δ_{22} has a surprisingly an increasing trend. δ_{11} decreased over range from 224 ppm to 207 ppm with a slope of -112 ppm/Å, δ_{22} increased over the range of 116 ppm to 119 ppm with a slope of 19.4 ppm/Å and δ_{33} decreased over the range from -33.5 ppm to -34.1 ppm with a slope of -4.2 ppm/Å.

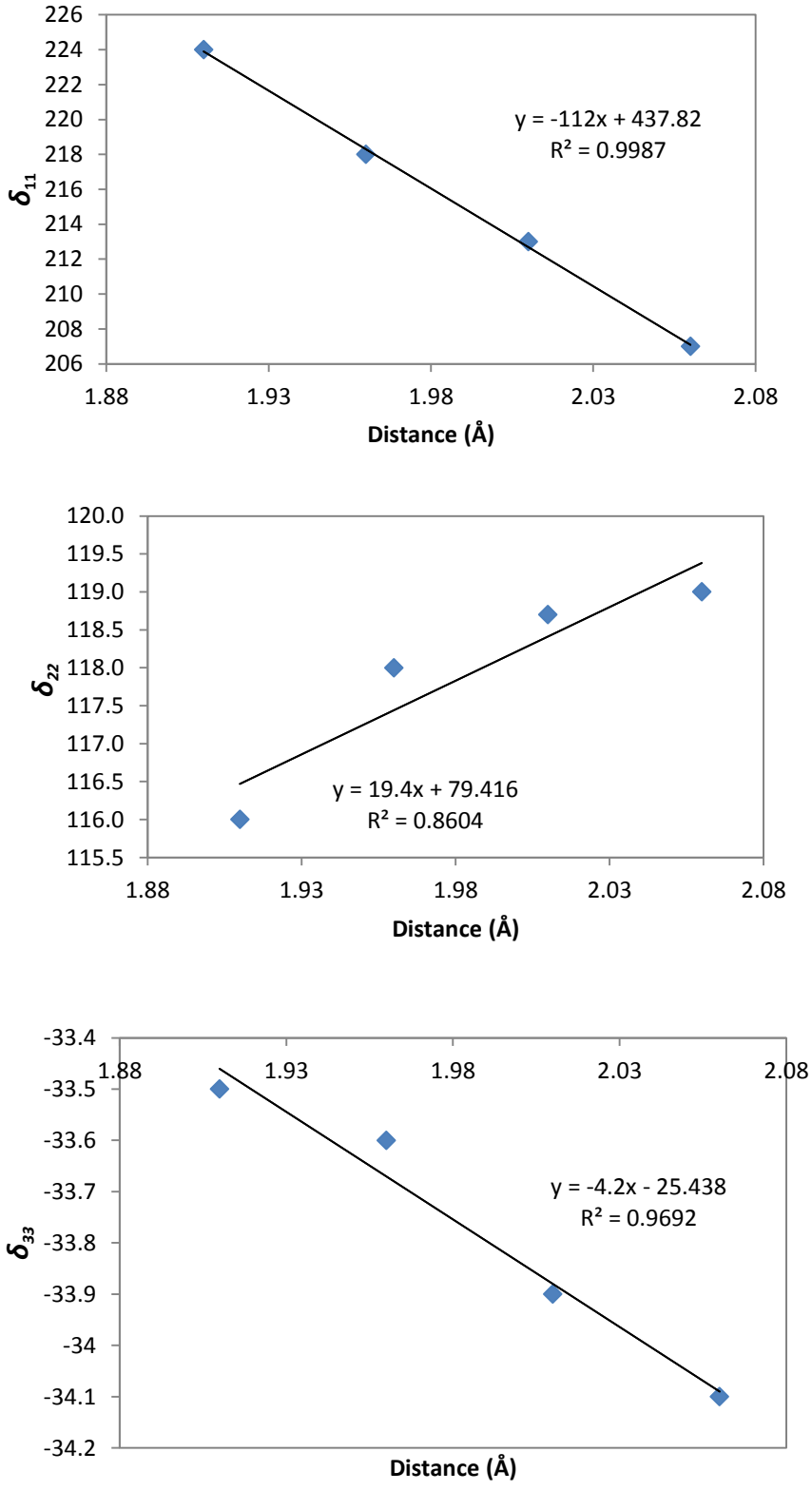

Figure 4.36: Computational results obtained using B3LYP/6-311+G(d,p) for $\delta_{11,}$ $\delta_{22,}$ and δ_{33} as a function of Li-O_w distance.

4.5 Discussion of computational and experimental results

In this section, the computational results representing the change in hydrogen bond geometry and its impact on the NMR parameters for both the organic molecular model, oxalic acid hydrate, and the inorganic molecular model, barium chlorate hydrate, will be discussed in search for a correlation with experimental results which are summarized in **Table 4.1**. The changes of geometry investigated included the hydrogen bond distance, O-H distance, and H-O-H angle. Second, the computational results for the change in metal-water distance will also be discussed. It is clear that the factors contributing to the experimental results are simply too many and overlapping, as shown in **Table 4.1**, suggesting that we can only study the effect of each structural change on a specific parameter to determine which has most effect. In the sections to follow and after discussing all computational results the most factors which contribute to NMR parameters will be specified.

4.5.1 Discussion of computational results

First, barium chlorate hydrate is used as molecular model for the inorganic hydrates studied in this work. The chemical shift tensor components $\delta_{11,}$ $\delta_{22,}$ and δ_{33} were studied for each of the geometrical changes where all three chemical shift tensor components had a decreasing pattern as the H-O-H angle increased, while the O-H distance increase caused δ_{11} and δ_{22} to increase and caused δ_{33} to decrease. Lastly, as the hydrogen bond distance increased, the value of δ_{11} decreased while the other two chemical shift tensor components had an increasing pattern.

The structural change with most impact on the δ_{11} is hydrogen bond distance; whereas the hydrogen bond distance increased the first chemical shift tensor had a decreasing pattern with slope of -10471 ppm/Å. Perhaps it is also worth mentioning that the H-O-H

angle had a very minimal impact on the first chemical shift tensor component. The δ_{22} value was mostly affected by the change in the hydrogen bond distance, where an increasing hydrogen bond distance leads to an increasing trend for δ_{22} with a slope 3718 ppm/Å. It is clear that also the change in hydrogen bond distance largely impacted the δ_{33}, whereas the hydrogen bond distance increased, the value of δ_{33} increased with a slope of 29303 ppm/Å. Again, we report that the H-O-H angle had a minimal impact on the three chemical shift tensor components. We conclude that the hydrogen bond distance in barium chlorate hydrate impacted the oxygen chemical shift tensor most.

It is therefore not surprising that the value of δ_{iso} is most affected by the change in the hydrogen bond distance where the H-O-H angle had no impact, while the increasing trend in the O-H distance caused the isotropic chemical shift to have a decreasing trend with slope of -1299 ppm/Å and finally the increasing hydrogen bond distance caused an increasing trend for isotropic chemical shift with slope 4680 ppm/Å. It is worth noting then that the increasing O-H distance and hydrogen bond distance lead to an opposite effect on the isotropic chemical shift with a greater impact to the hydrogen bond distance.

The quadrupolar coupling constant and asymmetry parameter like the isotropic chemical shift were not affected by the change in H-O-H angle as much as the other two structural changes. It is clear that the increase in O-H distance had the most impact on the quadrupolar coupling constant with an increasing slope of 2.3 MHz/Å. Also, the increase in the hydrogen bond the quadrupolar coupling constant had an increasing slope of 1.01 MHz/Å. Secondly, the asymmetry parameter was also most affected by the change in the O-H distance whereas the O-H distance increased the asymmetry parameter decreased with slope of -0.3/Å. Again, as the hydrogen bond distance increased the asymmetry parameter

had a decreasing slope of -0.09/Å. This concludes that whether the O-H or hydrogen bond distance increased, the quadrupolar coupling constant and asymmetry parameter will increase and decrease respectively.

Second, the computational results for oxalic acid hydrate will be investigated. It is worth to note first that again the H-O-H angle had the least impact on all parameters to be discussed. The value of δ_{11} is most sensitive to the O-H distance whereas the O-H distance increased, the δ_{11} had an increasing slope of 195 ppm/Å. The hydrogen bond distance also affected the δ_{11} in the same increasing direction as the O-H distance with a slope of 39 ppm/Å. The second chemical shift tensor component, δ_{22}, also increased, as O-H distance increased, with slope of 207 ppm/Å. Therefore, δ_{22} is also most sensitive to O-H distance while a minimal impact is observed for both changes in the hydrogen bond distance and the H-O-H angle. The δ_{33} just like the δ_{22} is most sensitive to the O-H distance and was not impacted by changes in the hydrogen bond distance or H-O-H angle. We can conclude that the chemical shift tensor is most sensitive to the O-H distance in oxalic acid hydrate.

It is not surprising that the isotropic chemical shift is most affected by the O-H distance. The quadrupolar coupling constant and asymmetry parameter are also most sensitive to the O-H distance whereas the O-H distance increases, the quadrupolar coupling constant will have an increasing trend with slope of 7.285 MHz/Å and as the hydrogen bond distance increases, quadrupolar coupling constant will increase with slope of 1.64 MHz/Å. Nonetheless, the increase in O-H bond and hydrogen bond distance with decrease the asymmetry parameters will decrease with slopes of -1.2/Å and -0.26/Å respectively. This concludes that as the O-H and hydrogen bond distances increase the quadrupolar coupling constant and asymmetry parameter will increase and decrease, respectively.

It is clear that the parameters including the C_Q, η, δ_{iso}, $\delta_{11,}$ $\delta_{22,}$ and δ_{33} are most sensitive to the hydrogen bond distance in barium chlorate hydrate and to the O-H distance in oxalic acid hydrate. The quadrupolar coupling constant increases and asymmetry parameter decreases to increasing hydrogen bond and O-H bond distances on both molecular models.

In molecular models constructed of a free metal and water molecule with varying distances, the computational results will be discussed and since each of the inorganic hydrates studied in this work contain a different cation, the effect of each cation and its distance from the water will play a role in the impact it has on the NMR parameters. Here, we study how that change in distance will affect quadrupolar coupling constant, asymmetry parameter, span, and chemical shift tensors accordingly. First, the increase in Ba-O_w shows an increase in quadrupolar coupling constant and asymmetry parameter. In comparison to the other metals, this model shows a largest impact on the span whereas Ba-O_w increases, the span has a decreasing slope of -310.6 ppm/Å while the second largest decrease in span is in Li-O_w of a decreasing slope of -108.6 ppm/Å. The impact the Ba-O_w has on quadrupolar coupling constant and asymmetry parameter is largest with slopes 2.8 MHz/Å and 0.52/Å. It is also worth noting that in all M-O_w, as the distance increase the asymmetry parameter will decrease except for Ba-O_w. As the M-O_w increases, the quadrupolar coupling constants increase with slopes of 2.8, 1.02, 0.37 and 0.32 MHz/Å for Ba-O_w, Li-O_w, Na-O_w and K-O_w respectively. Also as the M-O_w increases, the asymmetry parameters increase with slopes of 0.52, -0.39, -0.23 and -0.148/Å for Ba-O_w, Li-O_w, Na-O_w and K-O_w respectively. Note how the impact on the parameters decreases as the cation size decreases as we go from Ba to K.

It is not surprising to observe the same trend for the chemical shift tensors. The first chemical shift tensor component δ_{11} is the most sensitive to the change in Ba-O_w distance in

comparison to the other CS components. The same case is for Li-O_w and K-O_w while the second chemical shift tensor is most sensitive in the Na-O_w distance changes. As the M-O_w increases, δ_{11} decreases in all metal systems with slopes of -324, -112, -72, -55 ppm/Å for Ba-O_w, Li-O_w, Na-O_w and K-O_w respectively. Also the value of δ_{22} was not sensitive in Li-O_w and K-O_w while it had a decreasing pattern in most part. Finally, there is no impact on δ_{33} as the metal-water distance changes, making it the least sensitive.

We can therefore conclude that quadrupolar coupling constant and asymmetry parameter become less affected as the metal size decreases. Second, the asymmetry parameter decreases as a function of metal-water distance increase except for the Ba-O_w. The span shows a decreasing trend as the M-O_w distance increases and again is most impacted in large cation systems versus smaller cations. The chemical shift tensor components are most impacted by the change in the M-O_w distance in order of $\delta_{11} > \delta_{22} > \delta_{33}$ where there is pretty much no difference in the third chemical shift tensor component.

4.5.2 Discussion of experimental results

We first must note that there is no clear correlation between the experimental results for all NMR parameters shown in Figure 4.1 and the structural difference in each of the inorganic hydrates, yet we can discuss the experimental parameters in the scope of which factor contributes most to each parameter. The computational results clearly show that we cannot place the oxalic acid hydrate in the same basket as the other hydrates since it is an organic molecule while the other hydrates are inorganic molecules. Since oxalic acid hydrate is the only organic hydrate molecule studied here, it will be not possible to compare it to the other inorganic hydrates. However, we can conclude that the O-H distance is what most impacts the NMR parameters in organic hydrate molecules.

First, the quadrupolar coupling constant and the asymmetry parameter experimental results will be discussed for each molecule. As mentioned before, the hydrogen bond distance stood out to be the structural change with most impact on both of these parameters. It is clear to note that $NaClO_4 \bullet H_2O$ with longest hydrogen bond distance out of all inorganic hydrates (2.152 Å) had the largest quadrupolar coupling constant of 7.39 MHz while the $K_2C_2O_4 \bullet H_2O$ with the shortest hydrogen bond distance (1.80 Å) had the smallest quadrupolar coupling constant of 6.75 MHz. The asymmetry parameter clearly could have not been correlated with any of the structural changes which imply there are too many factors contributing to its results. However, one factor stands out which is the M-O_w distance. Overall, the larger the M-O_w and O-H distance the lower asymmetry parameter the molecule will have with the exception to barium chlorate hydrate.

Second, the chemical shift tensors will be discussed for the inorganic hydrates along with hydrogen bond distance and the metal-water distance since these two structural characteristics contribute the most to the NMR parameters, according to the computational results. First, we can observe from for the chemical shift tensors in all hydrates that the difference in each tensor component decreases in the order $\delta_{11} > \delta_{22} > \delta_{33}$. For instance, δ_{11} for the four inorganic hydrates ranges from -5.78 ppm to 36.7 ppm while δ_{22} is in the range of -6.45 ppm to 15.5 ppm and δ_{33} had similar values for $NaClO_4 \bullet H_2O$, $LiSO_4 \bullet H_2O$ and $K_2C_2O_4 \bullet H_2O$ (~33 ppm) while $Ba(ClO)_3 \bullet H_2O$ had different value of 6.65 ppm. This observation is close to the computational results obtained for M-O_w distances. Second, the O-H distance for each of the inorganic hydrates does not relate at all to the chemical shift tensors. We conclude that there is an overall correlation between the M-O_w distance and the impact it has most on δ_{11} and least on δ_{33}. It is also clear that the chemical shift tensor values

for $NaClO_4 \cdot H_2O$, $LiSO_4 \cdot H_2O$ and $K_2C_2O_4 \cdot H_2O$ are closer to each other in comparison to the $Ba(ClO)_3 \cdot H_2O$.

Even though the computational results showed that the H-O-H angle did not impact the parameters as much as the other structural changes, it is worth noting that the larger H-O-H angle correlated with a larger span where for $(COOH)_2 \cdot 2H_2O$ and NaClO4$\cdot H_2O$ having H-O-H angle of ~105° had span of 26 ppm while $Ba(ClO)_3 \cdot H_2O$, $LiSO_4 \cdot H_2O$ and $K_2C_2O_4 \cdot H_2O$ with angles of ~110° had span of 30 ppm to 60 ppm. Finally, there is no clear correlation between the skew and the structural changes since neither δ_{iso} nor δ_{22} follow a certain trend.

CHAPTER FIVE:
CONCLUSIONS

In this thesis, I presented a new study of hydrogen bonding using ^{17}O NMR where experimental and computational results are combined to determine the impact of the hydrogen bond geometry on the NMR parameters. First, the MAS and static ^{17}O NMR spectra were acquired for oxalic acid hydrate, barium chlorate hydrate, lithium sulphate hydrate, potassium oxalate hydrate and sodium perchlorate hydrate. The $C_{Q,}$ η, δ_{iso}, $\delta_{11,}$ $\delta_{22,}$ and δ_{33} parameters were found to be 7.01 MHz, 0.77, 8.0 ppm, 12.0 ppm, 2.8 ppm and -2.5 ppm, 6.91 MHz, 0.98, 19.6 ppm, 36.7 ppm, 15.5 ppm, and 6.65 ppm, 7.39 MHz, 0.75, -15.0 ppm, -5.78 ppm, -6.45 ppm and -32.8 ppm, 6.85 MHz, 0.85, -8.0 ppm, 14.4 ppm, -4.8 ppm and -33.6 ppm, 6.75 MHz, 1.0, 0.8 ppm, 28.6 ppm, 5.2 ppm and -31.4 for $(COOH)_2{\bullet}2H_2O$, $Ba(ClO)_3{\bullet}H_2O$, $NaClO_4{\bullet}H_2O$, $LiSO_4{\bullet}H_2O$ and $K_2C_2O_4{\bullet}H_2O$ respectively. It is worth noting that CASTEP calculations overestimated the ^{17}O quadrupolar coupling constant and the span but gave a good agreement for the chemical shift tensor principal components. Variable temperature MAS NMR experiments were also conducted to determine the range of error can be expected from the experimental results due to rapid spinning. The biggest shift in the quadrupolar coupling constant and asymmetry parameter is due to the temperature change from -20 °C to 0 °C and δ_{iso} changed mostly over a range of 0°C to 33 °C.

Computational methods were used to study an organic hydrate model, oxalic acid hydrate, and an inorganic hydrate model, barium chlorate hydrate, where the O_w-H••O distance, O-H distance and H-O-H angle are changed to determine the impact they will have on the values of $C_{Q,}$ η, δ_{iso}, $\delta_{11,}$ $\delta_{22,}$ and δ_{33}. For oxalic acid hydrate, the most impact on its NMR parameters is due to the changes in the O-H bond length. Secondly, the barium

chlorate hydrate NMR parameters are most sensitive to the hydrogen bond distance and its metal-water distance. This distinction in the sensitivity between oxalic acid hydrate and the barium chlorate hydrate shows that experimental results cannot be compared since different geometrical factors are contributing to each. Lastly, computational models were built for M-O_w where M is Ba, Li, Na, and K and had the distance varied to observe its impact on the NMR parameters; $C_{Q,}$ η, Ω, $\delta_{11,}$ $\delta_{22,}$ and $\delta_{33.}$ It should be noted that the impact on the parameters as consequence of changing M-O_w decreases in order of Ba > Li > Na > K respectively and there is an increasing pattern of quadrupolar coupling constant and a decreasing pattern in the asymmetry parameter, span and chemical shift tensors as a function of increasing distance. The quadrupolar coupling constant can be related directly to the hydrogen bond distance in all inorganic hydrates where $NaClO_4•H_2O$ with longest hydrogen bond distance (2.152 Å) has the largest quadrupolar coupling constant of 7.39 MHz while the $K_2C_2O_4•H_2O$ with the shortest hydrogen bond distance (1.80 Å) had the smallest quadrupolar coupling constant of 6.75 MHz. The asymmetry parameter experimental results could not be correlated to any of geometrical features concluding that there are overlapping factors to the results obtained. Overall there is a correlation between the M-O_w distance and the impact it has most on first chemical shift tensor and least on the third chemical shift tensor component which is observed from the M-O_w models. It is also clear that the chemical shift tensor values for $NaClO_4•H_2O$, $LiSO_4•H_2O$ and $K_2C_2O_4•H_2O$ are closer to each other in comparison to the $Ba(ClO)_3•H_2O$. The skew did not have a clear correlation with geometrical structures which is not of a surprise since there is no clear correlation observed for the δ_{22} or δ_{iso}. Finally the span had a correlation with the hydrogen bond length and typically increased with an increasing length.

This study has provided a new insight into how ^{17}O solid-state NMR may be used to characterize the electric field gradient and the chemical shift tensors in a series of inorganic hydrates. The computational results complemented and revealed the trends for each parameter where C_Q and Ω increase as a function of increasing hydrogen bond distance, $\delta_{11,}$ $\delta_{22,}$ and δ_{33} decrease as a function of increasing M-O_w distance and unclear for asymmetry parameter and skew due to overlapping contributing factors. Further experimental data on a wider range of systems will help to solidify some of the trends suggested by the computations in this thesis.

REFERENCES

[1] Holland, G., Creager, J., Lewis, R., & Yarger, J. (2008). Determining secondary structure in spider dragline silk by carbon-carbon correlation solid-state NMR spectroscopy. *J. Am. Chem. Soc.*(130), 9871-9877.

[2] Engelhardt, G. (1999). Multinuclear NMR study of host-guest interactions in sodalities. *Solid-State NMR Spectroscopy of Inorganic materials, Chapter 9*, 266-282.

[3] Bryce, D. L., Bernard, G., Gee, M., Lumsden, M., Eichele, K., & Wasylishen, R. E. (2001). Practical aspects of modern routine solid-state multinuclear magnetic resonance spetroscopy: One-dimensional experiments. *Can. J. Anal. Sci. Spect.*(46), 46-82.

[4] Godefroy, S., Fleury, M., Deflandre, F., & Korb, J.-P. (2002). Temperature effect on NMR surface relaxation in rocks for well logging applications. *J. Phys. Chem.*(106), 11183-11190.

[5] Lundberg, P., Weich, R., Jensen, P., & Vogel, H. (1989). Phosphorus-31 and Nitrogen-14 NMR studies of the uptake of phosphorus and nitrogen compounds in the marine microalgae Ulva lactuca. *Plant Physiol.*(89), 1380-1387.

[6] Hamaed, H., Laschuk, M., Terskikh, V., & Schurko, R. (2009). Application of solid-state ^{209}Bi NMR to the structural characterization of bismuth-containing materials. *J. Am. Chem. Soc.*(23), 8271-8279.

[7] Zhu, J., Ye, E., Terskikh, V., & Wu, G. (2010). Solid-state ^{17}O NMR spectroscopy of large protein-ligand complexes. *Angew. Chem. Int. Ed.*(49), 8399-8402.

---

[8] Levitt, M. (2008). *Spin Dynamics: Basics of Nuclear Magenetic Resonance* (2 ed.). Chichester: Wiley.

[9] Apperley, D., Harris, R., & Hodgkinson, P. (2012). *Solid-State NMR: Basic Principles & Practice.* New-York: Momentum Press.

[10] Kasai, N., Kakudo, M. (2005). *X-Ray Diffraction by Macromolecules*. Tokyo: Kodansha Ltd.

[11] Suryanarayana, C., & Norton, M. (1998). *X-Ray Diffraction: A Practical Approach.* New York: Plenum Press.

[12] Eisenberg, D., & Kauzman, W. (1969). *The Structure and Properties of Water.* London: Oxford University Press.

[13] St-Amant, A. (2014). Quantum Mechanics [Powerpoint Slides]. Retrieved from University of Ottawa CHEM 8323 course material.

[14] St-Amant, A. (2014). Quantum Mechanics [Powerpoint Slides]. Retrieved from University of Ottawa CHEM 8323 course material.

[15] Harris, R., Hodgkinson, P., Pickard, C., Yates, J., & Zorin, V. (2007). Chemical shift computations on a crystallographic basis: some reflections and comments. *Magnetic Resonance in Chemistry*(45), S174-S186.

[16] Pickard, C., & Mauri, F. (2001). All-electron magnetic response with pesudopotentials: NMR chemical shifts. *Phys. Rev. B.*(63), 245101.

[17] Harris, R. K., Wasylishen, R. E., Duer, M. (2009) *NMR Crystallography*. Hoboken: Wiley.

---

[18] Latimer, W., Rodebush, W. (1920). Polarity and ionization from the standpoint of the Lewis theory of valence. *J. Am. Chem. Soc.* (42), 1419-1433.

[19] Dunitz, J., Taylor, R. (1997). Organic fluorine hardly ever accepts hydrogen bonds. *Chem. Eur. J.*(3), 89-98.

[20] Buckingham, A., Del Bene, J., & McDowell, S. (2008). The hydrogen bond. *Chem. Phys. Lett.*(463), 1-10.

[21] Peterson, S., Levy, H. (1957). A single-crystal neutron diffraction study of heavy ice. *Acta Cryst.*(10), 70-76.

[22] Chidambaram, S., Butler, P., Hamilton, W., Dadmun, M. (2000). What is a model liquid crystalline polymer solution?: Solvent effects on the flow behavior of LCP solutions. In *Scattering from Polymers* (pp. 356-373, Chapter 23). Retrieved from American Chemical Society Symposium Series, Vol. 739. Doi:10.1021/bk-2000-0739.ch023

[23] Nucci, N., & Vanderkooi, J. (2008). Effects of salts of the Hofmeister series on the hydrogen bond network of water. *J. Mol. Liq.*(143), 160-170.

[24] Irvine, W., Pollack, J. (1968). Infrared optical properties of water and ice spheres[1]. *Icarus*.(8), 324-360.

[25] Sharp, K., Vanderkooi, J. (2010). Water on the half shell: Structure of water, focusing on angular structure and solvation. *Acc. Chem. Res.*(43), 231-239.

[26] Ogg, R. (1946). Bose-Einstein condensation of trapped electron pairs - phase separation and superconductivity of metal-ammonia solutions. *Phys. Rev.*(69), 243-244.

---

[27] Witterbort, R., Usha, M., Ruben, D., Wemmer, D., & Pines, A. (1988). Observation of molecular reorientation in ice by proton and deuterium magnetic resonance. *J. Am. Chem. Soc.*(110), 5668-5671.

[28] Modig, K., & Halle, B. (2002). Proton magnetic shielding tensor in liquid water. *J. Am. Chem. Soc.*(124), 12031-12041.

[29] Huang, P., Schwegler, E., & Galli, G. (2009). Water confined in carbon nanotubes: Magnetic response and proton chemical shieldings. *J. Phys. Chem. C.*(113), 8696-8700.

[30] Lee, D., Saito, T., Benesi, A., Hickner, M., & Allcock, H. (2011). Characterization of water in proton-conducting membranes by deuterium NMR T-1 relaxation. *J. Phys. Chem. B.*(115), 776-783.

[31] Yao, X., Durr, UH., Gattin Z., Laukat, Y., Narayanan, R., Bruckner, A., et al. (2014). NMR-based detection of hydrogen/deuterium exchange in liposome-embedded membrane proteins. *PLoS One*.(9), e112374.

[32] Zhou, D., Nieuwkoop, A., Berthold, D., Comellas, G., Sperling, L., Tang, M., et al. (2012). Solid-state NMR analysis of membrane proteins and protein aggregates by proton detected spectroscopy. *J Biol BMR*.(54), 291-305.

[33] Wu, G., Freure, C. V., Verdurand, E. (1998). Proton chemical shift tensors and hydrogen bond geometry: A ^{1}H-^{2}H dipolar NMR study of the water molecule in crystalline hydrates. *J. Am. Chem. Soc.*(120), 13187-13193.

---

[34] Groves, W. & Pennington, C. (2005). Comparison of ^{17}O spin-lattice relaxation solid-state NMR studies of pure and doped ices. *Chem. Phys.*(315), 1-7.

[35] Ba, Y., Ripmeester, J., & Ratcliffe, C. (2011). Water molecular reorientation in ice and tetrahydrofuran clathrate hydrate from line shape analyses of ^{17}O spin-echo NMR spectra. *Can. J. Chem.*(89), 1055-1064.

[36] Spiess, H., Garrett, B., Sheline, R., & Rabideau, S. (1969). *J. Chem. Phys.*(51), 1201. doi:10.1063/1.1672122

[37] Zhu, J., Geris, A., & Wu, G. (2009). Solid-state ^{17}O NMR as a sensitive probe of keto and gem-diol forms of alpha-keto acid derivatives. *Phys. Chem. Chem. Phys.*(11), 6972-6980.

[38] Wu, G., Zhu, J., Mo, X., Wang, R., & Terskikh, V. (2010). Solid-state ^{17}O NMR and computational studies of C-Nitrosoarene compounds. *J. Am. Chem. Soc.*(132), 5143-5155.

[39] Kong, X., O'Dell, L., Terskikh, V., Ye, E., Wang, R., & Wu, G. (2012). Variable-temperature ^{17}O NMR studies allow quantitative evaluation of molecular dynamics in organic solids. *J. Am. Chem. Soc.*(134), 14609-14617.

[40] Martel, L., Magnani, N., Vigier, J., Boshoven, J., Selfslag, C., & Farnan, I. E. (2014). High-resolution solid-state oxygen-17 NMR of actinide-bearing compounds: An insight into the 5f chemistry. *Inorg. Chem.*(53), 6928-6933.

[41] Griffin, J., Wimperis, S., Berry, A., Pickard, C., & Ashbrook, S. (2009). Solid-state ^{17}O NMR spectroscopy of hydrous magnesium silicates: Evidence for proton dynamics. *J. Phys. Chem. C.*(113), 465-471.

---

[42] Wu, G., Dong, S., Isa, R., & Reen, N. (2002). A solid-state ^{17}O nuclear magnetic resonance study of nucleic acid bases. *J. Am. Chem. Soc.*(124), 1768-1777.

[43] Bryce, D., Eichele, K., & Wasylishen, R. (2003). An ^{17}O NMR and quantum chemical study of monoclinic and orthorhombic polymorphs of triphenylphosphine oxide. *Inorg. Chem.*(42), 5085-5096.

[44] Sabine, T., Cox, G., & Craven, B. (1969). A neutron diffraction study of alpha-oxalic acid dihydrate. *Acta. Cryst.*(B25), 2437-2441.

[45] Sikka, S., Momin, S., Rajagopal, H., & Chidambaram, R. (1968). Neutron diffraction refinement of the crystal structure of barium chlorate monohydrate $Ba(ClO_3)2H_2O$. *J. Chem. Phys.*(48), 1883-1890.

[46] Zieglar, G.E. (1934). The crystal structure of lithium sulphate mono-hydrate, $Li_sSO_4\ H_2O$. *Z. Krist.* (89), 456-461

[47] Smith, H., Peterson, S., & Levy, H. (1968). Neutron diffraction study of lithium sulfate monohydrate. *J. Chem. Phys.*(48), 5561-5565.

[48] Berglund, B., Thomas, J., & Tellgren, R. (1975). Hydrogen bond studies. CII. An X-ray determination of the crystal structure of sodium perchlorate monohydrate, $NaClO_4.H_2O$. *Acta Cryst.*(B31), 1842-1846.

[49] Sequeira, A., Srikanta, S., & Chidambaram, R. (1970). Neutron diffraction refinement of the structure of potassium oxalate monohydrate. *Acta Cryst.*(B26), 77-80.